

AD-A170 488

EFFECT OF CONVECTION ON WELD POOL SHAPE AND
MICROSTRUCTURE(U) ILLINOIS UNIV AT URBANA DEPT OF
MECHANICAL AND INDUSTRIAL ENGINEERING

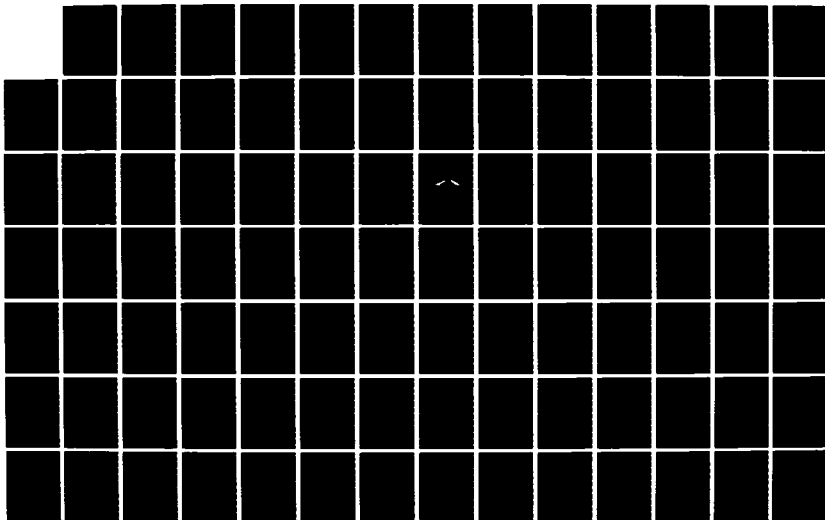
1/2

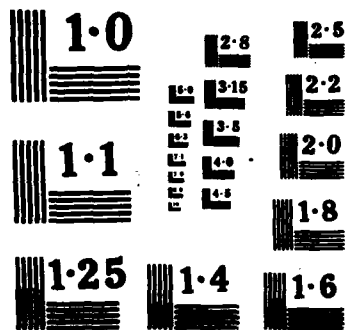
UNCLASSIFIED

J MAZUNDER ET AL. JUL 86 N00014-84-K-0315

F/G 11/6

NL





12



Department of Mechanical
and Industrial Engineering

University of Illinois at Urbana-Champaign
Urbana, IL 61801

EFFECT OF CONVECTION ON WELD POOL SHAPE AND MICROSTRUCTURE

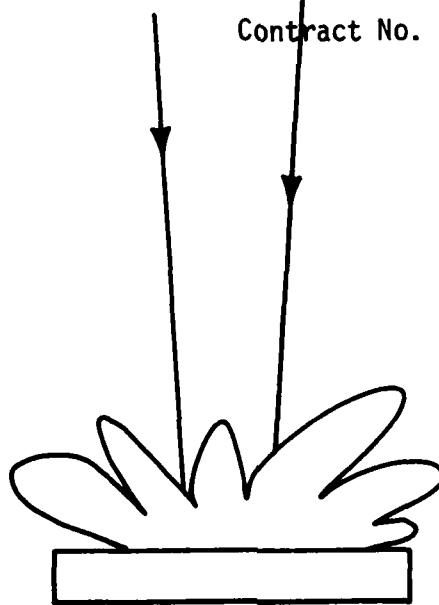
J. Mazumder, M. M. Chen, C. L. Chan and
R. Zehr

AD-A170 488

NTIC FILE COPY

Report to U.S. Navy
Contract No. N00014-84-K-0315

Laser
Applications
and
Materials
Processing



ADD 0 1984

E



EFFECT OF CONVECTION ON WELD POOL SHAPE AND MICROSTRUCTURE

Report to U.S. Navy
(Contract No. N00014-84-K-0315)

by

J. Mazumder, M. M. Chen, C. L. Chan, and R. Zehr
Department of Mechanical and Industrial Engineering
University of Illinois at Urbana-Champaign
1206 West Green Street
Urbana, IL 61801

July 1986



Approved For	
Dist	
A-1	

This document has been approved
for public release and sale; its
distribution is unlimited.

ABSTRACT

✓ The role of convection in weld pools is of great interest due to its effect on weld pool shapes and weld defects. A quantitative understanding of convection in the weld pool is being developed, at the University of Illinois at Urbana-Champaign under a program supported by the Office of Naval Research (Contract No. N00014-84-K-0315). This report describes the progress for the past two years effort during the period of April 15, 1984 to April 14, 1986.

> In this part of the effort major emphasis has been to model surface tension driven flow. The Lorentz force effect is incorporated towards the end of the two year effort. The significant achievements of the program are:

- a) Stagnation flow analysis for center of the weldpool which provided algebraic expressions for temperature and velocity. This solution clarifies the scaling problems.
- b) Three-dimensional axisymmetric model for surface tension driven flow with flat surface assumption which predicted the pool shape for stationary heat source such as in the case of spot welds.
- c) Three-dimensional perturbation model for surface tension driven flow with flat surface which predicted velocity field, temperature field, effect of trace elements and self-consistent prediction of the pool shape and cooling rate.
- d) Three-dimensional model with flat and free surface which predicted same as above with more realistic boundary condition. This model can also predict effect of Lorentz Force.

A series of controlled experiments has been carried out to verify pool shape and liquid velocity. This verified the trend predicted by the model.

TABLE OF CONTENTS

	Page
LIST OF TABLES.....	iv
LIST OF FIGURES.....	v
NOMENCLATURE.....	x
1. INTRODUCTION.....	1
2. TECHNICAL BACKGROUND.....	4
2.1 Materials Processing Processes.....	4
2.2 Surface Tension Gradient Driven Flow.....	5
2.3 Multidimensional Phase-Change Problem.....	6
3. FORMULATION.....	7
3.1 Perturbation Model.....	7
3.1.1 Introduction.....	7
3.1.2 Formulation.....	7
3.1.3 Results and Discussion.....	15
3.1.4 Conclusions.....	19
3.2 Stagnation Flow Analysis.....	30
3.2.1 Introduction.....	30
3.2.2 Formulation.....	31
3.2.3 Results and Discussion.....	33
3.2.4 Conclusions.....	43
3.3 Three Dimensional Numerical Model.....	65
3.3.1 Introduction.....	65
3.3.2 Formulation.....	65
3.3.3 Numerical Results.....	70
3.3.4 Conclusions.....	75
3.4 Experimental Verifications.....	116
3.4.1 Introduction.....	116
3.4.2 Experimental Procedure.....	116
3.4.3 Results and Discussion.....	117
3.4.4 Conclusions.....	118
4. SUMMARY AND CONCLUSIONS.....	127
REFERENCES.....	129

LIST OF TABLES

	Page
Table 3.1.1 The Numerical Values of the Dimensionless Parameters of the Nine Cases of the Perturbation Model.....	29
Table 3.2.1 Asymptotic Limits of the Stream Function at Small and Large \bar{z}	64
Table 3.2.2 Asymptotic Limits of the Surface Temperature Coefficients.....	64
Table 3.3.1 Governing Parameters.....	109
Table 3.3.2 Test Case Powers and Scanning Speeds.....	109
Table 3.3.3 Boundary Layer Thickness Estimates for Various Test Cases.....	110
Table 3.3.4 U-Velocity Variations Due to Variable Viscosity Along the Surface of the X-Z Plane with Y Located at the Symmetry Plane (Power = 200 W, $U_s = 0.010$ m/s).....	111
Table 3.3.5 V-Velocity Variations Due to Variable Viscosity Along the Surface of the Y-Z Plane with X Located at the Beam Center (Power = 200 W, $U_s = 0.010$ m/s).....	112
Table 3.3.6 W-Velocity Variations Due to Variable Viscosity in the X-Z Plane with X and Y Located at the Beam Center (Power = 200, $U_s = 0.010$ m/s).....	113
Table 3.3.7 Variation of U-Velocities Due to Electromagnetic Forces ($J \times D$ with Surface Tension) in the X-Y Plane with Z Located at the Material Surface (Power = 200 W, $U_s = 0.010$ m/s, Current = 100 Amps)...	114
Table 3.3.8 Variation of V-Velocities Due to Electromagnetic Forces ($J \times D$ with Surface Tension) in the X-Y Plane with Z Located at the Material Surface (Power = 200 W, $U_s = 0.010$ m/s, Current = 100 Amps)...	115
Table 3.4.1 Numerical Values of Process Parameters and the Results of the Experimental Runs.....	126

LIST OF FIGURES

Page

Figure 1.1	General Features and Various Regions of the Flow.....	3
Figure 3.1.1	Three-dimensional plot of the surface temperature for $Ma = 1,500$, $Pr = 0.15$, $T^* = 0.25$ and $RF = 0.0$ (perturbation model).....	20
Figure 3.1.2	Velocity field on the surface plane for $Ma = 1,500$, $Pr = 0.15$, $T^* = 0.25$ and $RF = 0.0$ (perturbation model).....	21
Figure 3.1.3	Velocity field on the vertical plane at $X_1^* = 0$ for $Ma = 1,500$, $Pr = 0.15$, $T^* = 0.25$ and $RF = 0.0$ (perturbation model).....	22
Figure 3.1.4	Trajectory of a particle as it enters, recir- culates and ultimately freezes. The trajectory is plotted in front, side, and top view in (a), (b), and (c), respectively. Initial position is $(X_1^*, X_2^*, X_3^*) = (-2.97, 0.423, 0.01)$ $Ma = 1,500$, $Pr = 0.15$, $T^* = 0.25$ and $RF = 0.0$ (perturbation model).....	23
Figure 3.1.5	Isotherms within the molten pool on the vertical plane $X_1^* = 0.05$ for $Ma = 1,500$, $Pr = 0.15$, $T_m^* = 0.25$ and $RF = 0.0$ (perturbation model).....	24
Figure 3.1.6	Isotherms within the molten pool on the vertical plane at $X_2^* = 0.0$ for $Ma = 1,500$, $Pr = 0.15$, $T_m^* = 0.25$ and $RF = 0.0$ (perturbation model).....	25
Figure 3.1.7	Family curves represent the surface temperature. Each curve corresponds to a different value of X_2^* for $Ma = 1,500$, $Pr = 0.15$, $T^* = 0.25$, and $RF = 0.0$ (perturbation model).....	26
Figure 3.1.8	Family curves of the temperature in a vertical plane ($X_1^* = 0$). Each curve corresponds to a different value of X_2^* $Ma = 1,500$, $Pr = 0.15$, $T_m^* = 0.25$ and $RF = 0.0$ (perturbation model).....	27
Figure 3.1.9	Comparison of the shape of the molten pool for different Prandtl number (perturbation model).....	28
Figure 3.2.1	Schematic Diagram of the Physical Model of the Stangation Flow Analysis.....	45

Figure 3.2.2	Graphs of the Stream Function \tilde{f}_1 , the Velocity Profile \tilde{f}_1' , and the Shear Stress \tilde{f}_1'' versus the Depth for both Two-Dimensional and Axisymmetric Cases (Stagnation Flow Analysis).....	46
Figure 3.2.3	Graphs of \tilde{g}_0 versus the Depth of the Two-Dimensional Case for Various Prandtl Numbers (> 1).....	47
Figure 3.2.4	Graphs of \tilde{g}_0 versus the Depth of the Two-Dimensional Case for Various Prandtl Numbers (< 1).....	48
Figure 3.2.5	Graphs of \tilde{g}_1 versus the Depth of the Two-Dimensional Case for Various Prandtl Numbers (> 1).....	49
Figure 3.2.6	Graphs of \tilde{g}_1 versus the Depth of the Two-Dimensional Case for Various Prandtl Numbers (< 1).....	50
Figure 3.2.7	Graphs of \tilde{g}_0 versus the Depth of the Axisymmetric Case for Various Prandtl Numbers (> 1).....	51
Figure 3.2.8	Graphs of \tilde{g}_0 versus the Depth of the Axisymmetric Case for Various Prandtl Numbers (< 1).....	52
Figure 3.2.9	Graphs of \tilde{g}_1 versus the Depth of the Axisymmetric Case for Various Prandtl Numbers (> 1).....	53
Figure 3.2.10	Graphs of \tilde{g}_1 versus the Depth of the Axisymmetric Case for Various Prandtl Numbers (< 1).....	54
Figure 3.2.11	Second Coefficient (Second Derivative) of the Surface Temperature versus the Prandtl Numbers (Stagnation Flow Analysis).....	55
Figure 3.2.12	Maximum Temperature versus the Prandtl Numbers (Stagnation Flow Analysis).....	56
Figure 3.2.13	Dimensionless Temperature Functions $\tilde{g}_0^0(\tilde{z}^0)$ and $\tilde{g}_1^0(\tilde{z}^0)$ of the Limiting Case of Small Prandtl Number (Stagnation Flow Analysis).....	57
Figure 3.2.14	Dimensionless Temperature Functions $\tilde{g}_0^1(\tilde{z}^1)$ and $\tilde{g}_1^1(\tilde{z}^1)$ of the Limiting Case of Large Prandtl Number (Stagnation Flow Analysis).....	58
Figure 3.2.15	Second Coefficient (Second Derivative) of the Surface Temperature versus the Prandtl Numbers (Stagnation Flow Analysis).....	59
Figure 3.2.16	Maximum Temperature versus the Prandtl Number (Stagnation Flow Analysis).....	60

Figure 3.2.17	Comparison of the Universal Velocity Profile F_1 for the Stagnation Flow Analysis and the Numerical Solution Results $Ma = 1,500$, $Pr = 0.15$, $T_m^* = 0.25$, and $RF = 0.0$	61
Figure 3.2.18	Comparison of the Centerline ($r = 0$) Temperature of the Stagnation Flow Analysis and the Numerical Solution Results $Ma = 1,500$, $Pr = 0.15$, $T_m^* = 0.25$, and $RF = 0.0$	62
Figure 3.2.19	Comparison of the Maximum Temperature of the Stagnation Flow Analysis and the Numerical Solution Results. The Numerical Solution Results are Numbered According to Table 5.1.....	63
Figure 3.3.1	Three-Dimensional Calculation Domain.....	78
Figure 3.3.2	X-Z Plane Cross-Section of the Calculation Domain (Y Located at the Symmetry Plane).....	79
Figure 3.3.3	Y-Z Plane Cross-Section of the Calculation Domain (X Located at the Beam Center).....	80
Figure 3.3.4	Melt Pool Isotherms in the X-Z Plane with Y Located at the Symmetry Plane (Power = 240 W, $U_s = 0.012$ m/s).....	81
Figure 3.3.5	Melt Pool Isotherms in the Y-Z Plane with X Located at the Beam Center (Power = 240 W, $U_s = 0.012$ m/s).....	82
Figure 3.3.6	Melt Pool Isotherms in the X-Y Plane with Z Located at the Material Surface (Power = 240 W, $U_s = 0.012$ m/s).....	83
Figure 3.3.7	Surface Temperature Contours (Power = 240 W, $U_s = 0.012$ m/s).....	84
Figure 3.3.8	Melt Pool Solid/Liquid Interface (Power = 240 W, $U_s = 0.012$ m/s).....	85
Figure 3.3.9	Melt Pool Isotherms in the X-Z Plane with Y Located at the Symmetry Plane (Power = 400 W, $U_s = 0.02$ m/s).....	86
Figure 3.3.10	Melt Pool Isotherms in the X-Y Plane with Z Located at the Material Surface (Power = 400 W, $U_s = 0.02$ m/s).....	87
Figure 3.3.11	Surface Temperature Contours (Power = 400 W, $U_s = 0.02$ m/s).....	88
Figure 3.3.12	Melt Pool Solid/Liquid Interface (Power = 400 W, $U_s = 0.02$ m/s).....	89

Figure 3.3.13 Melt Pool Velocity Field in the X-Z Plane with Y Located at the Symmetry Plane (Power = 240 W, $U_s = 0.012$ m/s).....	90
Figure 3.3.14 Melt Pool Velocity Field in the Y-Z Plane with X Located at the Beam Center (Power = 240 W, $U_s = 0.012$ m/s).....	91
Figure 3.3.15 Melt Pool Velocity Field in the X-Y Plane with Z Located at the Material Surface (Power = 240 W, $U_s = 0.012$ m/s).....	92
Figure 3.3.16 Melt Pool Velocity Field in the X-Z Plane with Y Located at the Symmetry Plane (Power = 400 W, $U_s = 0.02$ m/s).....	93
Figure 3.3.17 Melt Pool Velocity Field in the X-Y Plane with Z Located at the Material Surface (Power = 400 W, $U_s = 0.02$ m/s).....	94
Figure 3.3.18 Surface Temperature versus Distance(X) for Various Locations(Y) Away from the Beam Center (Power = 240 W, $U_s = 0.012$ m/s).....	95
Figure 3.3.19 Symmetry Plane Temperature versus Distance(X) for Various Locations(Z) Beneath the Domain Surface (Power = 240 W, $U_s = 0.012$ m/s).....	96
Figure 3.3.20 Surface Temperature versus Distance(X) for Various Locations(Y) Away from the Beam Center (Power = 400 W, $U_s = 0.02$ m/s).....	97
Figure 3.3.21 Symmetry Plane Temperature versus Distance(X) for Various Locations(Z) Beneath the Domain Surface (Power = 400 W, $U_s = 0.02$ m/s).....	98
Figure 3.3.22 Restricted Free Surface Deformation Based on Local Pressure Only (Power = 240 W, $U_s = 0.012$ m/s).....	99
Figure 3.3.23 Melt Pool Isotherms in the X-Z Plane with Y Located at the Symmetry Plane (Power = 200 W, $U_s = 0.010$ m/s).....	100
Figure 3.3.24 Melt Pool Isotherms in the X-Y Plane with Z Located at the Material Surface (Power = 200 W, $U_s = 0.010$ m/s).....	101
Figure 3.3.25 Melt Pool Velocity Field in the X-Z Plane with Y Located at the Symmetry Plane (Power = 200 W, $U_s = 0.010$ m/s).....	102

Figure 3.3.26 Melt Pool Velocity Field in the X-Y Plane with Z Located at the Material Surface (Power = 200 W, $U_s = 0.010$ m/s).....	103
Figure 3.3.27 Variation of Viscosity with Temperature.....	104
Figure 3.3.28 Melt Pool Isotherms in the Z=X-Z Plane with Y Located at the Symmetry Plane (Power = 200 W, $U_s = 0.010$ m/s) (JxB Forces Only).....	105
Figure 3.3.29 Melt Pool Isotherms in the X-Y Plane with Z Located at the Material Surface (Power = 200 W, $U_s = 0.010$ m/s) (JxB Forces Only).....	106
Figure 3.3.30 Melt Pool Velocity Field in the X-Z Plane with Y Located at the Symmetry Plane (Power = 200 W, $U_s = 0.010$ m/s) (JxB Force Only).....	107
Figure 3.3.31 Melt Pool Velocity Field in the X-Y Plane with Z Located at the Material Surface (Power = 200 W, $U_s = 0.010$ m/s) (JxB Forces Only).....	108
Figure 3.4.1 Schematic Diagram of the Experimental Set Up - Resolidified Region.....	119
Figure 3.4.2 Schematic Diagram of the Experimental Set Up - X-ray Shadow Graph.....	120
Figure 3.4.3 Micrograph of the Cross-section of the Laser Melted Pool, Laser Power = 8.0 kW, Beam Radius = 0.5 mm, Scanning Speed = 50 mm/sec.....	121
Figure 3.4.4 X-ray Shadow Graph of Two Successive Frames Showing the Motion of the Tungsten Particle.....	122
Figure 3.4.5 Color Enhanced of X-ray Shadow Graph Showing the Temperature Difference at 1 Second after the Arc is Turned Off.....	123
Figure 3.4.6 Color Enhanced of X-ray Shadow Graph Showing the Temperature Difference at 5 Seconds after the Arc is Turned Off.....	124
Figure 3.4.7 Color Enhanced of X-ray Shadow Graph Showing the Temperature Difference at 9 Seconds after the Arc is Turned Off.....	125

NOMENCLATURE

C_p	heat capacity
d	width of laser beam for the two-dimensional transient model
D	thickness of workpiece
f_1	stream function of the stagnation flow analysis
f_1^*	dimensionless stream function
\tilde{f}_1	universal dimensionless stream function
\tilde{f}_∞	$\tilde{f}_1(\infty)$
\tilde{f}'_{10}	$\left. \frac{d\tilde{f}_1}{d\tilde{z}} \right _{\tilde{z}=0}$
$f^{+'}$	stream function of the stagnation flow analysis calculated from numerical solution of the axisymmetric case
$g_{0,1}$	temperature functions
$g_{0,1}^*$	dimensionless temperature functions
$\tilde{g}_{0,1}$	rescaled dimensionless temperature functions
\tilde{g}_{10}	$\tilde{g}_1(0)$
$\tilde{g}_{0,1}^0$	stretched temperature functions for the case of small Pr
$\tilde{g}_{0,1}^i$	stretched temperature functions for the case of large Pr
\tilde{g}_{10}^0	$\tilde{g}_1^0(0)$
\tilde{g}_{10}^i	$\tilde{g}_1^i(0)$
$g_0^+(\tilde{z})$	centerline temperature of the stagnation flow analysis calculated from numerical solution of the axisymmetric case
h	heat transfer coefficient, along the solid-liquid interface
h^*	dimensionless heat transfer coefficient along the solid-liquid interface
k	thermal conductivity
L	length of the workpiece
m	dimensionality index; 2 for two-dimensional and 3 for axisymmetric

Ma	Marangoni number
\vec{n}	normal vector along the interface
n_i	i th component of the normal vector of the free surface
p	pressure
Pe	Peclet number $u_s r_0 / \kappa$
Pr	Prandtl number ν / κ
P_a	atmospheric pressure
q''	non-uniform heat flux distribution
$q_{0,1}$	coefficient of the heat source expansion
q	average heat flux of q''
Q	total power from laser
r	radial axis
r_0	radius of the laser beam
$R_{1,2}$	principal radii of curvature
Re	Reynolds number $u_c r_0 / \nu$
RF	Radiative heat loss parameter
\vec{s}	tangential vector of the free surface
s_i	i th component of the tangential vector
S	surface tension number, u_c / u_s
t	time
T	temperature
T^*	dimensionless temperature
T_0^*	temperature of the axisymmetric case
T_1^*	temperature of the perturbation
T_m^*	dimensionless melting temperature
T_a	ambient temperature
T_c	surface temperature at the center

T_{∞}	temperature of the liquid metal at a large distance from the surface in the melt pool
T_a^*	dimensionless ambient temperature
\underline{u}	velocity vector
$u_{1,2,3}$	velocity component in $x_{1,2,3}$ direction, respectively
u_c	thermocapillary velocity
u_r	r-component velocity
$\tilde{u}_{ro,1}$	r-component velocity expansion
u_{θ}	θ - component velocity
$\tilde{u}_{\theta o,1}$	θ -component velocity expansion
u_z	z-component velocity
$\tilde{u}_{zo,1}$	z-component velocity expansion
u_s	scanning speed of workpiece
u_n	normal velocity of the interface
W	width of workpiece
$x_{1,2,3}$	index form of rectangular coordinates
z	depth axis

Greek

β	coefficient of thermal expansion
γ	surface tension
γ'	temperature coefficient of surface tension
δ	$\delta = (k_{\mu\nu}/2\gamma'q_1)^{1/4}$
δ_{κ}	thermal boundary layer scale
δ_{ν}	viscous boundary layer scale
ϵ	emissivity
η	elevation of the free surface
θ	angular axis

κ	thermal conductivity
λ	latent heat of fusion
μ	dynamic viscosity
ν	kinematic viscosity
ρ	density
σ	Stefan-Boltzman constant
τ	stress tensor
$\phi_{0,1}$	functions defined the solid-liquid interface

Superscripts

*	dimensionless quantities
~	decomposed velocity field
^	amplitudes of the angular dependence
o	stretched variable for the asymptotic case of $Pr \rightarrow 0$
i	stretched variable for the asymptotic case of $Pr \rightarrow \infty$

Subscripts

l	liquid
s	solid
m	melting
a	ambient

1. INTRODUCTION

When a concentrated heat source, such as laser, arc, or electron beam, is directed at the surface of a moving substrate, several phenomena occur simultaneously. Heat is being reflected, absorbed, and re-radiated on the surface. The absorbed heat develops a molten region. Inevitably, there exists a fluid flow within this molten region. In addition to the convection due to the motion of the substrate, there is also the convection due to the fluid flow within the molten pool. Depending on the type of heat source, the fluid flow may be caused by the surface tension gradient or the Lorentz force or both. Buoyancy force can also play a role in establishing the fluid flow in the case of casting. When the dimension of the molten region is small as in the case of welding and laser materials processing, buoyancy force becomes unimportant. Beyond the molten region, the absorbed heat is conducted into the substrate and transported away by the motion of the substrate.

A quantitative understanding of convection in the weld pool is being developed for the last two years at UIUC under a research program sponsored by ONR. In the last two years, the significant achievements of the program are:

- a. Stagnation flow analysis for center of the weld pool which provided algebraic expressions for temperature and velocity [47,48]. This solution clarifies all the scalings of the problem, i.e. the effects of process parameters on the magnitude of velocity fields, temperature, and the extent of the viscous effect can be better understood.
- b. Three-dimensional axisymmetric model for surface tension driven flow with flat surface assumption which provided self-consistent prediction of the pool shape for stationary heat source: velocity and temperature fields are also obtained [49].

c. Three-dimensional perturbation model for surface tension driven flow with flat surface [50,51]:

- Velocity field is obtained: Qualitative understanding of the mixing mechanism has been achieved by particle tracing
- Temperature field is obtained which provided self-consistent prediction of the pool shape and prediction of the cooling rate
- Effect of trace element (positive surface tension coefficient) on velocity field and pool shape is also examined.

NOTE: Due to the perturbation technique used, this model is valid only for moderate and low scanning speed.

d. Full three-dimensional model for surface tension driven flow with flat surface and free surface [51,46]:

Numerical Solution

- Results are comparable to three-dimensional perturbation model; however, this model is capable of handling high scanning speed as well as low scanning speed
- Predictions of pool shape, cooling rate and free surface shape

These analyses improved the physical understanding of the process and certain general features of the flow (see Fig. 1.1). Since these flow processes appear to have singularities (Region 3, Fig. 1.1) and certain limiting behaviors, much work must be done to fully understand the convection in the weld. Free surface and effect of Lorentz forces should also be considered. This report discusses the effect of surface tension driven flow in detail and provides initial data for free surface and effect of Lorentz force acting simultaneously with surface tension driven flow.

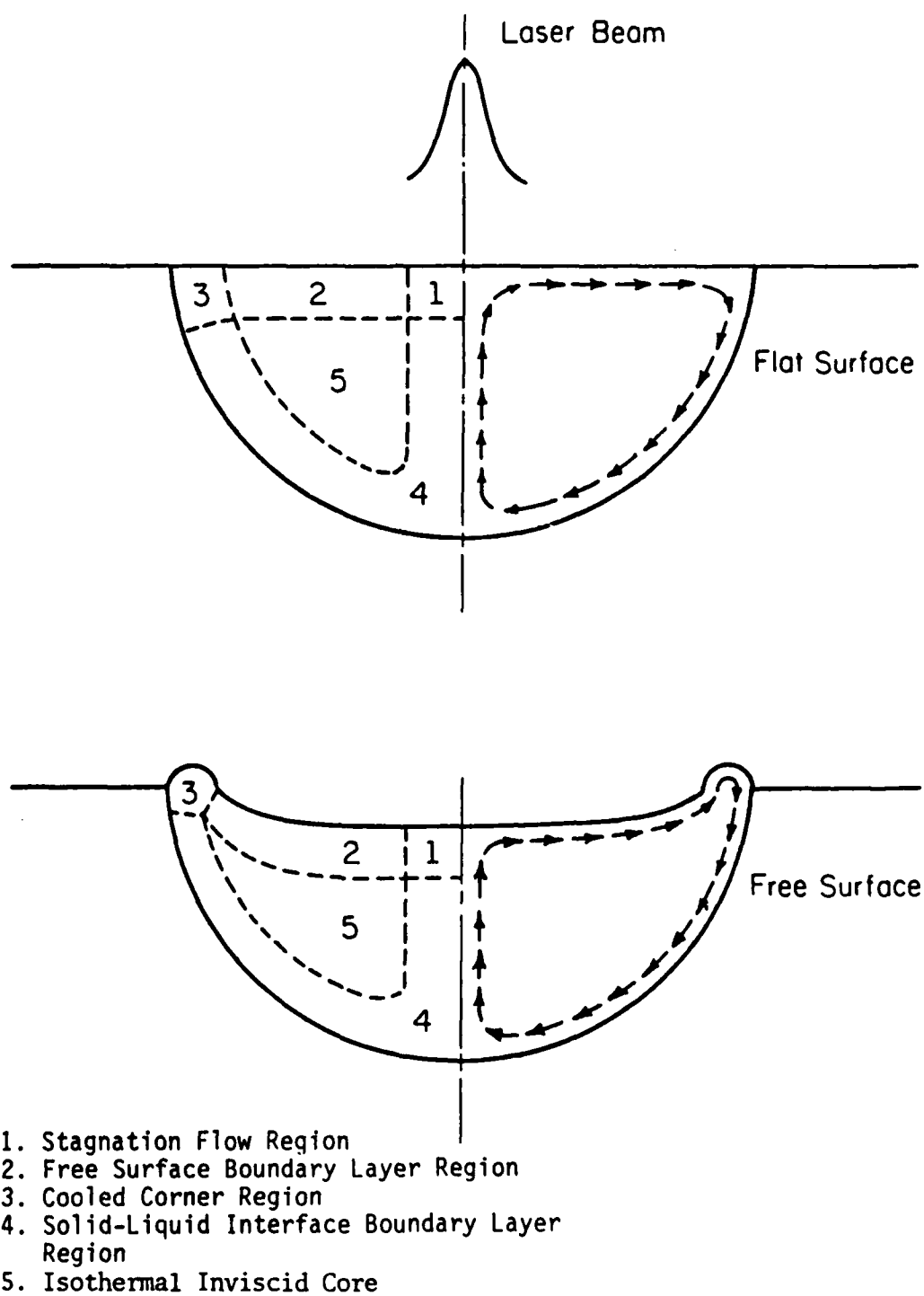


Figure 1.1 General Features and Various Regions of the Flow

2. TECHNICAL BACKGROUND

2.1 Materials Processing Processes

It has been recognized by several researchers [1-14] that convection plays a major role in arc, laser, and electron beam weld pools. Convection is the single most important factor influencing the geometry of the pool including pool shape, undercut, and ripples. It can result in defects such as variable penetration, porosity, and lack of fusion. It is also primarily responsible for mixing, thus, affecting the composition of the weld pool.

Fluid flow and its effect on weld homogeneity were reported by Houldcroft [8] and Pumphrey [9] almost three decades ago. They have shown that for a number of arc weldings with a filler metal of different composition to the base metal give rise to substantially uniform weld beads which imply mixing in the weld pool. Also, the well-known Shaeffler diagram [10] implicitly assumes complete and perfect mixing of filler metal and base metal plates of different composition, and is found to work out well in practice.

Apps and Milner [11] determined the "effective thermal conductivity" of molten lead under an arc. They found it to be considerably greater than that of static molten metal, showing the existence of convection and fluid flow in arc weld pools. Both Apps, et al. [12] and Christensen, et al. [13], attributed the shape of the weld pool, at least partially, to the motion in the molten metal. Bradstreet [14] reported the general patterns for the fluid flow within the weld pool and its effect on bead formation.

Fluid flow in weld pools also affects the mixing [15-19] of the reacting products and the solidifying structure [20,21]. Even relatively mild convection, as experienced in ingot casting, affects the solidifying structure [22]. Chande and Mazumder [15], observed that an effective diffusivity of $10^6 \text{cm}^2/\text{sec}$ (10 orders of magnitude higher than the actual diffusivity) is

required to explain the experimentally obtained uniform solute redistribution during Laser Surface Alloying (LSA) on the basis of molecular diffusion. The implication as pointed out by Chande and Mazumder is that the fluid flow within the molten pool plays a significant role in the mechanism of solute redistribution.

2.2 Surface Tension Gradient Driven Flow

Surface tension gradient driven flow has been identified to be responsible for ripple formation in the weld [23-26]. Copley, et al. [23-25], discussed, qualitatively, the mechanism of ripple formations by surface tension gradient driven flow. Anthony and Cline [26] developed a steady state one-dimensional model for the fluid flow and predicted the spacing and height of the surface ripple. The momentum equation is solved based on the temperature field given by the conduction equation. Therefore, convective heat transfer within the molten region was not considered. Oreper, et al. [27], did a numerical solution for the convective heat transfer within the molten pool during arc welding. Buoyancy, electromagnetic, and surface tension forces were considered. It was found that the surface tension gradient is the dominant factor in many cases. The model has the inconsistency that the solid-liquid interface, which is not known a priori, was being specified. Heat transfer and fluid flow during electron beam welding, when keyholing phenomenon occurs, was studied by W. Geidt [28]. In such a case, a thin layer of molten metal is found between the plasma, which is formed by the keyholing effect, and the solid phase. Within the framework of boundary layer assumption, he obtained a solution for the fluid flow and the heat transfer. Surface tension gradient driven flow also arises in zone melting crystal growth. A general formulation and dimensionless governing parameters were

derived by Ostrach [29]. An extensive review of literatures in this area can be found in Ref. [29].

2.3 Multidimensional Phase-Change Problem

The problem of multidimensional phase-change heat transfer is a very complicated one. It involves the coupling of the energy equations in different phases through the interface which in most cases is irregular. Analytical and semi-analytical methods have a very limited range of applicability [30]. Numerical solutions using finite difference or finite elements are more versatile. A detailed review of the numerical methods has been published by Shamsundar [31]. He compared various numerical methods of solving multidimensional phase-change problem. Various methods of solving multidimensional phase-change heat transfer were reviewed by Viskanta [30]. The available methods can be broadly divided into two groups, (1) temperature as the primitive variable, and (2) enthalpy as the primitive variable. Large number of numerical works are based on finite difference formulation, although finite element seems to be able to treat the irregular boundaries which often exist in multidimensional phase-change problem. A general finite element solution method has been developed by Lynch and O'Neil [32]. The method has been applied to a one-dimensional phase-change heat transfer problem only.

The finite difference schemes are much better developed. The temperature based method can be further divided into four categories [30]: (1) the explicit finite difference scheme, (2) the implicit finite difference scheme, (3) the moving boundary immobilization method, and (4) the isotherm migration method. The enthalpy based methods, on the other hand, have their merits. A detailed discussion of the advantages and disadvantages of the enthalpy-based model can be found in Ref. [31]. Brief descriptions of various numerical

methods (both finite difference and finite element) and a long list of references can be found in the review by Viskanta [30].

Multidimensional phase-change with convection is also discussed in [30]. In addition to the complication of coupling of the energy equations of the different phases through the interface, there is the coupling of energy, momentum, and continuity equations within the liquid phase. Some works have been done for the case of phase-change with natural convection in the liquid phase [30].

In order to achieve a quantitative understanding of the effects of convection on pool shape and mixing, mathematical modeling of the flow in the pool is needed. In an arc weld pool both surface tension gradient driven flow and electromagnetic field driven flow play a role, whereas in laser welding only the flow driven by surface tension variation is important. Therefore, laser melted pool is an ideal candidate to study the affect of the flow driven by surface tension variation separated from electromagnetic field driven flow. Recently, it has also been recognized that at moderate current (up to 150 ampere) surface tension plays a major role even in arc melted pools [27]. In view of the foregoing, convection in laser melted pools is analyzed.

The present report consists of three models of the thermocapillary convection in the melt pool. The first model is a perturbation solution of the full three-dimensional problem. As it turns out the recirculatory flow due to thermocapillarity is much larger than the scanning speed. Perturbation solution is therefore sought. This approach has the advantage of reducing the original three-dimensional problem to two-dimensional. However, this solution is limited to lower scanning speed. The second model is the stagnation flow. It can be observed from the results of the perturbation model (or the full three-dimensional model) that near the center right underneath the

beam. The flow has a great similarity to stagnation flow except the motion is now driven by the surface shear not the impinging flow. This provides a clear picture of the structures of the fluid flow and heat transfer in this stagnation region. Quantities such as maximum temperature, surface velocity, viscous and thermal boundary layers can be estimated from the derived algebraic equations. The final model is a full three-dimensional calculation of the Navier-Stokes and energy equations. This model also has the capability to treat free surface flow.

In the present work, we have limited ourselves to the problems of the fluid flow and the heat transfer in the molten and solid regions. The laser beam is modeled as a surface heat source so that the keyholing phenomenon is not considered. The objective of this research is to understand the physics of the process--the mechanism and the coupling of the fluid flow and the heat transfer. The effects of the fluid flow and the heat transfer on pool characteristics, such as pool shape, cooling rate, recirculating flow, and temperature, are quantified.

3. FORMULATION

3.1 Perturbation Model

3.1.1 Introduction

In this section, the perturbation model of the three-dimensional problem is presented. It was found that the recirculating velocity is much higher than the scanning velocity. Therefore, the convection due to the recirculating velocity is much larger than that due to the scanning velocity. In view of the above, a perturbation solution is therefore attempted. The basic solution corresponds to the stationary spot source, and the perturbation is based on a small scanning velocity. The advantage of seeking a perturbation solution, as it turns out, is that the three-dimensional problem is solved by solving two sets of two-dimensional equations. The formulation is as follows. The non-dimensional form is first derived. The velocity field is next decomposed into two parts, the first part is the recirculation and the second is the scanning velocity. An asymptotic series expansion is sought. The zeroth order terms correspond to the axisymmetric solution. The first order terms are the perturbations due to low scanning speed. The angular dependence of the perturbation terms are separable thereby reducing the three-dimensional problem to two-dimensional.

3.1.2 Formulation

The final dimensionless governing equations are given below, for detail derivation refer to Ref. [42].

$$t^* = \frac{t}{r_0/u_c}, \quad (r^*, \theta^*, z^*) = \left(\frac{r}{r_0}, \theta, z/r_0\right)$$

$$p^* = \frac{p - p_\infty}{\rho u_c^2}, \quad T^* = \frac{T - T_\infty}{qr_0/k}, \quad (u_r^*, u_\theta^*, u_z^*) = \frac{(u_r, u_\theta, u_z)}{u_c}$$

where

$$u_c = \frac{\gamma' q r_o}{k\mu} \quad (3.1.1)$$

The zeroth order is axisymmetric and the governing equations are continuity:

Continuity:

$$\frac{1}{r^*} \frac{\partial \tilde{u}_{ro}}{\partial r^*} + \frac{\partial \tilde{u}_{zo}}{\partial z^*} = 0 \quad (3.1.2)$$

r-momentum equation:

$$\frac{1}{r^*} \frac{\partial}{\partial r^*} r^* \tilde{u}_{ro}^2 + \frac{\partial}{\partial z^*} \tilde{u}_{zo} \tilde{u}_{ro} = - \frac{\partial p_o^*}{\partial r^*} + \frac{1}{Re} \left(\frac{1}{r^*} \frac{\partial}{\partial r^*} r^* \frac{\partial \tilde{u}_{ro}}{\partial r^*} + \frac{\partial^2 \tilde{u}_{ro}}{\partial z^{*2}} - \frac{\tilde{u}_{ro}}{r^{*2}} \right) \quad (3.1.3)$$

z-momentum equation:

$$\frac{1}{r^*} \frac{\partial}{\partial r^*} r^* \tilde{u}_{zo} \tilde{u}_{ro} + \frac{\partial}{\partial z^*} \tilde{u}_{zo}^2 = - \frac{\partial p_o^*}{\partial z^*} + \frac{1}{Re} \left(\frac{1}{r^*} \frac{\partial}{\partial r^*} r^* \frac{\partial \tilde{u}_{zo}}{\partial r^*} + \frac{\partial^2 \tilde{u}_{zo}}{\partial z^{*2}} \right) \quad (3.1.4)$$

the energy equations within the molten region:

$$\frac{1}{r^*} \frac{\partial}{\partial r^*} r^* \tilde{u}_{ro} T_o^* + \frac{\partial}{\partial z^*} \tilde{u}_{zo} T_o^* = \frac{1}{Ma} \left(\frac{1}{r^*} \frac{\partial}{\partial r^*} r^* \frac{\partial T_o^*}{\partial r^*} + \frac{\partial^2 T_o^*}{\partial z^{*2}} \right) \quad (3.1.5)$$

the energy equation in the solid region:

$$0 = \frac{1}{r^*} \frac{\partial}{\partial r^*} r^* \frac{\partial T_0^*}{\partial r^*} + \frac{\partial^2 T_0^*}{\partial z^{*2}} \quad (3.1.6)$$

The appropriate boundary conditions are, on the surface,

$$z^* = 0; \quad \frac{\partial \tilde{u}_{r0}}{\partial z^*} = - \frac{\partial T_0^*}{\partial r^*}$$

$$\tilde{u}_{z0} = 0 \quad (3.1.7)$$

$$\frac{\partial T_0^*}{\partial z^*} = \begin{cases} -q''^* + RF[(T_0^* + T_a k/q r_0)^4 - (T_a k/q r_0)^4], & r^* \leq 1 \\ + RF[(T_0^* + T_a k/q r_0)^4 - (T_a k/q r_0)^4], & \text{otherwise} \end{cases}$$

along the solid-liquid interface,

$$\tilde{u}_{r0} = \tilde{u}_{z0} = 0 \text{ and } \frac{\partial T_0^*}{\partial r^*} = \frac{\partial T_0^*}{\partial n^*} \quad (3.1.8)$$

at the surface defined by $T^* = T_m^*$,

and finally at a distance away,

$$r^*, z^* \rightarrow \infty; \quad T_0^* \rightarrow 0 \quad (3.1.9)$$

The governing equations for the perturbation are:

Continuity:

$$\frac{1}{r^*} \frac{\partial}{\partial r^*} r^* \hat{u}_{r1} + \frac{\hat{u}_{\theta 1}}{r^*} + \frac{\partial \hat{u}_{z1}}{\partial z^*} = 0 \quad (3.1.10)$$

r-momentum equation:

$$\begin{aligned} & \left[\frac{2}{r^*} \frac{\partial r^*}{\partial r^*} \tilde{u}_{ro} - \frac{\tilde{u}_{ro}}{r^*} + \frac{\partial \tilde{u}_{zo}}{\partial r^*} \right] + \frac{2}{r^*} \frac{\partial}{\partial r^*} r^* \tilde{u}_{ro} \hat{u}_{r1} \\ & + \frac{\tilde{u}_{ro} \hat{u}_{\theta 1}}{r^*} + \frac{\partial}{\partial z^*} (\tilde{u}_{zo} \hat{u}_{r1} + \hat{u}_{z1} \tilde{u}_{ro}) \\ & = - \frac{\partial \hat{p}_1}{\partial r^*} + \frac{1}{Re} \left(\frac{\partial^2 \hat{u}_{r1}}{\partial r^{*2}} + \frac{1}{r^*} \frac{\partial \hat{u}_{r1}}{\partial r^*} + \frac{\partial \hat{u}_{r1}}{\partial z^{*2}} - \frac{2\hat{u}_{r1}}{r^{*2}} - \frac{2\hat{u}_{\theta 1}}{r^{*2}} \right) \end{aligned} \quad (3.1.11)$$

θ -momentum equation:

$$\begin{aligned} & \left[\frac{-1}{r^*} \frac{\partial}{\partial r^*} r^* \tilde{u}_{ro} - \frac{\partial \tilde{u}_{zo}}{\partial z^*} - \frac{\tilde{u}_{ro}}{r^*} \right] + \frac{1}{r^*} \frac{\partial}{\partial r^*} r^* \tilde{u}_{ro} \hat{u}_{\theta 1} + \frac{\partial}{\partial z^*} \tilde{u}_{zo} \hat{u}_{\theta 1} \\ & + \frac{\tilde{u}_{ro} \hat{u}_{\theta 1}}{r^*} = \frac{\hat{p}_1}{r^*} + \frac{1}{Re} \left(\frac{\partial^2 \hat{u}_{\theta 1}}{\partial r^{*2}} + \frac{1}{r^*} \frac{\partial \hat{u}_{\theta 1}}{\partial r^*} + \frac{\partial^2 \hat{u}_{\theta 1}}{\partial z^{*2}} - \frac{2\hat{u}_{r1}}{r^{*2}} - \frac{2\hat{r}_{\theta 1}}{r^{*2}} \right) \end{aligned} \quad (3.1.12)$$

z-momentum equation:

$$\begin{aligned} & \left[\frac{1}{r^*} \frac{\partial}{\partial r^*} r^* \tilde{u}_{zo} - \frac{\tilde{u}_{zo}}{r^*} \right] + \frac{1}{r^*} \frac{\partial}{\partial r^*} r^* (\tilde{u}_{zo} \hat{u}_{r1} + \hat{u}_{z1} \tilde{u}_{ro}) \\ & + \frac{1}{r^*} \tilde{u}_{zo} \hat{u}_{\theta 1} + 2 \frac{\partial}{\partial z^*} \tilde{u}_{zo} \hat{u}_{z1} \\ & = - \frac{\partial \hat{p}_1}{\partial z^*} + \frac{1}{Re} \left(\frac{\partial^2 \hat{u}_{z1}}{\partial r^{*2}} + \frac{1}{r^*} \frac{\partial \hat{u}_{z1}}{\partial r^*} + \frac{\partial^2 \hat{u}_{z1}}{\partial z^{*2}} - \frac{\hat{u}_{z1}}{r^{*2}} \right) \end{aligned} \quad (3.1.13)$$

the energy equation within the molten region:

$$\begin{aligned}
 & \left[\frac{1}{r^*} \frac{\partial}{\partial r^*} r^* T_0^* - \frac{T_0^*}{r^*} \right] + \frac{1}{r^*} \frac{\partial}{\partial r^*} r^* (\bar{u}_{r0} \hat{T}_1 + \hat{u}_{r1} T_0^*) \\
 & + \frac{T_0^* \hat{u}_{\theta 1}}{r^*} + \frac{\partial}{\partial z^*} (\bar{u}_{z0} \hat{T}_1 + \hat{u}_{z1} T_0^*) \\
 & = \frac{1}{\text{Ma}} \left(\frac{\partial^2 \hat{T}_1}{\partial r^{*2}} + \frac{1}{r^*} \frac{\partial \hat{T}_1}{\partial r^*} + \frac{\partial^2 \hat{T}_1}{\partial z^{*2}} - \frac{\hat{T}_1}{r^{*2}} \right)
 \end{aligned} \tag{3.1.14}$$

the energy equation in the solid region:

$$\frac{1}{r^*} \frac{\partial}{\partial r^*} \hat{T}_0 r^* + \frac{\hat{T}_0}{r^*} \frac{1}{\text{Ma}} \left(\frac{\partial^2 \hat{T}_1}{\partial r^{*2}} + \frac{1}{r^*} \frac{\partial \hat{T}_1}{\partial r^*} + \frac{\partial^2 \hat{T}_1}{\partial z^{*2}} - \frac{\hat{T}_1}{r^{*2}} \right) \tag{3.1.15}$$

the boundary conditions become,

on the free surface,

$$z^* = 0;$$

$$-\frac{\partial \hat{u}_{r1}}{\partial z^*} = \frac{\partial \hat{T}_1}{\partial r^*}, \quad \frac{\partial \hat{u}_{\theta 1}}{\partial z^*} = + \frac{\hat{T}_1}{r^*}$$

$$\hat{u}_{z1} = 0$$

$$\frac{\partial \hat{T}_1}{\partial z^*} = 4 \text{ RF } \hat{T}_1 (T_0^* + T_a k/q r_0)^3 \tag{3.1.16}$$

along the solid-liquid interface,

$$\begin{aligned}
 \hat{T}_1 [\phi_0^*] &= - \frac{\delta T_0^*}{\delta \phi^*} \Big|_{\phi_0^*} \hat{\phi}_1 \\
 \frac{\partial \hat{T}_{1l}}{\partial n^*} &= \frac{\partial \hat{T}_{1s}}{\partial n^*} \\
 \hat{u}_{r1} [\phi_0^*] &= - \frac{\delta \tilde{u}_{r0}}{\delta \phi^*} \Big|_{\phi_0^*} \hat{\phi}_1 \\
 \hat{u}_{\theta 1} [\phi_0^*] &= 0 \\
 \hat{u}_{z1} [\phi_0^*] &= - \frac{\delta \tilde{u}_{z0}}{\delta \phi^*} \Big|_{\phi_0^*} \hat{\phi}_1
 \end{aligned} \tag{3.1.17}$$

and finally at a distance away,

$$r^*, z^* \rightarrow \infty;$$

$$\hat{T}_1 = 0 \tag{3.1.18}$$

where

$$Re = \frac{u_c r_0}{\nu} = \frac{\gamma' q r_0^2}{k_{\mu\nu}}$$

$$Ma = \frac{u_c r_0}{\kappa} = \frac{\gamma' q r_0^2}{k_{\mu\kappa}}$$

$$T_m^* = \frac{T_m - T_\infty}{q r_0 / k}$$

$$RF = \frac{\epsilon \sigma}{q} \left(\frac{q r_o}{k} \right)^4 \quad (3.1.19)$$

The three-dimensional problem is therefore represented by two sets of two-dimensional equations. The basic solution is described by the system Eqs. (3.1.2) through (3.1.9), and the perturbation solution is described by the system Eqs. (3.1.10) through (3.1.18). However, the perturbation model is limited to slow scanning speed.

Numerical solutions are sought for the two sets of two-dimensional equations of the perturbation model. Finite difference equations, central difference for the diffusion terms and upwind difference for the convective terms, governing the velocities and temperature are derived. The staggered grid is used. The resultant non-linear algebraic equations are solved by standard Alternating Direction Iteration (ADI) method [34].

The computational procedure is as follows. For a certain temperature field where both solid and liquid region exist, the interface is first determined. The velocities within the molten pool are iterated for a prescribed number of iterations. Using this updated velocity field, the energy equations are iterated next. Thus, the temperature field for the next global iteration is obtained. The initial guesses are the steady state conduction temperature and zero velocity for the basic solution, and zero temperature and velocity for the perturbation solution. The convergent solutions are obtained when the average residual of each equation is smaller than a specified small number, typically 10^{-4} .

3.1.3 Results and Discussion

Numerical solutions for nine cases have been obtained. The values of the governing parameters are tabulated in Table 3.1.1. In order to

visualize this three-dimensional fluid flow and convection, the results are presented in the familiar cartesian coordinates, as depicted in Fig. 3.1.1, even though the calculations were done in cylindrical coordinates. Using 0.0001 for u_s/u_c , a solution can be obtained. The values of the governing parameters are Case #1 tabulated in Table 3.1.1. The following graphs were plotted based on this result unless specified otherwise.

a. Surface Temperature: A three-dimensional plot of the surface temperature is presented in Fig. 3.1.1 for Case #1. The horizontal plane is the surface $x_1^* - x_2^*$ plane and vertical axis is the dimensionless temperature. The temperature distribution is very much expected. The temperature attains its maximum at the center underneath the beam and decreases radially outward. It is interesting to note that the temperature gradient, the driving force, has three distinct regimes. Its magnitude increases from zero at the center in the radial direction roughly until the edge of the laser beam, it then decreases and finally increases again as the flow approaches the edge of the molten pool. The first stage, being so close to the center, the increase in temperature gradient is caused by surface heating. The fluid flow driven by the surface tension gradient becomes important in the second stage where it tends to smooth out the temperature. Finally, the flow approaches the edge of the molten pool, and turns around. This phenomenon is very similar to the heat transfer near the stagnation point, and therefore gives rise to high temperature gradient.

b. Velocity Field: The variation of surface temperature due to surface heating induces a surface tension gradient thus pulling the molten materials radially outward. The velocity field on the surface of the molten pool is

plotted in Fig. 3.1.2. The velocity field in the vertical plane at $x_1^* = 0$ is presented in Fig. 3.1.3. The general pattern of the flow field is that the molten materials are going radially outward on the surface. As the flow approaches the edge of the molten pool, it goes down and turns around. It then moves to the center and comes up to complete the recirculation pattern. In addition to this recirculation, there is also the motion of the workpiece. Therefore, material enters the molten pool from the front part of the pool, goes through the recirculation pattern, ultimately resolidifying on the trailing edge.

c. Solid Redistribution: In order to help the reader to obtain a qualitative understanding of the mechanism of solute redistribution, a particle trajectory is plotted in Fig. 3.1.4. This trajectory is presented in three views; front, side, and top. The initial position is $(x_1^*, x_2^*, x_3^*) = (-2.97, 0.423, 0.01)$; a point very close to the surface and before the molten pool. The recirculating pattern of the particle can be clearly observed. This recirculating pattern implies that a particle will travel through a rather long path before it freezes into the resolidifying surface. Consequently, the molten materials can be well mixed. The composition within the melt pool is therefore uniform.

d. Temperature Field within the Molten Pool: The isotherms within the molten pool of the vertical planes at $x_1^* = 0$ and $x_2^* = 0$ are plotted in Figs. 3.1.5 and 3.1.6, respectively. x_1 is the scanning direction. The vertical plane at $x_1^* = 0$ therefore represents the cross-section of the molten pool directly under the laser beam. It can be observed that the isotherms in the vicinity of the solid-liquid interface are compressed near the surface of

the pool and stretched apart near the bottom due to existence of the flow field. This distortion is due to recirculation of molten material. The vertical plane $x_2^* = 0$ is the longitudinal section of the molten pool along the center line. The asymmetry of the isotherms and the solid-liquid interface can be observed. This distortion is due to the motion of the workpiece.

e. Cooling Rate: To visualize the heating and cooling of the materials as they scan pass underneath the laser, the temperature versus the scanning axis are plotted in Figs. 3.1.7 and 3.1.8. In Fig. 3.1.7, the family of the curves represents the temperature on the surface plane ($x_3^* = 0$). Each curve corresponds to a different value of x_2^* . On the other hand, the curves plotted in Fig. 3.1.8 are the temperature curves in the vertical plane along the centerline ($x_2^* = 0$). The melting temperature is also plotted in both figures. The cooling rate right after resolidification is related to the microstructure. The higher the cooling rate, the finer is the microstructure. It can be observed from the previous two graphs that the cooling rate (i.e. the temperature gradient) decreases from maximum the centerline to zero at the edge of the molten pool (Fig. 3.1.7) and also decreases from maximum on the surface to minimum at the bottom of the molten pool (Fig. 3.1.8). Such a variation in cooling causes a variation of the resolidified microstructure. Further investigation of the solidification mechanism is required to fully predict the resulting microstructure.

f. Pool Shape: The molten pool is greatly altered because of the presence of the fluid flow. It tends to make the molten pool wider and shallower. This effect is shown clearly in Fig. 3.1.9, where the solid-liquid interfaces at the vertical section ($x_1^* = 0.0$) for both pure conduction and

convection are plotted. The convection cases are tabulated in Table 3.1.1 (Case #1, 4, and 5). The Prandtl number is the only changing parameter among these cases. An increase in the Prandtl number signifies an increase in convection, thus, making the pool wider and shallower.

3.1.4 Conclusions

A perturbation model of the fluid flow and heat transfer of a laser melted pool is developed. Because of the fact that the recirculating flow is much greater than scanning speed, a perturbation is sought. The basic solution is the axisymmetric case and the perturbation is based on small scanning speed. The advantage is that the three-dimensional problem is represented by two sets of two-dimensional governing equations. It is found that the presence of the thermocapillary convection, the physics of the process changes from conduction to convection dominated. This changes the pool geometry dramatically, resulting in up to a 150 percent increase in the aspect ratio (width/depth) as compared to the pure conduction case. The temperature gradient on the resolidifying surface, which is directly proportional to the cooling rate, is found to be non-uniform. This in turn gives rise to the non-uniform resolidified microstructure. The mechanisms of solute redistribution is discussed qualitatively. It is found that a particle recirculates many, many times in the molten pool before it resolidifies. Consequently, the solute can be well mixed.

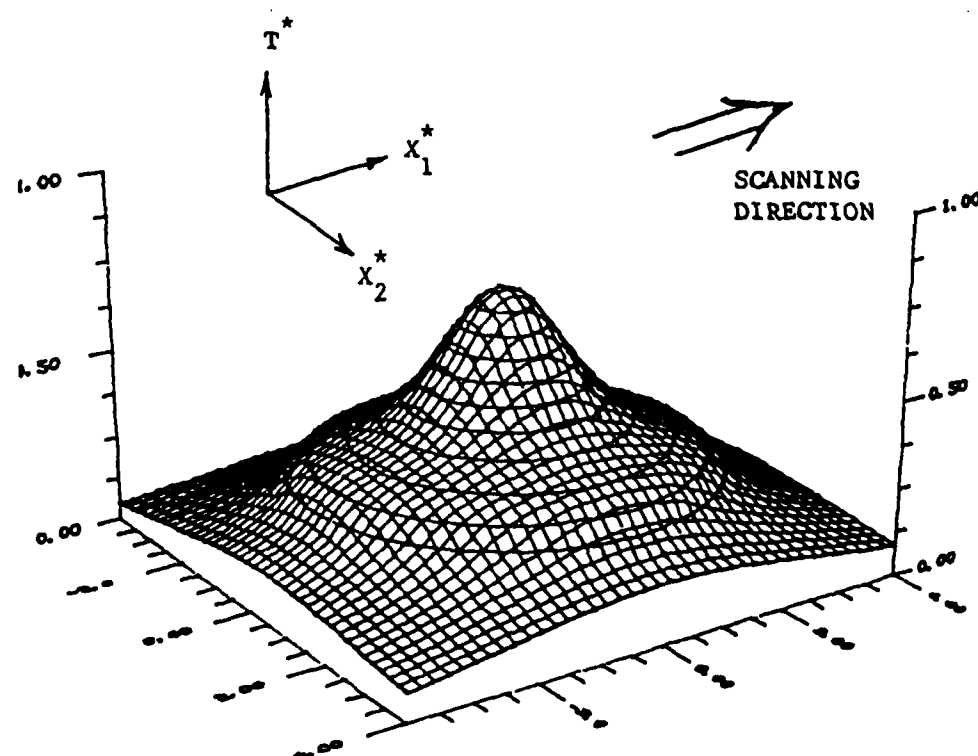


Figure 3.1.1 Three-dimensional plot of the surface temperature for $Ma = 1,500$, $Pr = 0.15$, $T^* = 0.25$ and $RF = 0.0$ (perturbation model)

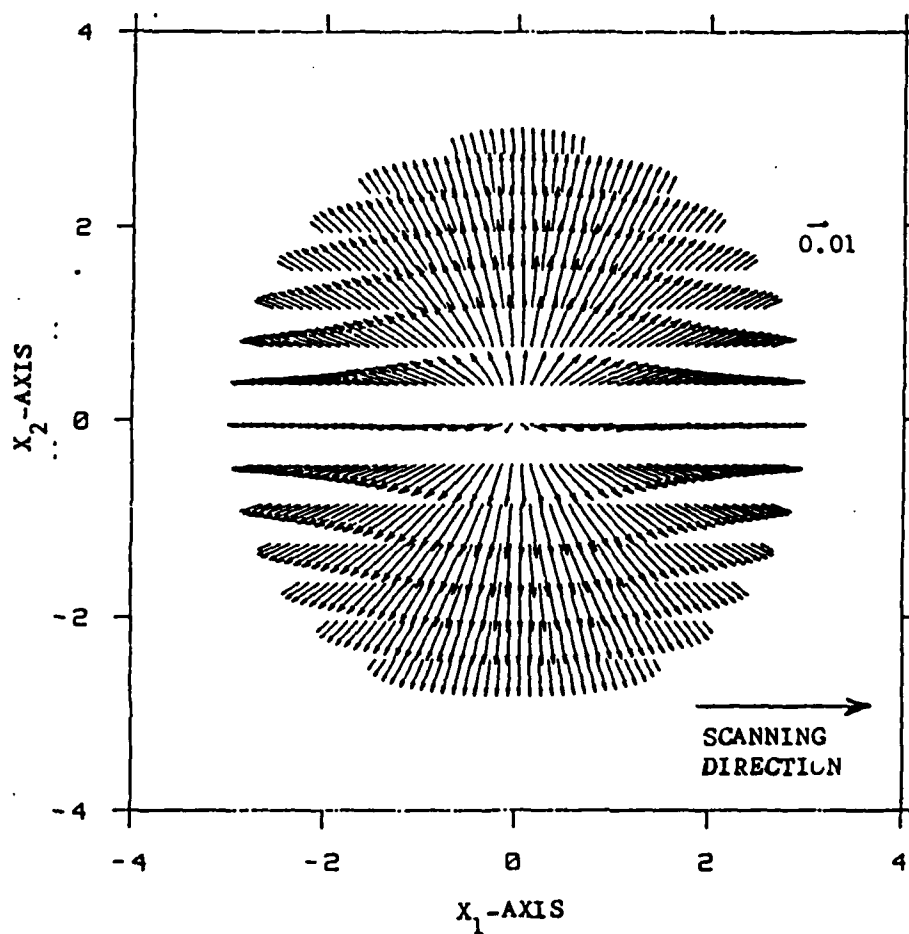


Figure 3.1.2 Velocity field on the surface plane for $Ma = 1,500$, $Pr = 0.15$, $T^* = 0.25$ and $RF = 0.0$ (perturbation model)

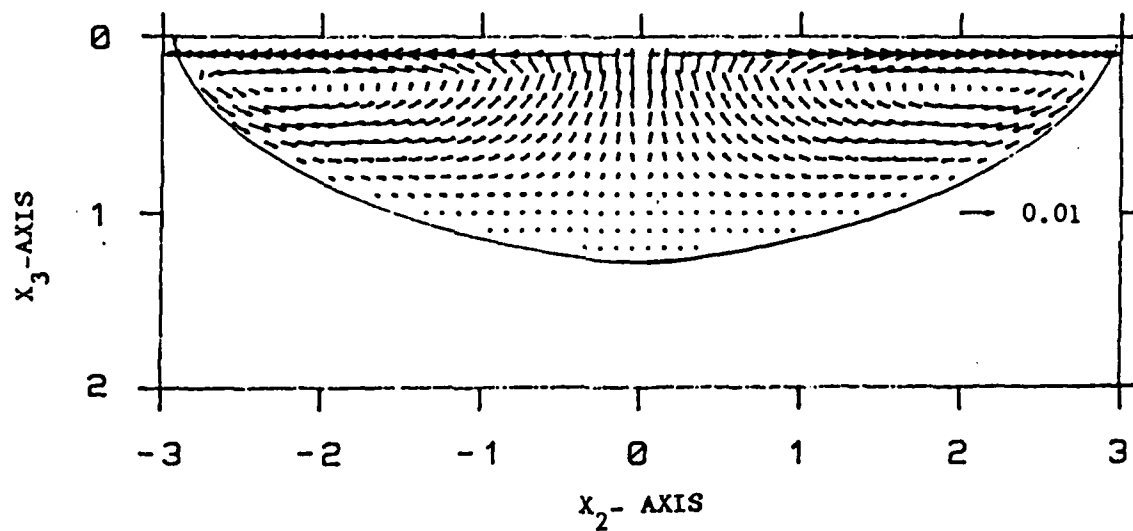


Figure 3.1.3 Velocity field on the vertical plane at $X_1^* = 0$ for
 $Ma = 1,500$, $Pr = 0.15$, $T^* = 0.25$ and
 $RF = 0.0$ (perturbation model)

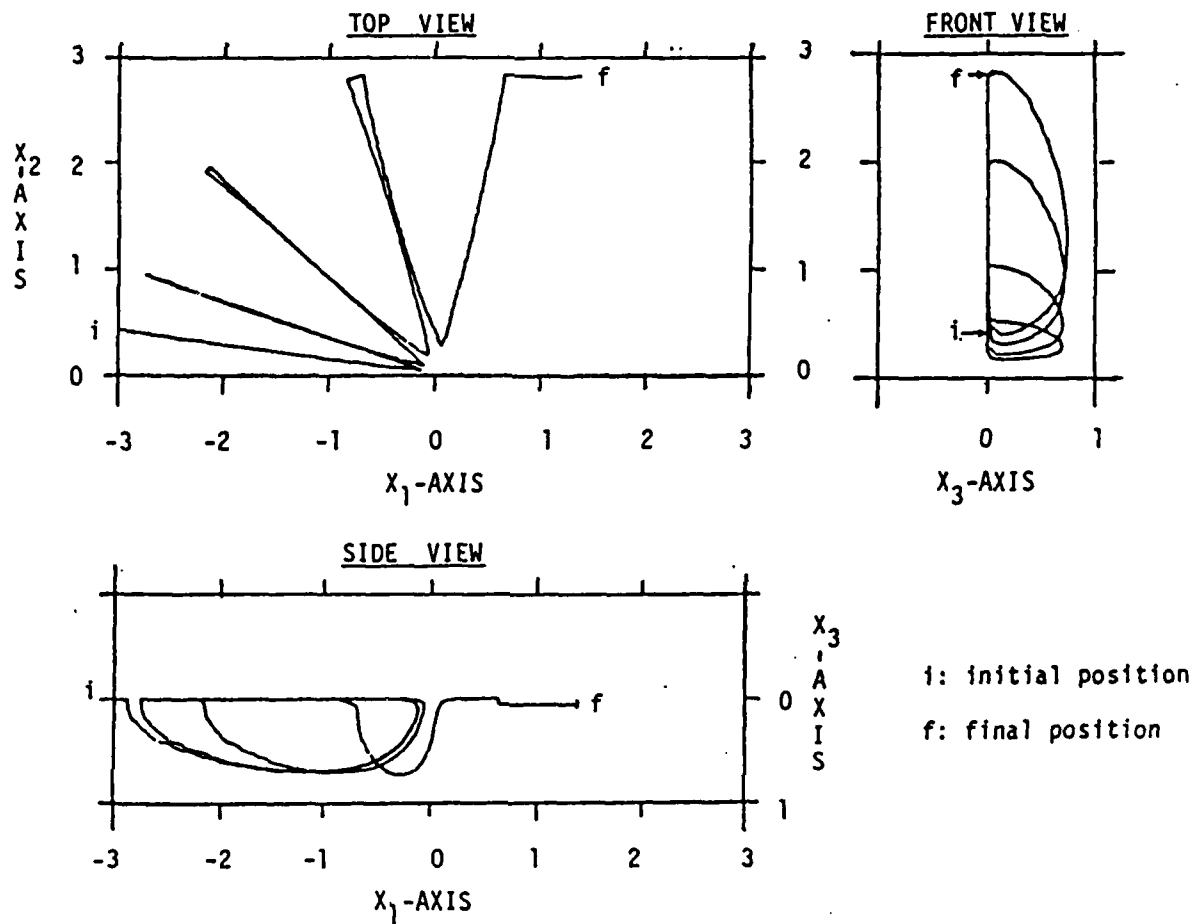


Figure 3.1.4 Trajectory of a particle as it enters, recirculates and ultimately freezes. The trajectory is plotted in front, side, and top view in (a), (b), and (c), respectively. Initial position is $(X_1^*, X_2^*, X_3^*) = (-2.97, 0.0423, 0.01)$ $Ma = 1,500$, $Pr = 0.15$, $f_m^* = 0.25$ and $RF = 0.0$ (perturbation model)

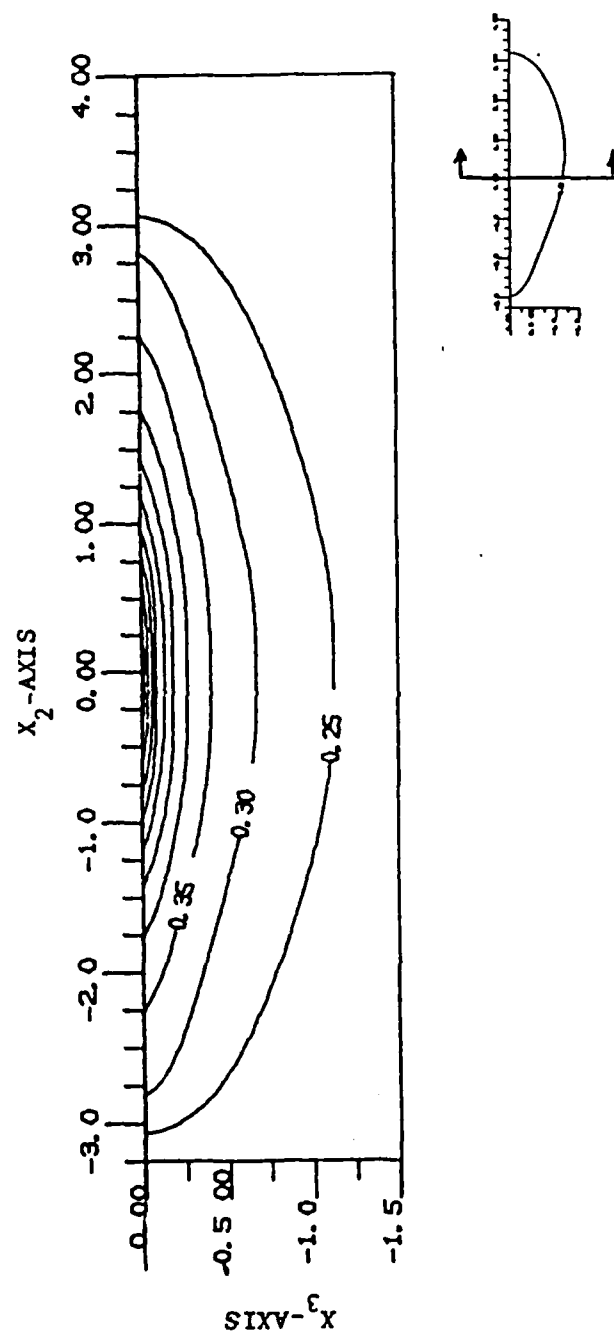


Figure 3.1.5 Isotherms within the molten pool on the vertical plane $X^* = 0.05$ for $Ma = 1,500$, $Pr = 0.15$, $T_m^* = 0.25$ and $Rf = 0.0$ (perturbation model)

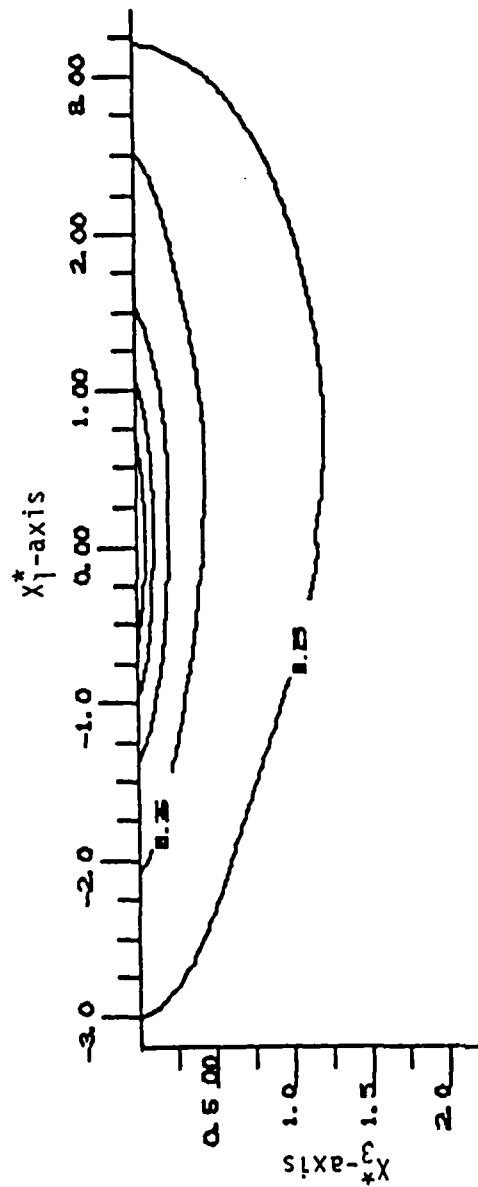


Figure 3.1.6 Isotherms within the molten pool on the vertical plane at $X_2^* = 0.0$ for $Ma = 1,500$, $Pr = 0.15$, $T_m^* = 0.25$ and $RF = 0.0$ (perturbation model)

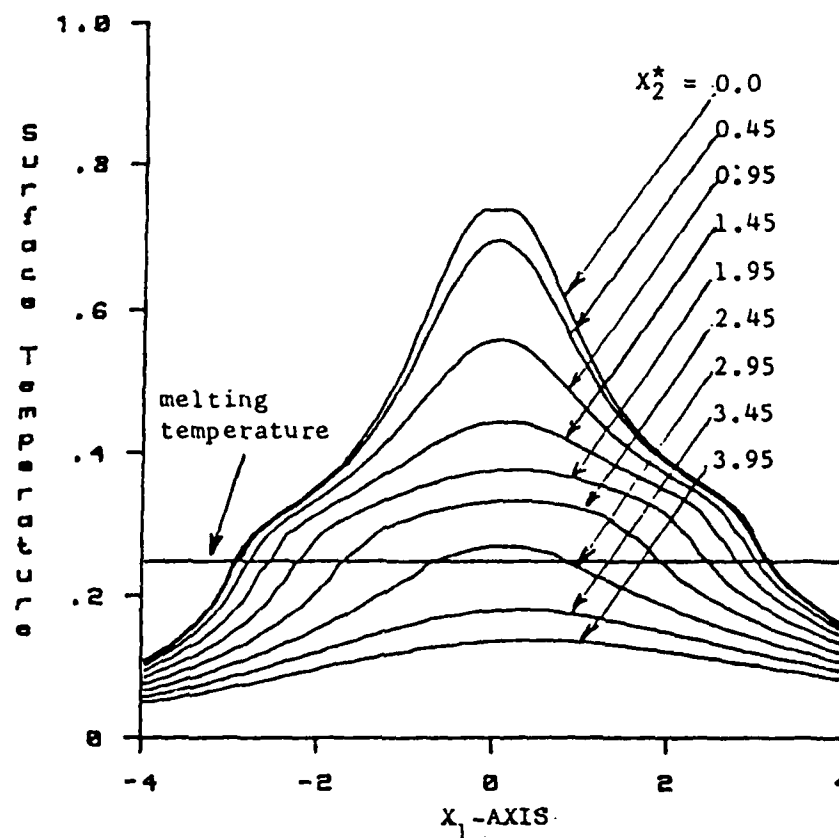


Figure 3.1.7 Family curves represent the surface temperature. Each curve corresponds to a different value of X_2^* for $Ma = 1,500$, $Pr = 0.15$, $T^* = 0.25$, and $RF = 0.0$ (perturbation model)

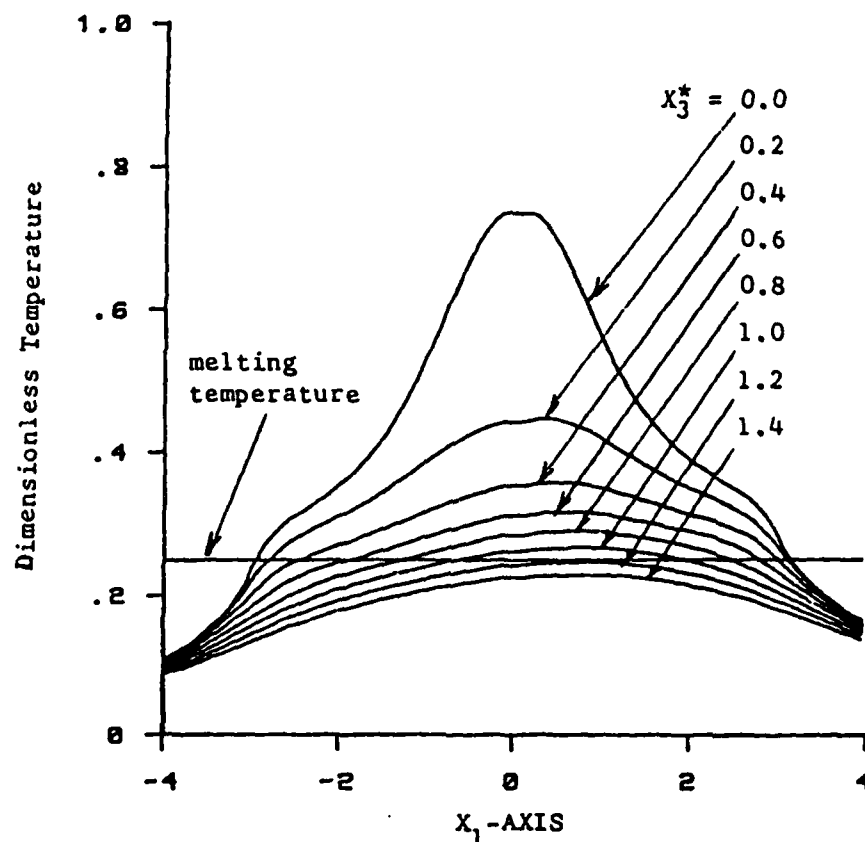


Figure 3.1.8 Family curves of the temperature in a vertical plane ($X_2^* = 0$). Each curve corresponds to a different value of X_3^* . $Ma = 1,500$, $Pr = 0.15$, $T_m^* = 0.25$ and $RF = 0.0$ (perturbation model)

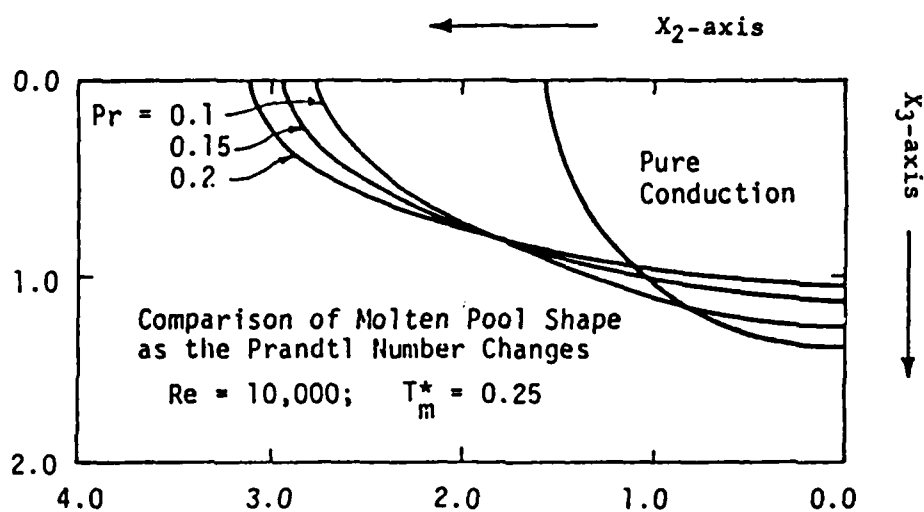


Figure 3.1.9 Comparison of the shape of the molten pool for different Prandtl number (perturbation model)

Table 3.1.1 The Numerical Values of the Dimensionless Parameters
of the Nine Cases of the Three-Dimensional Model

	1	2	3	4	5
Re	10,000	30,000	30,000	10,000	10,000
Pr	0.15	0.15	0.015	0.1	0.2
Ma	1,500	4,500	450	1,000	2,000
T_m^*	0.25	0.3	0.3	0.25	0.25
RF	0.0	0.0	0.0	0.0	0.0
	6	7	8	9	
Re	5,000	5,000	5,000	10,000	
Pr	0.10	0.15	0.2	0.015	
Ma	500	750	1,000	150	
T_m^*	0.25	0.25	0.25	0.25	
RF	0.0	0.0	0.0	0.0	

3.2 Stagnation Flow Analysis

3.2.1 Introduction

In this section, a generalized solution for the thermocapillary flow and convection of the liquid melt under an intense, non-uniform heat source, is considered. When a concentrated heat source is applied to a free surface of a molten material, the resulting temperature distribution causes a non-uniform surface tension distribution. Being a decreasing function of temperature for most liquid metal, the surface tension gradient will therefore pull the liquid from the warmer, central region to the cooler, outer region at the surface. This shearing motion entrains fluid toward the surface at the center, forming viscous and thermal boundary layers if the fluid is deep enough. Such flows are the dominant features in the central region of the melt pools during laser materials processing processes such as laser surface alloying and rapid-solidification by laser melt quenching [15,27]. Similar flows, with a different geometry are also found in crystal growth processes using zone melting and similar methods [29]. The physical model is shown in Fig. 3.2.1. Both two-dimensional and axisymmetric cases are considered. The two-dimensional case represents the limiting case of the flows encountered in zone melting crystal growth, when the heat source dimension is small with respect to the radius. The axisymmetric case represents the limiting case of the flows encountered in welding, laser surface alloying and rapid-solidification by laser melt quenching when the scanning velocity is small relative to the velocity of the thermocapillary motion. This investigation is to focus on the basic features of the flow in the central region where the structure is very much like the stagnation flow. The theory approximates the surface heat flux distribution near the center by a parabola, and invokes the

boundary layer approximation for the energy equation, but not for the momentum equation. The governing coupled partial differential equations are transformed to a set of decoupled ordinary differential equations. Analytical solutions are found for some conditions. Numerical solutions are sought for other conditions. These results provide the basic scaling laws for thermocapillary convection in a deep melt pool. Explicit formulas are obtained for the scalings of the physical quantities such as velocity, temperature, surface temperature gradient, and viscous and thermal boundary layers. Because of the intrinsic coupling of the momentum and energy equations of thermocapillary convection, these scalings depend on the Prandtl number. This dependence is obtained by computations of the energy equations for various Prandtl numbers near unity. The limiting cases of large and small Prandtl numbers are also analyzed. The results complete the understanding of scaling laws dependence on the Prandtl numbers. These asymptotic analyses also yield explicit and concise solutions and scalings within the respective ranges. It is found that the asymptotic results give good approximation for moderate values of the Prandtl numbers as compared to the numerical results of the case $Pr \sim O(1)$.

3.2.2 Formulation

The governing equations are given below, for detail derivation refer to Ref. [42].

$Pr \sim O(1)$

$$f_1''' + (m-1) f_1 f_1'' - f_1'^2 = 0 \quad (3.2.1)$$

$$\tilde{g}_0'' + \text{Pr } \tilde{f}_1 \tilde{g}_0' = 0 \quad (3.2.2)$$

$$\tilde{g}_1'' + \text{Pr } [\tilde{f}_1 \tilde{g}_1' - 2 \tilde{f}_1' \tilde{g}_1] = 0 \quad (3.2.3)$$

the boundary conditions are,

$$\tilde{z} = 0; \tilde{f}_1 = 0, \tilde{f}_1'' = -1, \tilde{g}_0' = \tilde{g}_1' = -1 \quad (3.2.4)$$

$$\tilde{z} \rightarrow \infty \quad \tilde{f}_1' = \tilde{g}_0 = \tilde{g}_1 = 0.$$

$\text{Pr} \rightarrow 0$

$$\tilde{g}_0^{0''} + \tilde{f}_\infty \tilde{g}_0^{0'} = 0, \quad (3.2.5)$$

$$\tilde{g}_0^{0''} + \tilde{f}_\infty \tilde{g}_1^{0'} - 2 \tilde{f}_\infty \delta(\tilde{z}^0) \tilde{g}_1^0 = 0 \quad (3.2.6)$$

where $\delta(\tilde{z}^0)$ is the Dirac delta function and $\tilde{f}_\infty = \tilde{f}_1(\infty)$ is a constant and listed in Table 3.2.1.

the boundary conditions are,

$$\tilde{z}^0 = 0, \tilde{g}_0^{0'} = \tilde{g}_1^{0'} = -1, \quad (3.2.7)$$

$$\tilde{z}^0 \rightarrow \infty, \quad \tilde{g}_1^0 = \tilde{g}_1^{0'} = 0.$$

$\text{Pr} \rightarrow \infty$

$$\tilde{g}_0^{i''} + \tilde{f}_{10}' \tilde{z}^i \tilde{g}_0^{i'} = 0, \quad (3.2.8)$$

$$\tilde{g}_1^{i''} + \tilde{f}_{10}' \tilde{z}^i \tilde{g}_1^{i'} - 2 \tilde{f}_{10}' \tilde{g}_1^i = 0 \quad (3.2.9)$$

where $\tilde{f}_{10}' \equiv \tilde{f}_1'(0)$ is a constant tabulated in Table 3.2.1.

the boundary conditions are,

$$\tilde{z}^i = 0; \quad \tilde{g}_0^i = \tilde{g}_1^i = -1,$$

$$\tilde{z}^i \rightarrow \infty; \quad \tilde{g}_0^i = \tilde{g}_1^i = 0. \quad (3.2.10)$$

3.2.3 Results and Discussion

a. $Pr \sim 0$ (1): The universal stream function \tilde{f}_1 , velocity profile \tilde{f}_1' , and shear stress \tilde{f}_1'' for both two-dimensional and axisymmetric cases are plotted in Fig. 3.2.2. The behavior of the stream function is quite different from the conventional stagnation flow. In the case of thermocapillary flow, the fluid flow is driven by the surface tension gradient on the free surface. Consequently, the shear stress is negative with maximum magnitude on the free surface and diffuses into the liquid. The velocity, u_r , is non-zero on the surface. In fact, it is maximum here and decreases exponentially with the depth. The scaled temperature functions \tilde{g}_0 and \tilde{g}_1 for various Prandtl numbers are plotted in Figs. 3.2.3 through 3.2.10 for two-dimensional and

axisymmetric cases. The scaled temperature functions decrease very rapidly from their maximum values on the surface. The maximum values which exist on the surface increase as the Prandtl number decreases. This is because the smaller the Prandtl number, the smaller is the convection, less heat being brought sideways, hence the higher is the temperature.

The decoupling of the system by simple rescaling means that the coupling effect of the heat transfer and momentum is by a multiplication factor. This can be seen easily by writing the viscous boundary layer scale, velocity, the maximum temperature, and the heat transfer coefficient explicitly as:

$$\delta_v = \left(\frac{k_{\mu\nu}}{2\gamma' q_1} \right)^{\frac{1}{4}} \tilde{g}_{10}^{-\frac{1}{4}} \quad (3.2.11)$$

$$\begin{aligned} u_r &= \frac{v}{\left(\frac{k_{\mu\nu}}{2\gamma' q_1} \right)^{\frac{1}{4}} \tilde{g}_{10}^{-\frac{1}{4}}} r f'_1(\tilde{z}) \\ &= q_1^{\frac{1}{2}} \tilde{g}_{10}^{\frac{1}{2}} \left(\frac{2\gamma'}{k_0} \right)^{\frac{1}{2}} r f'_1(\tilde{z}) \end{aligned} \quad (3.2.12)$$

$$\begin{aligned} \Delta T_{\max} &= \frac{q_0}{k} \left(\frac{k_{\mu\nu}}{2\gamma' q_1} \right)^{\frac{1}{4}} \tilde{g}_{10}^{-\frac{1}{4}} \tilde{g}_0(0) \\ &= \frac{q_0 \tilde{g}_0(0)}{q_1^{\frac{1}{4}} \tilde{g}_{10}^{\frac{1}{4}}} \left(\frac{\mu\nu}{2k^3 \gamma'} \right)^{\frac{1}{4}} \end{aligned} \quad (3.2.13)$$

\tilde{g}_{10} appears in all these quantities. \tilde{g}_{10} is a measure of the surface temperature non-uniformity. In particular, it is the second derivative (with respect to r) of the surface temperature. This is introduced into the non-dimensionalization to decouple the system. Thus the coupling of the energy and momentum equations is solely embodied in this term. \tilde{g}_{10} is a function of

the Prandtl number and is graphically presented in Fig. 3.2.11 for both two-dimensional and axisymmetric cases. $\tilde{g}_0(0)$ denotes the dimensionless surface temperature at the center ($r = 0$) and therefore is directly related to the maximum temperature. Naturally, $\tilde{g}_0(0)$ is also a function of the Prandtl number and is plotted in Fig. 3.2.12. The surface temperature gradient can be obtained by taking the derivative of the temperature with respect to r and then by substituting in the scalings. It is found to be:

$$\begin{aligned} \left. \frac{\partial T}{\partial r} \right|_{z=0} &= \frac{2 q_1}{k} \left(\frac{k_{\mu\nu}}{2\gamma' q_1} \right)^{1/4} \tilde{g}_{10}^{3/4} r \\ &= 2 q_1^{3/4} \tilde{g}_{10}^{3/4} \left(\frac{\mu\nu}{2k^3 \gamma'} \right)^{1/4} r \end{aligned} \quad (3.2.14)$$

The dependence of all the scalings on the temperature coefficient of surface tension, and other thermophysical properties are expressed explicitly in Eqs. (3.2.1) through (3.2.4). As mentioned earlier, \tilde{g}_{10} appears in all of the scalings, and it is a function of the Prandtl number. The complete understanding of the scalings required the asymptotic analyses of small and large Prandtl numbers which are presented in the following two sections.

b. $Pr \rightarrow 0$: The dimensionless functions $\tilde{g}_0^0(\tilde{z}^0)$ and $\tilde{g}_1^0(\tilde{z}^0)$ are plotted in Fig. 3.2.13. This limiting analysis provides explicit formulas for the Prandtl number effect on the scaling laws. The scaling introduced for $\tilde{g}_1(\tilde{z})$ [42] implies that the viscous length scale is:

$$\tilde{\delta}_v = \left(\frac{k_{\mu\nu}}{2\gamma' q_1} \right)^{1/4} \tilde{g}_{10}^0{}^{-1/4} Pr^{1/4} \quad (3.2.15)$$

This viscous length scale can be rewritten as:

$$\tilde{\delta}_v = q_1^{-1/4} \tilde{g}_{10}^0^{-1/4} \left(\frac{\rho^2 C_p v^3}{2 \gamma'} \right)^{1/4} \quad (3.2.16)$$

Thus, the viscous boundary layer is proportional to $v^{3/4}$. The ratio of the thermal length scale and viscous length scale is,

$$\tilde{\delta}_\kappa / \tilde{\delta}_v = Pr^{-1} \quad (3.2.17)$$

so that

$$\begin{aligned} \tilde{\delta}_\kappa &= \left(\frac{k_{\mu v}}{2 \gamma' q_1} \right)^{1/4} \tilde{g}_{10}^0^{-1/4} Pr^{-3/4} \\ &= q_1^{-1/4} \tilde{g}_{10}^0^{-1/4} k \left(\frac{1}{2 \rho^2 C_p^3 \gamma' v} \right)^{1/4} \end{aligned} \quad (3.2.18)$$

The same Prandtl number dependence is found for the temperature. In particular, the maximum temperature difference which occurs on the surface at the center can be obtained. Substituting the scaling for g_0 , we have,

$$\begin{aligned} \Delta T_{\max} &= \frac{q_0}{k} \left(\frac{k_{\mu v}}{2 \gamma' q_1} \right)^{1/4} \frac{\tilde{g}_0^0(0) Pr^{-3/4}}{\tilde{g}_1^0(0)^{1/4}} \\ &= \frac{q_0}{q_1^{1/4}} \cdot \frac{\tilde{g}_0^0(0)}{\tilde{g}_{10}^0^{1/4}} \cdot \left(\frac{1}{2 \rho^2 \gamma' C_p^3 v} \right)^{1/4} \end{aligned} \quad (3.2.19)$$

The driving force of the flow field, the surface temperature can be shown to be,

$$\begin{aligned}
 \left. \frac{\partial T}{\partial r} \right|_{r=0} &= \frac{2 q_1}{k} \left(\frac{k_{\mu\nu}}{2 \gamma' q_1} \right)^{1/4} \tilde{g}_{10}^0{}^{3/4} Pr^{-3/4} \cdot r \\
 &= 2 q_1^{3/4} \tilde{g}_{10}^0{}^{3/4} \left(\frac{1}{2 \rho^2 \gamma' C_p^3 v} \right)^{1/4} r
 \end{aligned}
 \tag{3.2.20}$$

The velocity in the radial direction is

$$\begin{aligned}
 u_r &= \frac{v}{\left(\frac{k_{\mu\nu}}{2 \gamma' q_1} \right)^{1/2} \tilde{g}_{10}^0{}^{-1/2}} \frac{1}{Pr^{1/2}} r \tilde{f}_1'(\tilde{z}) \\
 &= q_1^{1/2} \tilde{g}_{10}^0{}^{1/2} \tilde{g}_{10}^0{}^{1/2} \cdot \left(\frac{2 \gamma' v}{\rho C_p} \right)^{1/2} r \tilde{f}_1'(\tilde{z})
 \end{aligned}
 \tag{3.2.21}$$

The vertical velocity, u_z , can be derived from the continuity equation:

$$\begin{aligned}
 u_z &= \frac{(m-1) v Pr^{-1/4}}{\left(\frac{k_{\mu\nu}}{2 \gamma' q_1} \right)^{1/4} \tilde{g}_{10}^0{}^{-1/4}} \tilde{f}_1(\tilde{z}) \\
 &= (m-1) q_1^{1/4} \tilde{g}_{10}^0{}^{1/4} \left(\frac{2 \gamma' v}{\rho C_p} \right)^{1/4} \tilde{f}_1(\tilde{z})
 \end{aligned}
 \tag{3.2.22}$$

The shear stress can be obtained by differentiating u_r with respect to z in Eq. (3.2.11)

$$\begin{aligned}
 \mu \frac{\partial u_r}{\partial z} &= \mu \nu \left(\frac{k_{\mu\nu}}{2\gamma' q_1} \right)^{-3/4} \tilde{g}_{10}^0 \text{Pr}^{-3/4} r \\
 &= q_1^{3/4} \tilde{g}_{10}^0 \mu \left(\frac{2\gamma' \nu}{\rho C_p} \right)^{3/4} r
 \end{aligned}
 \tag{3.2.23}$$

\tilde{g}_{10}^0 , which appears in the above equations, is a constant tabulated in Table 3.2.2 for both two-dimensional and axisymmetric cases.

c. $\text{Pr} \rightarrow \infty$: The dimensionless functions $\tilde{g}_0^i(\tilde{z}^i)$ and $\tilde{g}_1^i(\tilde{z}^i)$ for the two-dimensional and axisymmetric cases are plotted in Fig. 3.2.14. The solutions behave as expected, attaining their maximum on the surface and decreasing very rapidly downward.

Similarly, this asymptotic limit provides the explicit formula for the effect of the Prandtl number on the scaling laws for large Pr . The viscous length scale is:

$$\begin{aligned}
 \tilde{\delta}_v &= \left(\frac{k_{\mu\nu}}{2\gamma' q_1} \right)^{1/4} \tilde{g}_{10}^i^{-1/4} \text{Pr}^{1/8} \\
 &= q_1^{-1/4} \tilde{g}_{10}^i^{-1/4} \left(\frac{k_{\mu}^2 \nu^3 \rho C_p}{4 \gamma'^2} \right)^{1/8}
 \end{aligned}
 \tag{3.2.24}$$

The ratio of the thermal length scale and viscous length scale is:

$$\frac{\tilde{\delta}_\kappa}{\tilde{\delta}_v} = \text{Pr}^{-1/2}
 \tag{3.2.25}$$

so that

$$\begin{aligned}\tilde{\delta}_\kappa &= \left(\frac{k_{\mu\nu}}{2\gamma' q_1}\right)^{1/4} \tilde{g}_{10}^i{}^{-1/4} Pr^{-3/8} \\ &= q_1^{-1/4} \tilde{g}_{10}^i{}^{-1/4} \left(\frac{k^5 \mu^2}{4 \gamma'^2 \nu \rho^3 C_p^3}\right)^{1/8}\end{aligned}\quad (3.2.26)$$

It is interesting to compare this high Prandtl number limit of the $\tilde{\delta}_\kappa/\tilde{\delta}_\nu$ ratio of the present model to that of the common forced convection. The limit for common forced convection case is $\tilde{\delta}_\kappa/\tilde{\delta}_\nu \propto Pr^{-1/3}$. This difference is a result of the non-zero velocity on the surface so that the stream function behaves linearly in z for small z . On the other hand, the common forced convection problem has the no-slip condition so that the stream function behaves quadratically in z for small z . The maximum temperature difference is found to be,

$$\begin{aligned}\Delta T_{\max} &= \frac{q_0}{k} \left(\frac{k_{\mu\nu}}{2\gamma' q_1}\right)^{1/4} \frac{\tilde{g}_0^i(0) Pr^{-3/8}}{\tilde{g}_{10}^i{}^{1/4}} \\ &= \frac{q_0}{q_1^{1/4}} \cdot \frac{\tilde{g}_0^i(0)}{\tilde{g}_{10}^i{}^{1/4}} \cdot \left(\frac{\nu}{4 \rho k^3 C_p^3 \gamma'^2}\right)^{1/8}\end{aligned}\quad (3.2.27)$$

the surface temperature gradient is,

$$\begin{aligned}\frac{\partial T}{\partial r}\bigg|_{z=0} &= \frac{2 q_1}{k} \left(\frac{k_{\mu\nu}}{2\gamma' q_1}\right)^{1/4} \tilde{g}_{10}^i{}^{3/4} Pr^{-3/8} \cdot r \\ &= 2 q_1^{3/4} \tilde{g}_{10}^i{}^{3/4} \left(\frac{\nu}{4 \rho k^3 C_p^3 \gamma'^2}\right)^{1/8} \cdot r\end{aligned}\quad (3.2.28)$$

the radial velocity is,

$$u_r = \frac{v}{\left(\frac{k_{uv}}{2\gamma'q_1}\right)^{1/2} \tilde{g}_{10}^i} Pr^{-1/4} r \tilde{f}'_1(\tilde{z}) \quad (3.2.29)$$

$$= q_1^{1/4} \tilde{g}_{10}^{i1/2} \left(\frac{4\gamma'^2}{\rho^3 C_p k_v}\right)^{1/4} \tilde{r}_1 f^r(z)$$

the vertical velocity is,

$$u_z = \frac{(m-1) v Pr^{-1/8}}{\left(\frac{k_{uv}}{2\gamma'q_1}\right)^{1/4} \tilde{g}_{10}^i} \tilde{f}_1(\tilde{z}) \quad (3.2.30)$$

$$= (m-1) \cdot q_1^{1/4} \tilde{g}_{10}^{i-1/4} \left(\frac{4\gamma'^2 v^3}{k_o^3 C_p}\right)^{1/8}$$

and the shear force is,

$$\mu \frac{\partial u_r}{\partial z} = \mu v \left(\frac{k_{uv}}{2\gamma'q_1}\right)^{-3/4} \tilde{g}_{10}^{i3/4} Pr^{-3/8} r \quad (3.2.31)$$

$$= q_1^{3/4} \tilde{g}_{10}^{i3/4} \mu v \left(\frac{4\gamma'^2}{k_{\mu}^2 v^3 \rho C_p}\right)^{3/8}$$

\tilde{g}_{10}^i is a constant tabulated in Table 3.3.2 for both two-dimensional and axisymmetric cases. \tilde{g}_{10} for the whole range of Pr , which is necessary for the scaling laws, is also presented graphically in Fig. 3.2.15 for both two-dimensional and axisymmetric cases. The maximum temperature as a function of the Prandtl number, including both high and low Pr limits, is plotted in Fig. 3.2.16. The asymptotic limits are reflected in the graph (log-log plot) as two straight lines of slopes, $-1/2$ and -1 , respectively. It can be observed that the two asymptotic limits give with reasonable predictions of these quantities. For $Pr \leq .15$, the maximum errors of the low Pr limit prediction for both $\tilde{g}_0(0)$ and $\tilde{g}_1(0)$ are less than 10 percent. For $Pr \geq 10.0$, the maximum errors of the high Pr limit prediction for both $\tilde{g}_0(0)$ and $\tilde{g}_1(0)$ are also less than 10 percent.

d. Comparison to Numerical Solution: The stagnation flow analysis presented in this section is the dominant feature of the thermocapillary convection in melt pool. This model represents a common feature of thermocapillary convection in the melt pool in the vicinity of the central region underneath the heat source. In order to examine the validity of the model, this stagnation flow analysis results are compared to the numerical results of the axisymmetric case presented in the last chapter.

i. Velocity Profile

The universal velocity profile of the stagnation flow analysis is plotted in Fig. 3.2.17. The velocity profile obtained from the perturbation model (case #2 in Table 3.1.1) are plotted also in Fig. 3.2.17 to provide the comparisons among themselves as well as to the stagnation flow analysis

result. The comparison shows that the surface velocities predicted by the two theories are within 10 percent. These predicted velocity profiles are also similar. The returned flow velocity at the bottom part of the pool which is neglected in the stagnation flow analysis is predicted to be of one order of magnitude less than the surface velocity by the numerical solution. The stagnation flow analysis predicted that the velocity profile is directly proportional to r . It can be observed that the curves f^+ versus \bar{z} for different values of r^* of the numerical solutions are essentially one curve.

ii. Centerline Temperature

The centerline temperature predicted by the stagnation flow analysis (i.e. $\tilde{g}_0(\bar{z})$ versus \bar{z} for $Pr = 0.15$) is plotted in Fig. 3.2.18. This centerline temperature of case #2 (Table 3.1.1) is also plotted in Fig. 3.2.18 for comparison of the two predictions. The stagnation flow analysis predicts a high surface temperature, 10 percent higher than the numerical solution. This is expected since the boundary layer approximation is invoked for the energy equation so that the radial conduction is not taken into consideration. The centerline temperature drops more rapidly in the case of the stagnation flow analysis. This is because of the fact that the stagnation flow analysis is based on the boundary layer approximation of the energy equation and the assumption of semi-infinite domain. The thermocapillary convection, in the case of stagnation flow analysis, since there are no return flow, carries all the heat from the heat source sideways. However, in the case of the numerical solution, there is a return flow which convects part of the heat back.

iii. Maximum Temperature

The maximum temperature, which occurs at $r^* = z^* = 0$, of all the numerical solution cases and stagnation flow analysis are plotted in Fig. 3.2.19. The stagnation flow analysis is predicting the maximum temperature quite accurately (within 10%) for $Pr = 0.10, 0.15$, and 0.2 . However, the stagnation flow analysis is predicting a much higher temperature for small Prandtl number ($Pr = 0.015$). This is due to the boundary layer approximation on the energy equation. In essence, the radial conduction is neglected.

3.2.4 Conclusions

A generalized solution for the thermocapillary convection in the central region of the liquid melt pool directly underneath an intense non-uniform heat source is obtained for both two-dimensional and axisymmetric cases. The system of coupled partial differential equations is transformed into a set of decoupled ordinary differential equations. By doing so, a universal stream function (velocity profile) is obtained. The rescaled temperature field is solved for various Prandtl numbers. The effects of the coupling of the temperature and the velocity fields are characterized by scalings. The term \tilde{g}_{10} , appeared in all of these scalings, represents the leading order term of the temperature non-uniformity on the surface and varies with respect to the Prandtl numbers. Quantitative dependence of \tilde{g}_{10} on the Prandtl numbers is obtained and it is presented graphically. This analysis also yields explicit formulas of physical quantities such as maximum temperature, velocity, shear stress, and viscous boundary layer length scale. These expressions are presented in Eqs. (3.2.1) through (3.2.4). Their dependences on thermophysical properties are explicitly defined. The two asymptotic

limits of small and large Prandtl numbers provide concise formulas for these dependences in the respective ranges. These two asymptotic limits also yield explicit, simple, and concise formulas for the physical quantities such as maximum temperature, second derivative of the surface temperature, velocity, shear stress, thermal boundary layer length scale, and viscous boundary layer length scale. These expressions are presented in Eqs. (3.2.5) through (3.2.13) and Eqs. (3.2.14) through (3.2.21) for small and large Prandtl numbers, respectively.

The results of the present stagnation flow analysis are also compared with the numerical solutions of the base flow of the perturbation model. The results of the numerical solutions are plotted in the stagnation flow analysis variables. It is found that the stagnation flow analysis predictions are close to the numerical solutions. Thus, the simple algebraic formulas of the stagnation flow analysis can be used to predict various physical quantities such as the maximum temperature and the velocity.

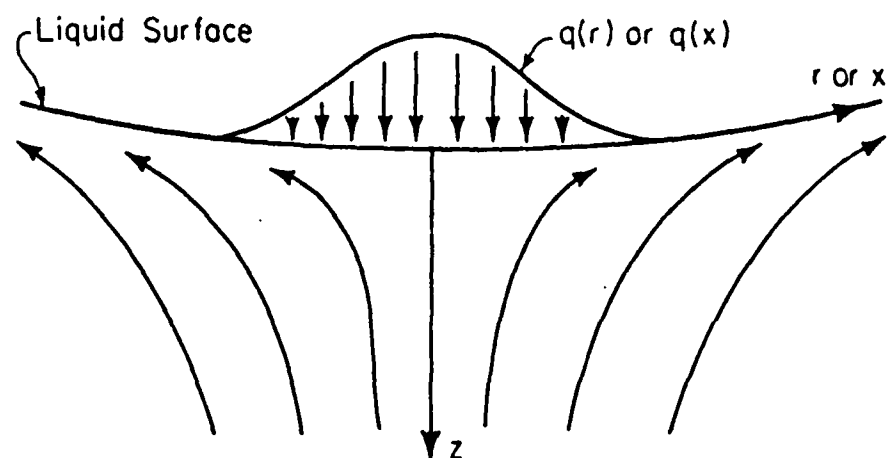


Figure 3.2.1 Schematic Diagram of the Physical Model of the Stagnation Flow Analysis

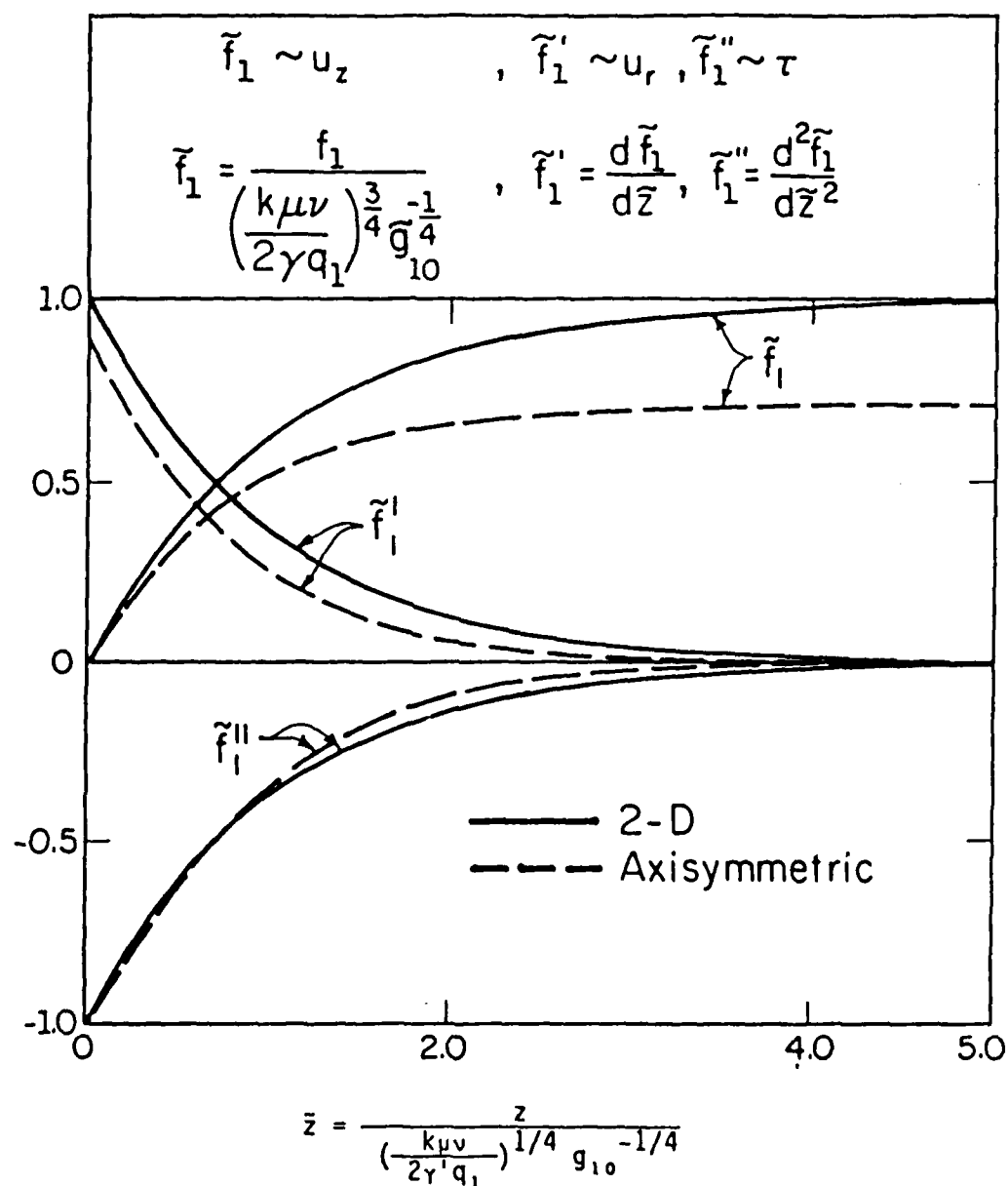


Figure 3.2.2 Graphs of the Stream Function \tilde{f}_1 , the Velocity Profile \tilde{f}_1' , and the Shear Stress \tilde{f}_1'' versus the Depth for both Two-Dimensional and Axisymmetric Cases (Stagnation Flow Analysis)

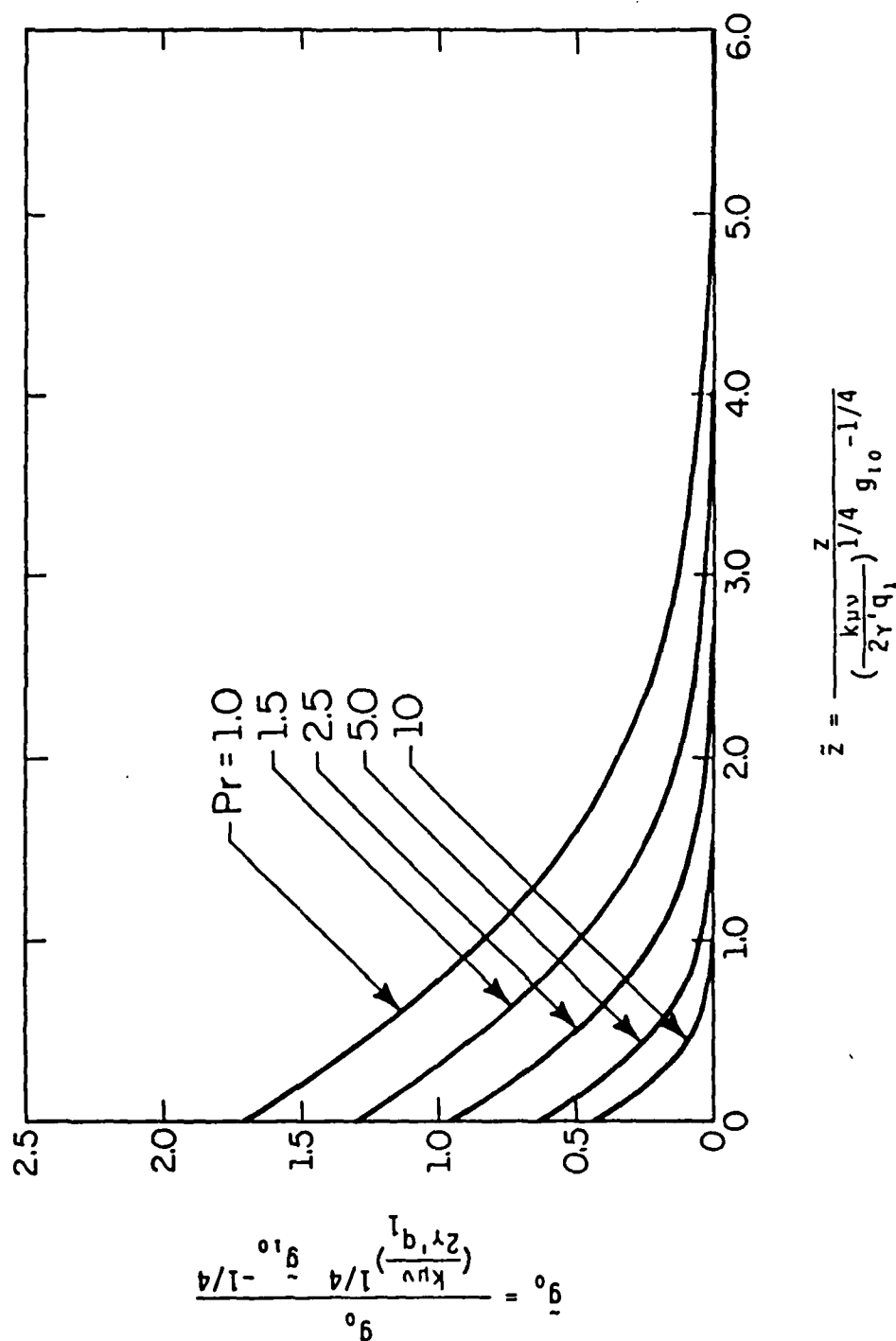


Figure 3.2.3 Graphs of \bar{g}_0 versus the Depth of the Two-Dimensional Case for Various Prandtl Numbers (> 1)

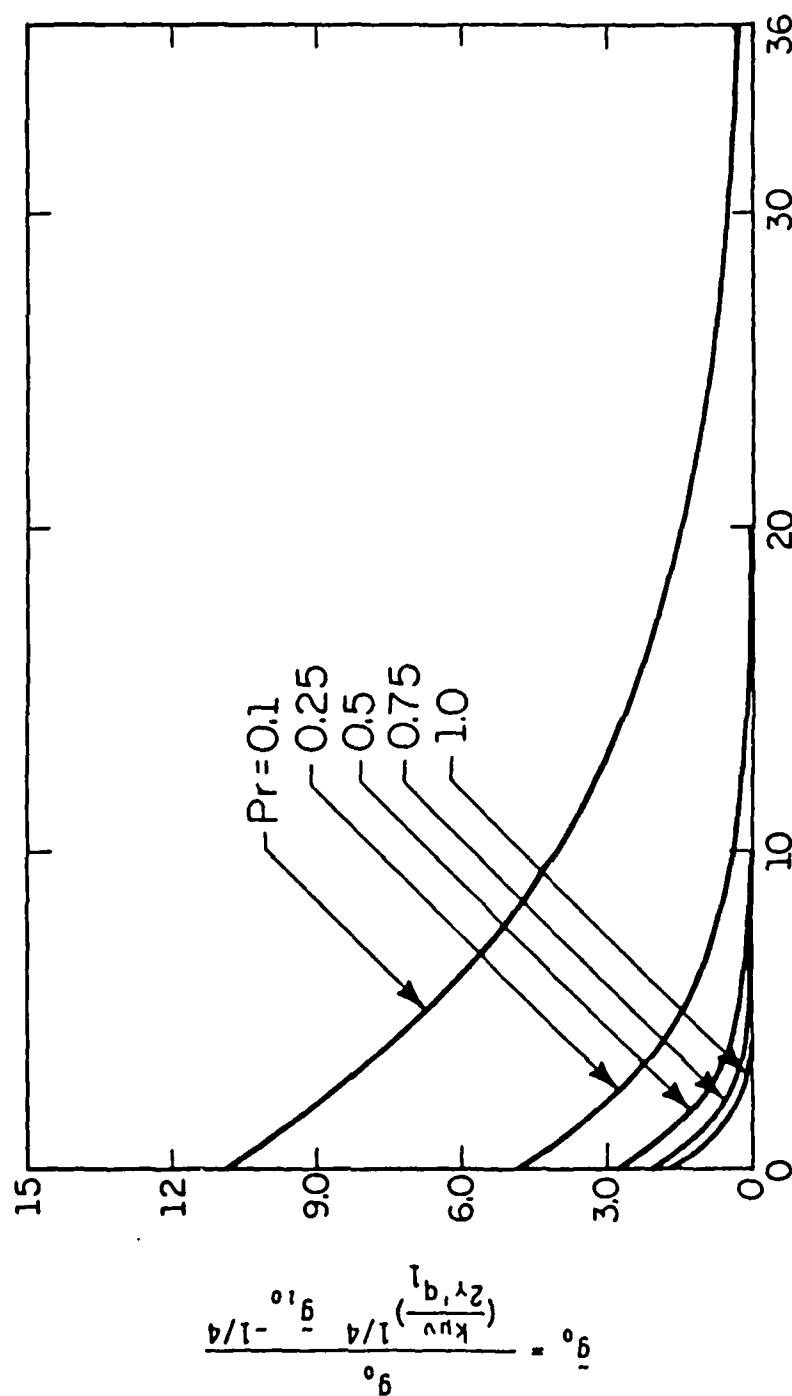


Figure 3.2.4 Graphs of \bar{g}_0 versus the Depth of the Two-Dimensional Case for Various Prandtl Numbers (< 1)

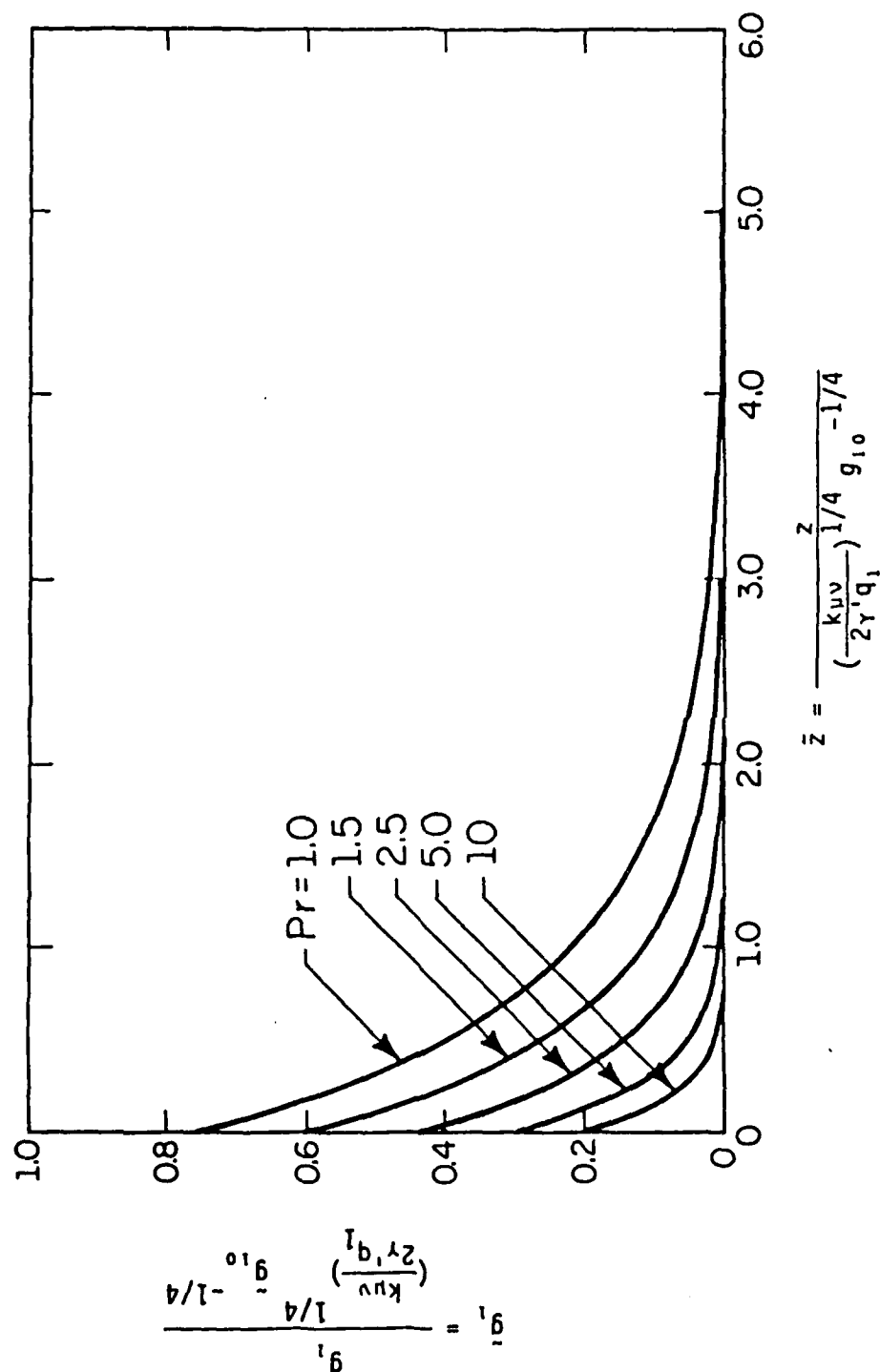


Figure 3.2.5 Graphs of \bar{g}_1 versus the Depth of the Two-Dimensional Case for Various Prandtl Numbers (> 1)

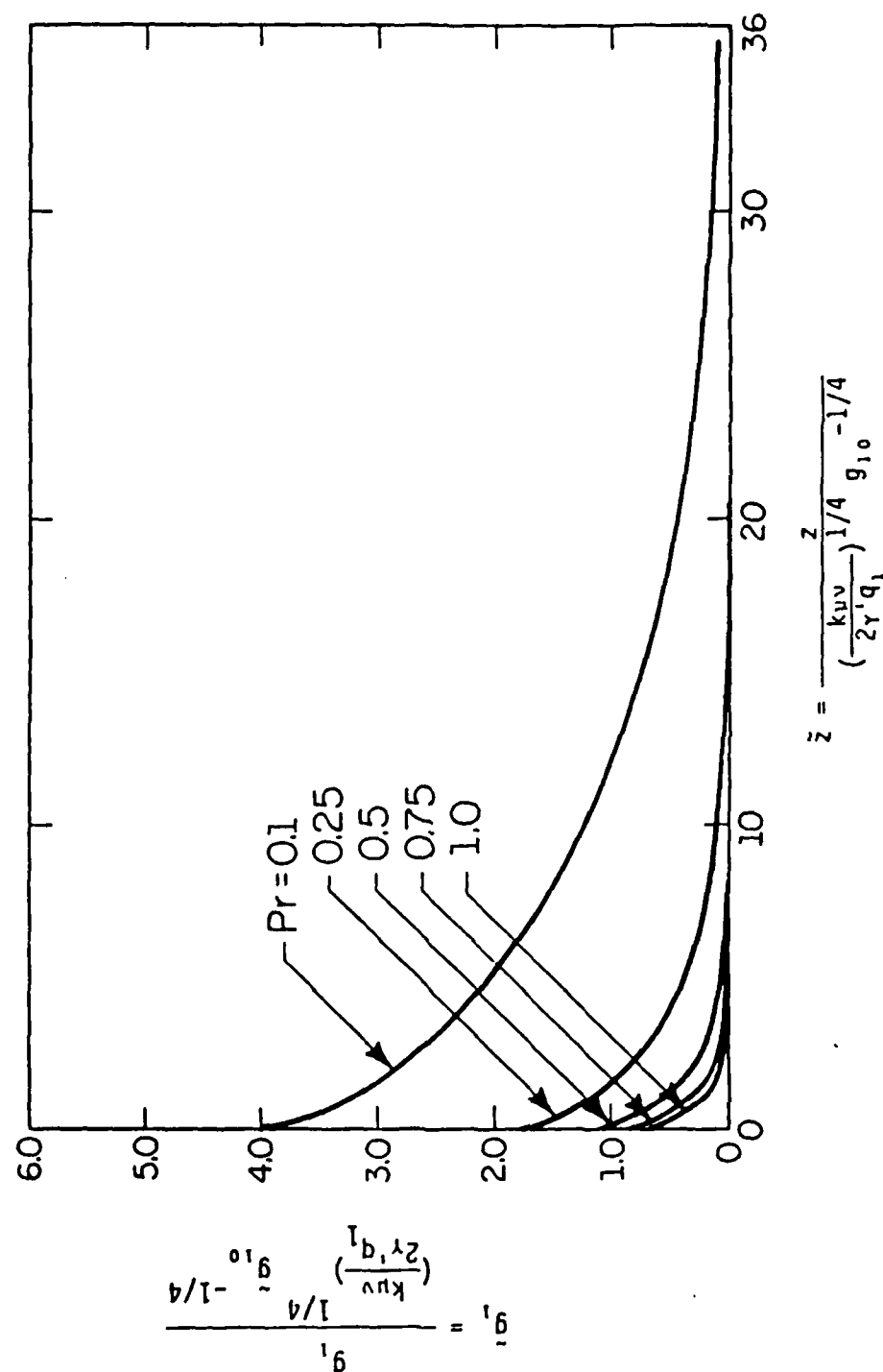


Figure 3.2.6 Graphs of \bar{g}_1 versus the Depth of the Two-Dimensional Case for Various Prandtl Numbers (< 1)

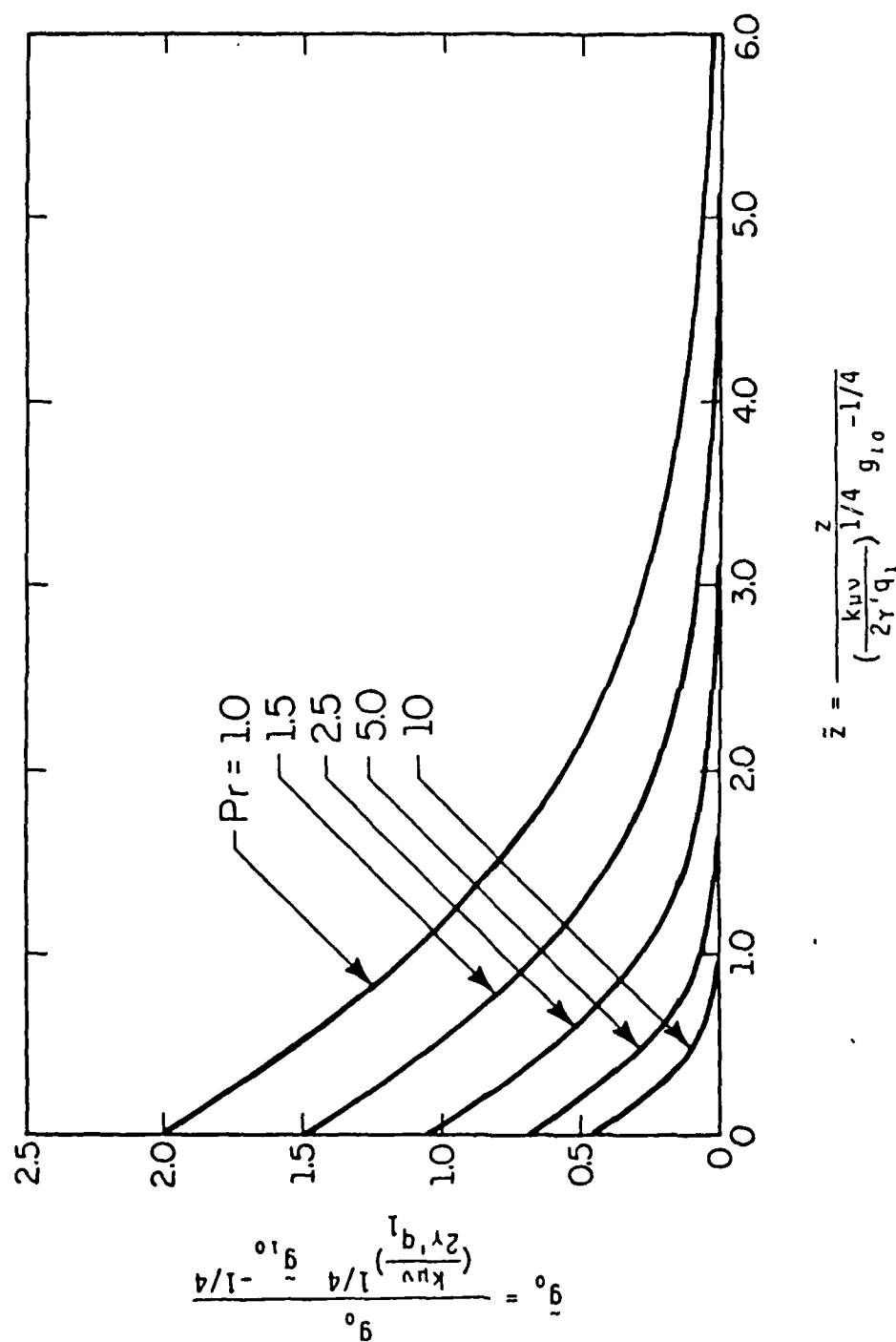


Figure 3.2.7 Graphs of \bar{g}_0 versus the Depth of the Axisymmetric Case for Various Prandtl Numbers (> 1)

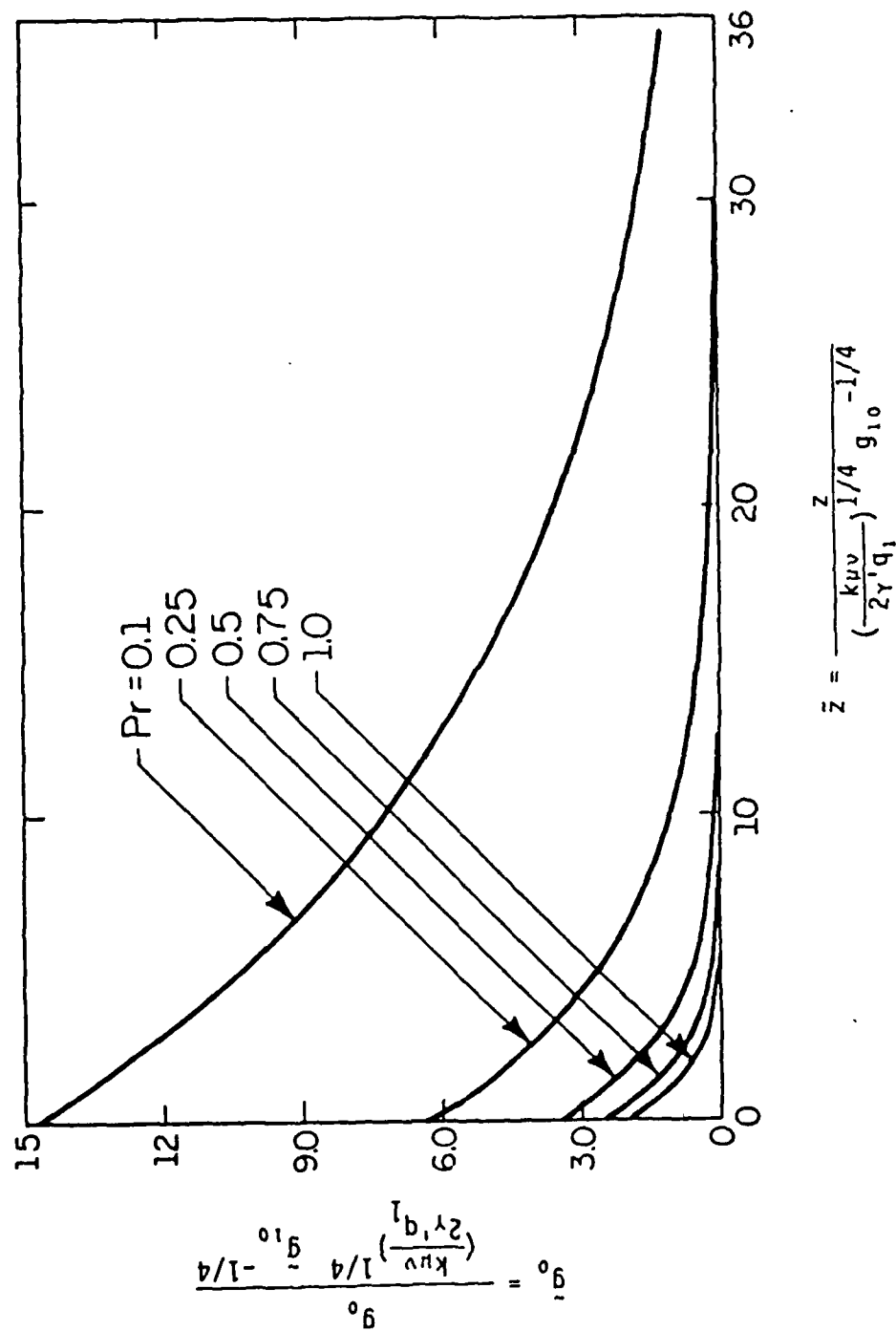


Figure 3.2.8 Graphs of \bar{g}_0 versus the Depth of the Axisymmetric Case for Various Prandtl Numbers (< 1)

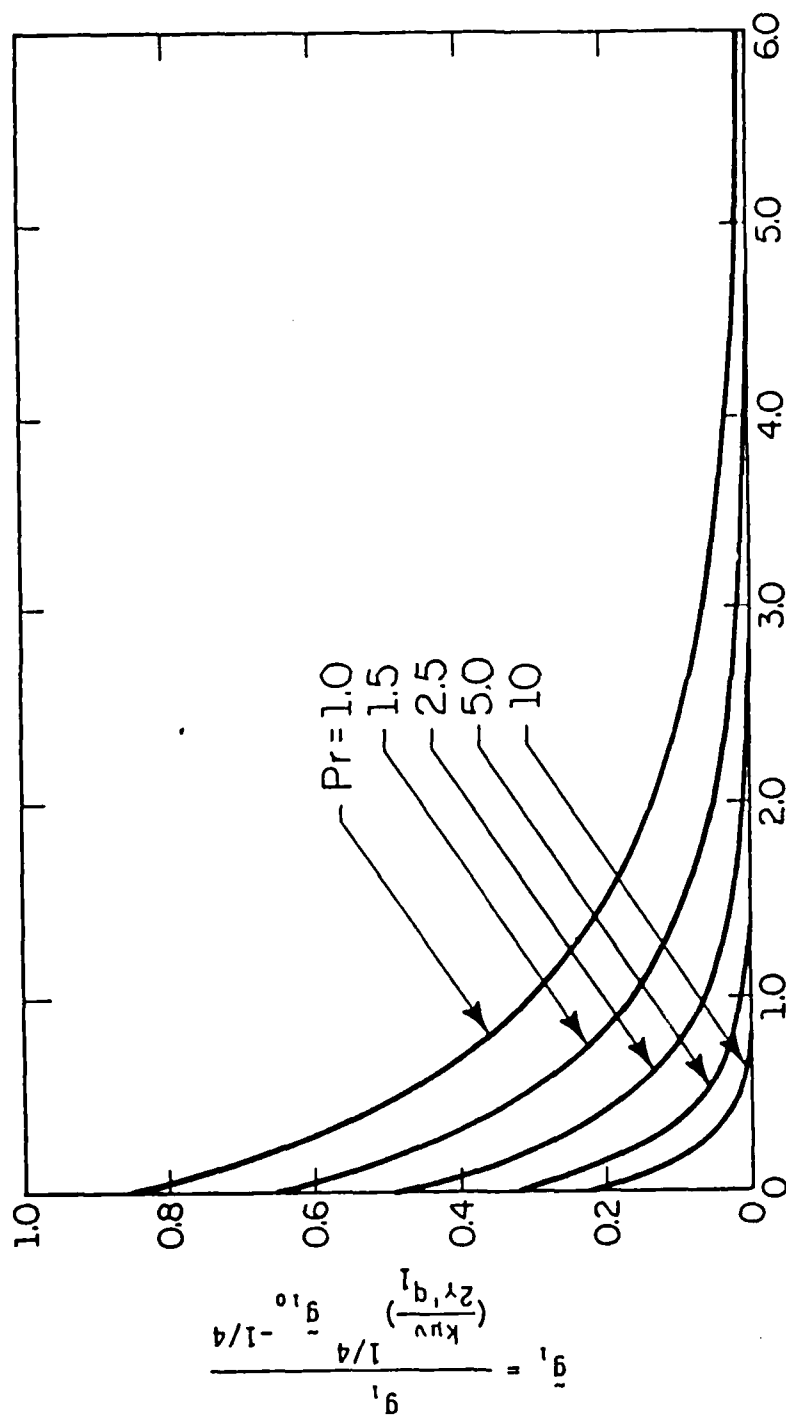


Figure 3.2.9 Graphs of \bar{g}_1 versus the Depth of the Axisymmetric Case for Various Prandtl Numbers (> 1)

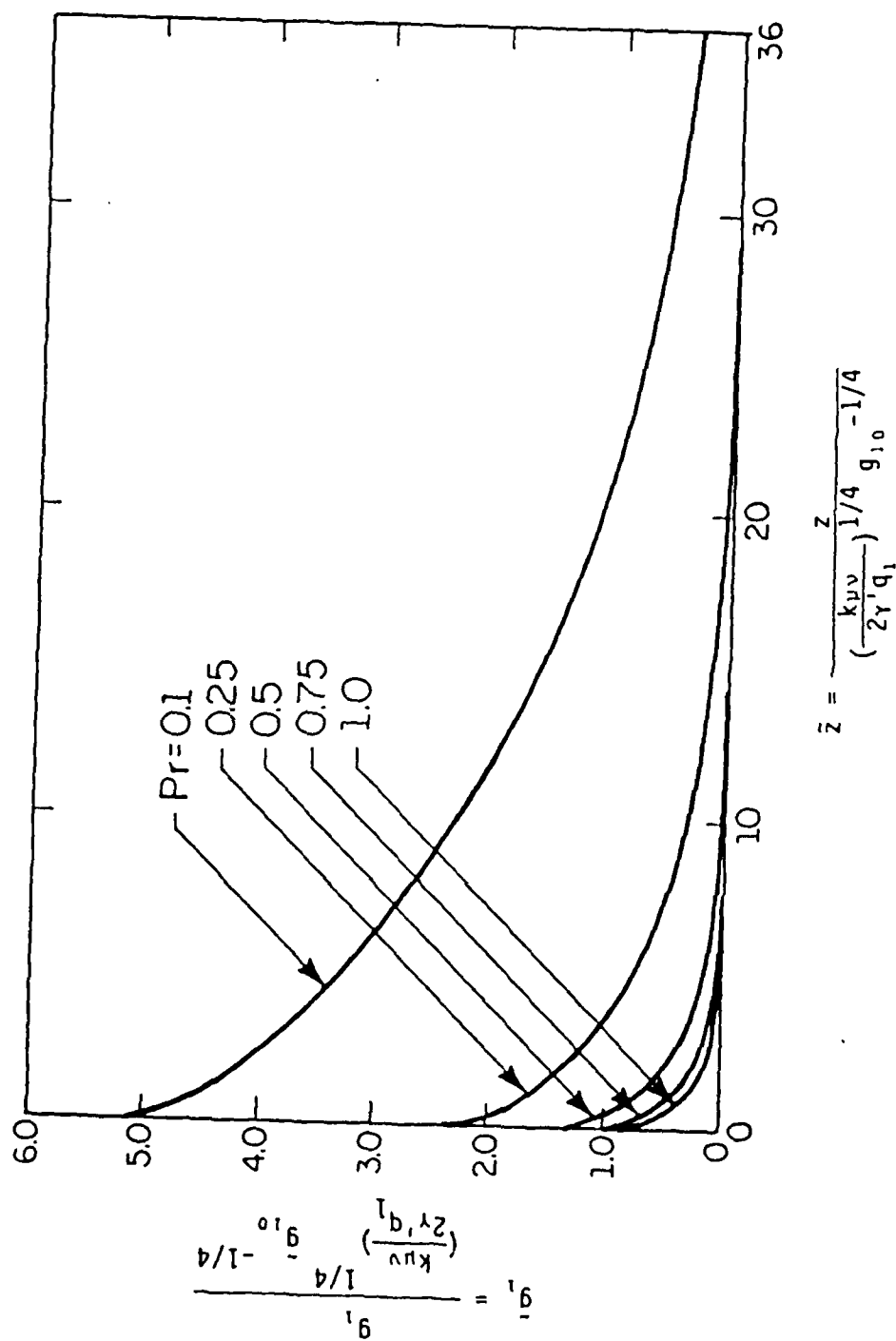


Figure 3.2.10 Graphs of g_1 versus the Depth of the Axisymmetric Case for Various Prandtl Numbers (< 1)

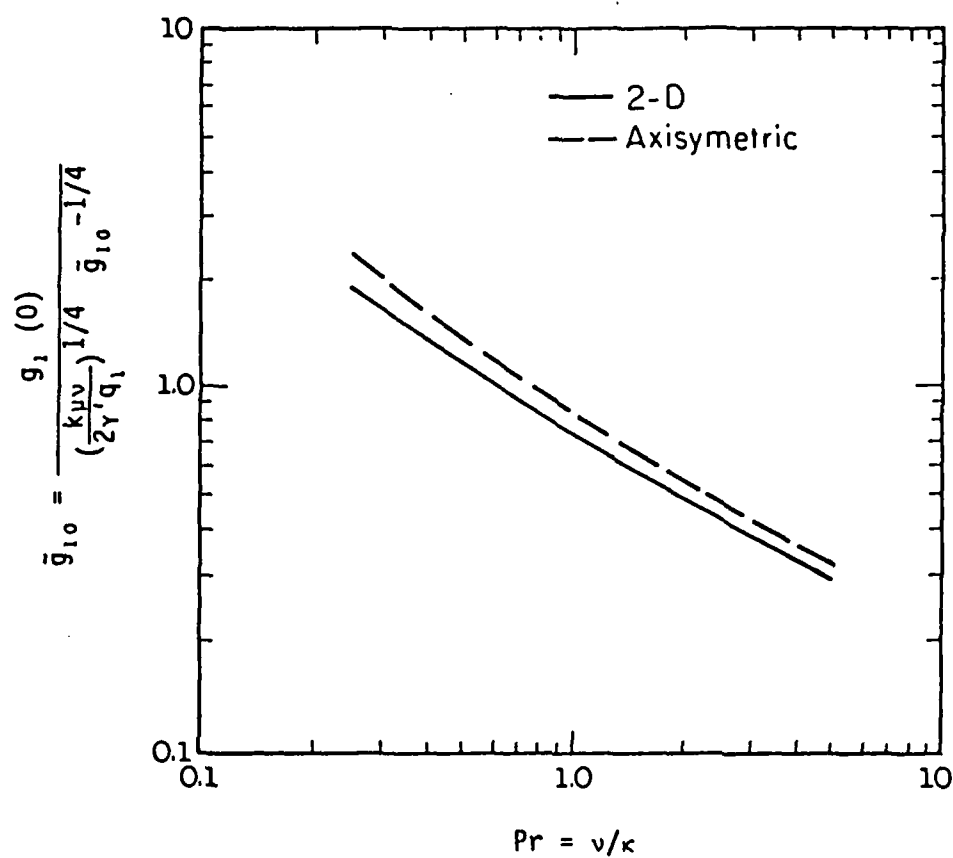


Figure 3.2.11 Second Coefficient (Second Derivative) of the Surface Temperature versus the Prandtl Numbers (Stagnation Flow Analysis)

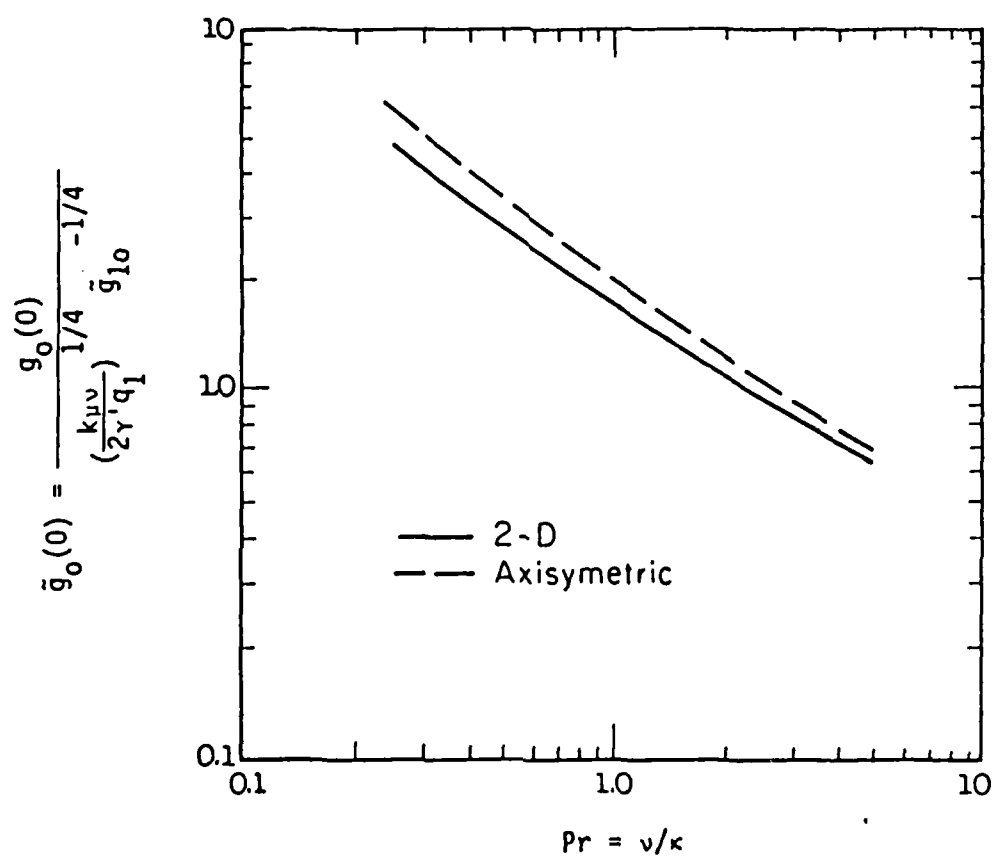


Figure 3.2.12 Maximum Temperature versus the Prandtl Numbers
(Stagnation Flow Analysis)

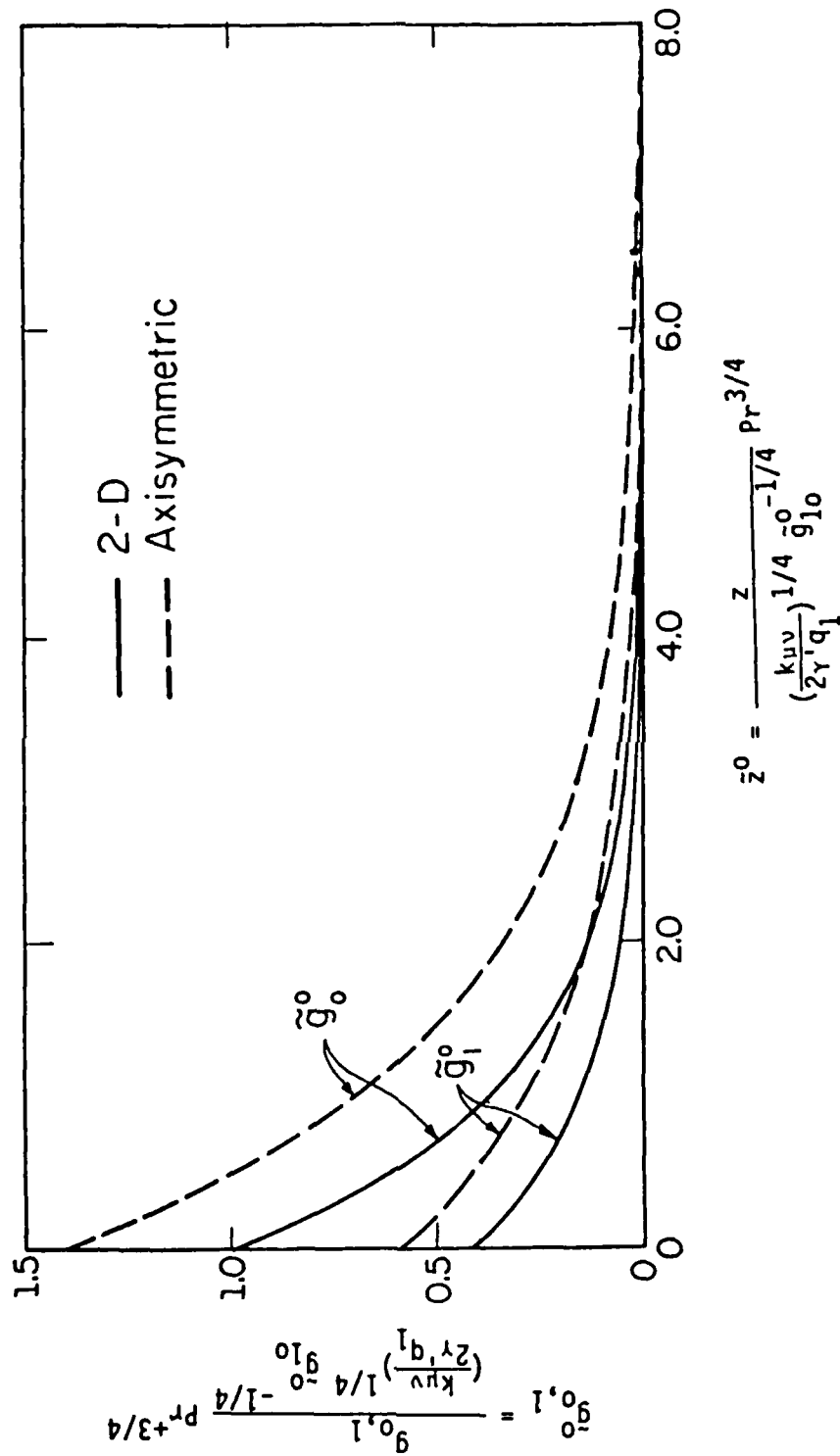


Figure 3.2.13 Dimensionless Temperature Functions $\bar{g}_0^0(\bar{z}^0)$ and $\bar{g}_1^0(\bar{z}^0)$ of the Limiting Case of Small Prandtl Number (Stagnation Flow Analysis)

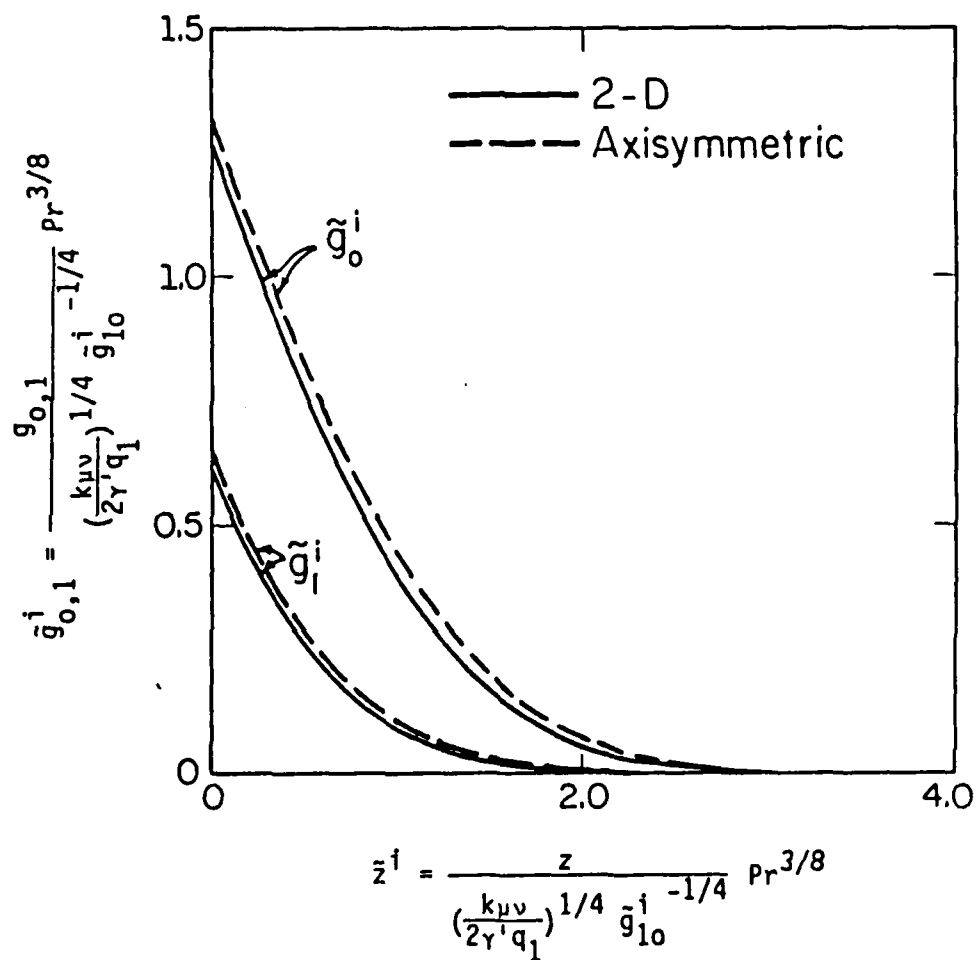


Figure 3.2.14 Dimensionless Temperature Functions $\bar{g}_0^i(\bar{z}^i)$ and $\bar{g}_1^i(\bar{z}^i)$ of the Limiting Case of Large Prandtl Number (Stagnation Flow Analysis)

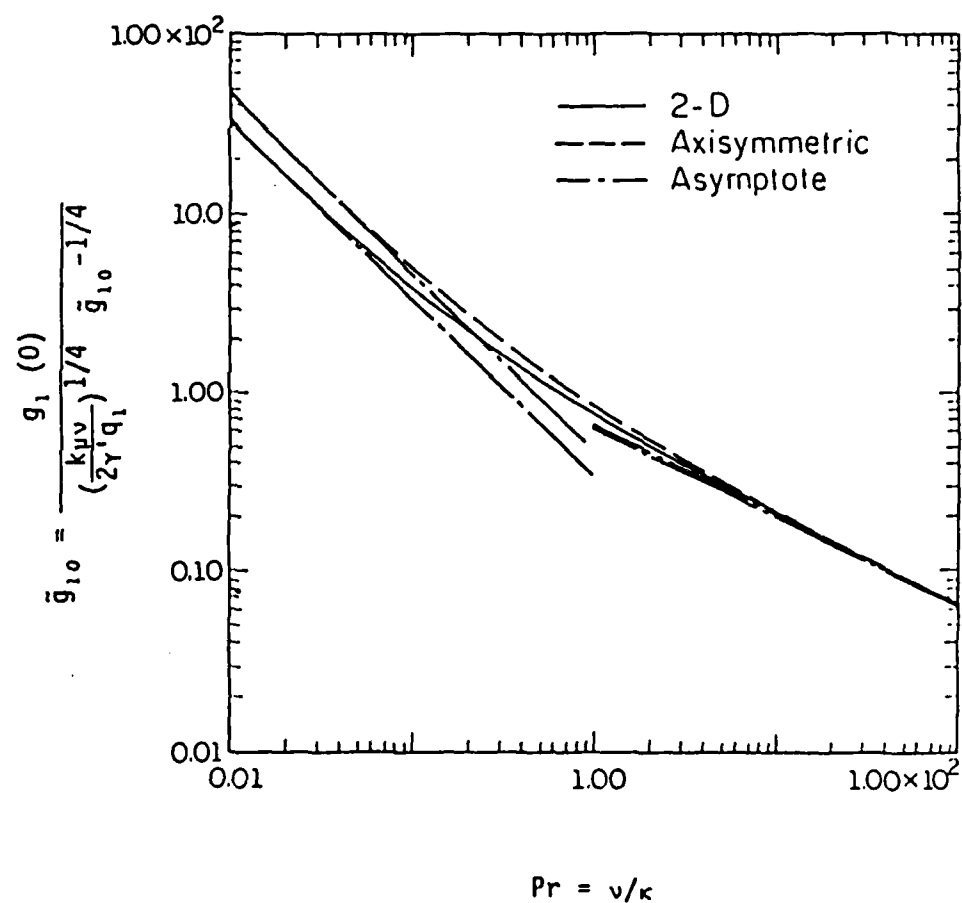


Figure 3.2.15 Second Coefficient (Second Derivative) of the Surface Temperature versus the Prandtl Numbers (Stagnation Flow Analysis)

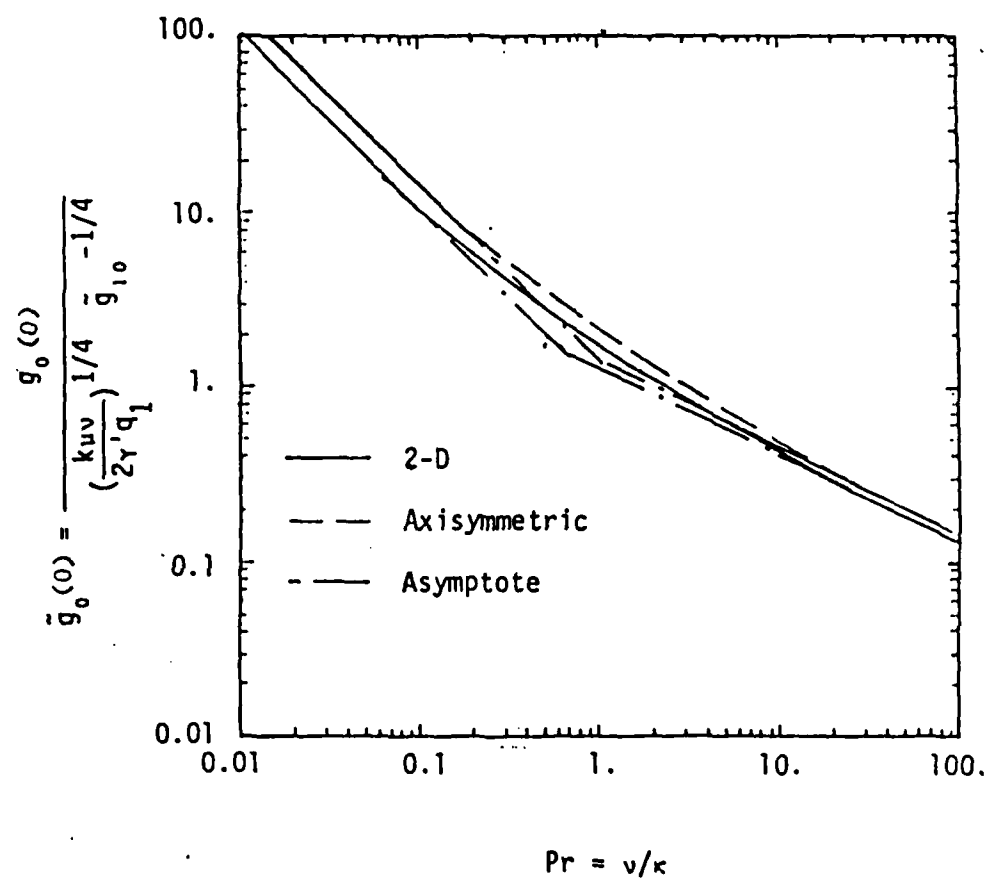


Figure 3.2.16 Maximum Temperature versus the Prandtl Number (Stagnation Flow Analysis)

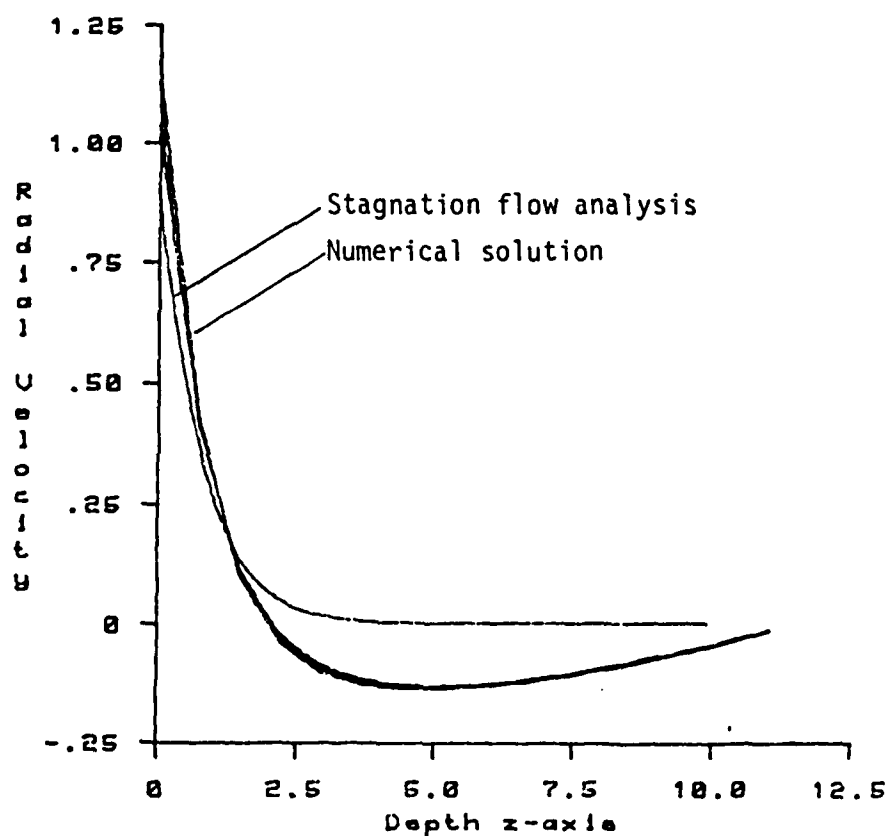


Figure 3.2.17 Comparison of the Universal Velocity Profile f' for the Stagnation Flow Analysis and the Numerical Solution Results $Ma = 1,500$, $Pr = 0.15$, $T_m^* = 0.25$, and $RF = 0.0$

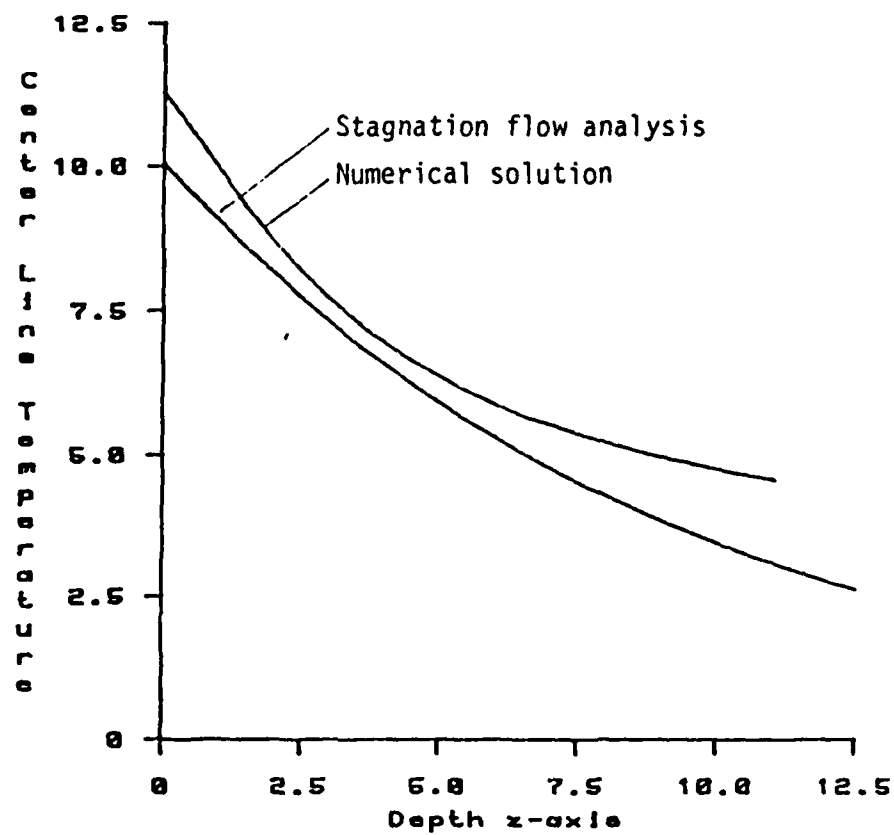


Figure 3.2.18 Comparison of the Centerline ($r = 0$) Temperature of the Stagnation Flow Analysis and the Numerical Solution Results $Ma = 1,500$, $Pr = 0.15$, $T_m^* = 0.25$, and $RF = 0.0$

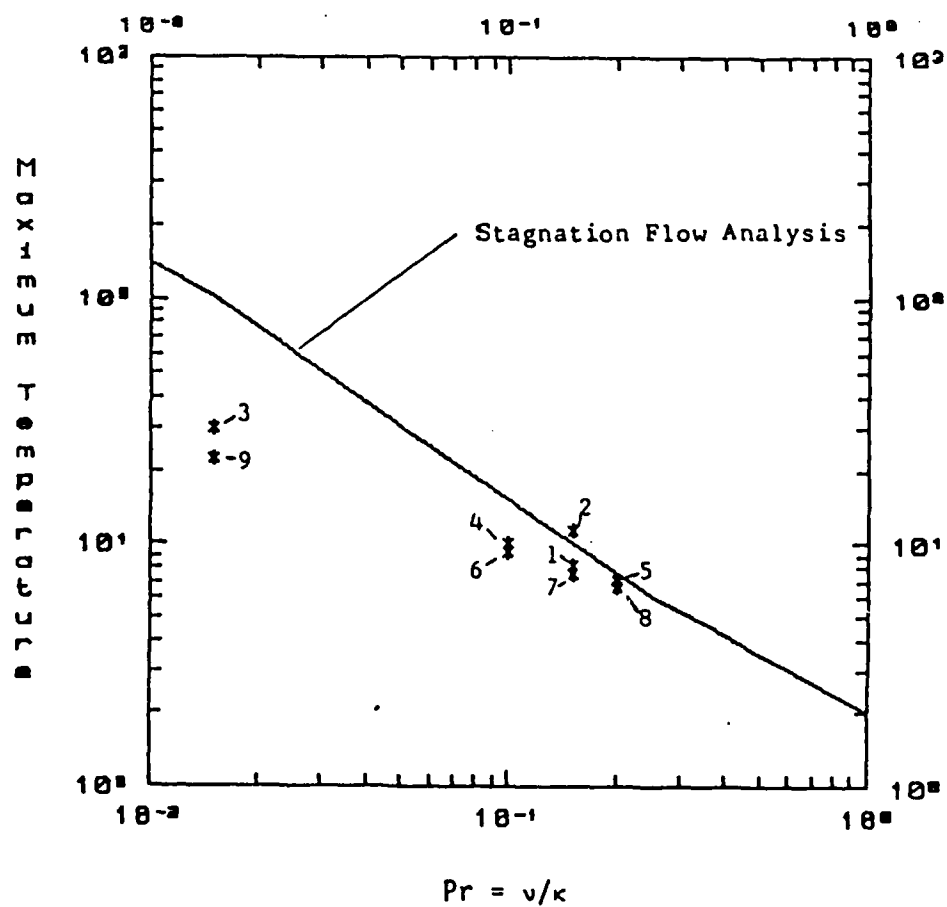


Figure 3.2.19 Comparison of the Maximum Temperature of the Stagnation Flow Analysis and the Numerical Solution Results. The Numerical Solution Results are Numbered According to Table 5.1

Table 3.2.1 Asymptotic Limits of the Stream Function at Small and Large \tilde{z}

	Functional Form	Plane 2-D	Axisymmetric
$\tilde{z} \rightarrow 0$	$\tilde{f}_1 = \tilde{f}'_{10} \tilde{z}$	$\tilde{f}'_{10} = 1.0$	$\tilde{f}'_{10} = 0.8987$
$\tilde{z} \rightarrow \infty$	$\tilde{f}_1 = \tilde{f}_\infty$	$\tilde{f}_\infty = 1.0$	$\tilde{f}_\infty = 0.7124$

Table 3.2.2 Asymptotic Limits of the Surface Temperature Coefficients

	Plane 2-D	Axisymmetric
$Pr \rightarrow 0$	$\tilde{g}_0^0(0) = 1.0$	$\tilde{g}_0^0(0) = 1.4037$
	$\tilde{g}_1^0(0) = 0.3333$	$\tilde{g}_1^0(0) = 0.4679$
$Pr \rightarrow \infty$	$\tilde{g}_0^1(0) = 1.2533$	$\tilde{g}_0^1(0) = 1.3946$
	$\tilde{g}_1^1(0) = 0.6266$	$\tilde{g}_1^1(0) = 0.6610$

3.3 Three Dimensional Numerical Model

3.3.1 Introduction

The majority of the previous work dealing with surface tension gradient driven flows was based on one-dimensional and two-dimensional assumptions. Because of the complex nature of the melt pool phenomenon, important physical characteristics may be unresolved by these oversimplified models.

The perturbation solution described earlier in this report offers an interim solution in that two two-dimensional solutions are used to construct three-dimensional solutions of modest scanning velocities. This chapter describes full three-dimensional numerical solutions. Our program is a three-dimensional finite difference scheme which iteratively evaluates the energy, momentum and continuity (pressure corrector) equations for transient/ steady-state cases. For programming simplicity as well as easy user understanding, a rectangular coordinate system was defined which uses in-line grid and primitive variable formulations. Assumptions made to simplify the problem are: 1) the material is homogeneous throughout, 2) all physical properties, with the exception of viscosity and surface tension, remain constant throughout both solid and liquid phases, 3) the material scanning speed remains constant, 4) the absorbed surface energy flux remains constant, 5) the top surface was initially flat and, 6) buoyancy, evaporation and latent heat effects were neglected.

3.3.2 Formulation

The basic governing equations in indicial notation are,

the continuity equation:

$$\frac{\partial u_i}{\partial x_i} = 0 \quad (3.3.1)$$

the momentum equation:

$$\frac{\partial u_i}{\partial t} + u_j \frac{\partial u_i}{\partial x_j} = - \frac{1}{\rho} \frac{\partial p}{\partial x_i} + \nu \frac{\partial^2 u_i}{\partial x_j \partial x_j} \quad (3.3.2)$$

the energy equations,

within the molten pool:

$$\rho c_p \left(\frac{\partial T}{\partial t} + u_i \frac{\partial T}{\partial x_i} \right) = k \frac{\partial^2 T}{\partial x_i \partial x_i} + \mu \frac{\partial u_i}{\partial x_j} \left(\frac{\partial u_j}{\partial x_i} + \frac{\partial u_i}{\partial x_j} \right) \quad (3.3.3)$$

in the solid region:

$$\rho c_p \left(\frac{\partial T}{\partial t} + u_s \frac{\partial T}{\partial x_1} \right) = k \frac{\partial^2 T}{\partial x_i \partial x_i} \quad (3.3.4)$$

where δ_{ij} is the Kronecker delta. The appropriate boundary conditions on the free surface are, i) the kinematic free surface condition, requiring the fluid particles at the surface remain attached, ii) the dynamic free surface condition, requiring the balance of both normal and tangential stresses, and iii) the heat flux condition. Mathematically, they would be formulated as,

$$x_3 = 0;$$

kinematic free surface condition,

$$u_3(x_1, x_2, \eta, t) = \frac{\partial \eta}{\partial t} + u_1 \frac{\partial \eta}{\partial x_1} + u_2 \frac{\partial \eta}{\partial x_2} \quad (3.3.5)$$

dynamic free surface condition,

normal stress balance,

$$\tau_{ij} n_i n_j + (p_0 - p) - \rho g \eta = -\gamma \left(\frac{1}{R_1} + \frac{1}{R_2} \right) \quad (3.3.6)$$

tangential stress balance,

$$\tau_{ij} n_j s_i = \frac{\partial \gamma}{\partial s} = \gamma' \cdot \nabla T \cdot \vec{s} \quad (3.3.7)$$

heat flux condition,

$$k \frac{\partial T}{\partial x_3} = \begin{cases} -q'' + \epsilon \sigma (T^4 - T_a^4), & x_1^2 + x_2^2 \leq r_0^2 \\ \epsilon \sigma (T^4 - T_a^4), & \text{otherwise} \end{cases} \quad (3.3.8)$$

The boundary conditions along the solid-liquid interface which is defined by the surface at melting temperature,

$$T = T_m \quad (3.3.9)$$

are the continuity of mass,

$$u_1 = u_s \frac{\rho_s}{\rho_l}, u_2 = u_3 = 0 \quad (3.3.10)$$

and the balance of heat fluxes and the latent heat of fusion.

$$\lambda \rho_s u_s \cdot \frac{\vec{n}}{|\vec{n}|} = k_s \frac{\partial T_s}{\partial n} - k_l \frac{\partial T_l}{\partial n} \quad (3.3.11)$$

It is important to point out that the surface which describes the solid-liquid interface is not known a priori. It is part of the problem to be solved.

The formulation is completed by specifying the boundary condition far away from the heat source to be unaffected by the heat source,

$$|x_1|, |x_2|, x_3 \rightarrow \infty;$$

$$T \rightarrow T_a \quad (3.3.12)$$

The calculation domain is illustrated in Figure 3.3.1. A right-handed rectangular coordinate system is imposed on an elongated slab, the origin of the coordinate system being located at the slab's lower, left, front corner. The concentrated heat source strikes the workpiece on the top surface, the center of the source being located at the slab mid-point in the Y direction and approximately one-third of the slab length in the X direction. The viewer and the heat source are located in a stationary reference frame while the workpiece scans into and out of the "control volume" calculation domain.

Because the material is assumed to be scanning in the positive X direction only, symmetry can be assumed about the slab mid-point in the Y direction. Due to this symmetry consideration, the actual calculation domain is reduced and is defined by the bold, solid rectangular box.

Figure 3.2.2 shows an X-Z cross-section of the calculation domain located at the symmetry plane in Y. The concentrated heat source is assumed to have a Gaussian energy distribution and is, again, applied at the top surface of the calculation domain. Phantom nodes were introduced to facilitate the imposition of desired boundary conditions. A Y-Z cross-section of the calculation domain located at $X = X$ (source center) is shown in Fig. 3.3.3. As seen, the Gaussian energy distribution is centered on the symmetry plane; the actual calculation domain being represented by the bold, solid box.

The details of the numerical scheme are described in the MS Thesis by R. Zehr [46]. It is essentially a point-iterative computation based on the finite difference formulation of the governing equations. In brief, at each iteration step, the residuals, representing errors, are computed for the three momentum equations, the continuity equation, and the energy equation. These residuals serve as indications for convergence, as well as the bases for computing convections for each of the velocities, pressure, and temperature. The convections for velocities and temperature are based on a mixed Gauss-Seidel and Jacobi schemes, proceeding from line-to-line according to the Gauss-Seidel scheme, updating values as each line is completed. With each line, however, the point-by-point iteration is based on the Jacobi scheme without updating the values. This is done to take advantage of the vectorizability of the Jacobi scheme. Pressure corrections are based on the artificial compressibility concept of Chorin [43], using a form for implicit problems derived by Mech [44].

For the calculations involving free surface deformation, the pressure distribution from flow calculations and that from the surface curvature are compared and iterated until they match. For these and other details, consult the thesis by Zehr [46].

3.3.3 Numerical Results

a. Introduction: Numerical solutions were obtained for six test cases in which steel was used as the scanning substrate. The governing parameters are listed in Table 3.3.1. Table 3.3.2 shows the various test case powers and scanning speeds which range from 200 W to 400 W, and 0.01 m/s to 0.024 m/s, respectively. Selected numerical information for test cases I, II, and V are graphically presented, corresponding to Power = 200 W, $U_s = 0.010$ m/s; Power = 240 W, $U_s = 0.012$ m/s; and Power = 400 W, $U_s = 0.02$ m/s, respectively. It should be noted that the beam center (at the domain surface) is defined as ($X = 0$, $Y = 0$, $Z = 0$) for graphing purposes.

b. Temperature Distributions: Figures 3.3.4 through 3.3.12 illustrate temperature isotherms (contours) from various cross-sections (viewpoints) of the domain. The three cross-sectional views are, 1) X-Z plane with Y located at the symmetry plane, 2) Y-Z plane with X located at the beam center, and 3) X-Y plane with Z located at the material surface. As seen, the temperature isotherms compress near the top solid/liquid interface due to the rapid impingement of fluid (convecting heat) against the solid substrate. These isotherms are compressed slightly more at the leading edge of the melt pool as compared to the trailing edge due to the scanning velocity of the substrate. The gap separating the isotherms widens near the bottom of the melt pool

indicating slower (convective) velocities in this region. Figures 3.3.6 and 3.3.10 illustrate the circular nature of the isotherms near the (beam) center which transform into ellipses due to the influence of the substrate scanning speed near the solid/liquid interface. This axisymmetric temperature distribution near the pool center supports the perturbation approach taken by Chan. [42] Figures 3.3.7 and 3.3.11 represent three-dimensional surface temperature contours which vividly illustrate the severe temperature gradients beneath the beam and at the solid/liquid interface. An interesting feature is the difference between the upstream and downstream dimensions of the pool. The relative downstream velocities are greater than the relative upstream velocities causing the melt pool front and sides ($-X$ and $\pm Y$, respectively) to flatten. More heat is convected downstream which lengthens (and deepens) the melt pool trailing edge. (See Figures 3.3.4, 3.3.6, 3.3.8, 3.3.9, 3.3.10, and 3.3.12.)

c. Velocity Fields: The recirculating velocity fields for the respective cross-sections are shown in Figures 3.3.13 through 3.3.17. Fluid is driven radially outward along the surface from the beam center until it reaches the solid/liquid interface. At this point the flow is turned downward, circulating along the pool bottom until reaching the center where it is forced upwards toward the surface. This recirculating pattern resembles a toroidal vortex. The large radial surface velocities are a direct consequence of the dramatic surface temperature gradients shown in Figures 3.3.7 and 3.3.11. Numerical results indicate that thermocapillary (surface) velocities are approximately two orders of magnitude larger than the substrate scanning velocity which illustrates the importance of surface tension effects. Governing dimensionless parameters and corresponding boundary layer thickness

estimates are listed in Table 3.3.3. Reynolds and Peclet numbers are based on the calculated pool length (in X) and the maximum surface velocity (U) for each test case. As the test case power and scanning speed increased the pool length and maximum surface velocity also increased. This increase caused the Reynolds and Peclet numbers to increase which caused the viscous and thermal boundary layers to grow thinner.

d. Cooling Rates: To illustrate heating and cooling of the substrate as it passes beneath the laser, temperature versus scanning distance(X) is plotted. Figures 3.3.19 and 3.3.20 show surface temperature versus distance(X) for various locations(Y) from the symmetry plane while Figures 3.3.19 and 3.3.21 illustrate symmetry plane temperatures versus distance(X) for various locations(Z) from the domain surface. The substrate is observed to increase in temperature as it approaches the laser and decrease in temperature after passing beneath the laser. The resolidified substrate microstructure is controlled by the magnitude of the cooling rate at any given location; the greater the cooling rate the finer the microstructure. (The cooling rate is directly proportional to the temperature gradient.) As illustrated, the most severe temperature gradients are located at the (symmetry plane) surface solid/liquid interface, becoming less severe at the melt pool side edges and bottom. These results suggest that the resolidified substrate microstructure is finest at the symmetry plane surface and coarser at the side/bottom edges. This is contradictory to experimental observation, however, where the finest microstructure is found at the pool side edges. Further study is needed to explain this discrepancy between theoretical and experimental results.

e. Free Surface Deformation: The first method involves solving the free surface subroutine in conjunction with the main iteration scheme. By continuously updating the free surface W velocities (and consequently the pressures) deformation of the surface occurred. A higher surface tension value (see Table 3.3.1, σ_{test}) was used in order to inhibit the free surface deformation from jumping over the phantom nodes. This method proved to be extremely slow due to the convergence requirements of the surface subroutine. A much quicker method used to visualize the surface deformation resembles a perturbation scheme. The converged (flat surface) pressure data was used as initial conditions for an independent surface subroutine calculation. The new surface values were iterated using a Poisson pressure formulation until conservation of mass was achieved about the initial surface position. Instead of recalculating the free surface W velocities and continuing the main iteration, the surface values were simply plotted, as illustrated in Figure 3.3.22. The two methods yield approximately similar results due to the small deformation of the surface. Method 2 is more efficient but applies to small surface deformations only. It should be noted that the "constant volume" convergence criterion was used at the melt pool surface because exact conditions are not presently known.

Both methods show the following trends. Thermocapillarity drives the surface fluid radially outward at extremely high velocities. These high velocities displace more mass from the central (surface) region than can be replaced by the recirculating flow, thus causing a depression. The displaced mass builds up at the solid/liquid interface causing the surface to bulge upward where it is then forced downward into the molten pool. The contact

angle of the liquid metal on the substrate at the solid/liquid interface is unknown and currently being researched. Dussan [45] indicates that the physics of contact angle are very poorly understood at the present time.

f. Variable Viscosity: It is well documented that some material properties, such as density, remain relatively constant while others such as surface tension and viscosity, vary considerably with temperature. Variable viscosity results compared with constant property results is presented in Tables 3.34 through 3.36 for test case I, Power = 200 W, $U_s = 0.010$ m/s which is illustrated in Figs. 3.3.23 through 3.3.26. (The o subscript denotes the beam location and * denotes the variable viscosity data.) Temperature and velocity profiles for the variable viscosity case were not plotted due to the relatively small changes in the velocities and pool shapes as compared to the constant property case.

An exponential curve fit was used to model the viscosity change with temperature in the melt pool region. The variation of viscosity with temperature is illustrated in Fig. 3.3.27. Local viscosity varied from 0.0055 kg/m-s at the melt temperature to approximately 0.0015 kg/m-s near the concentrated heat source. Local velocities were shown to increase with decreasing viscosity (increasing temperature), the most dramatic changes taking place near the free surface where heat is being convected radially outward from the concentrated heat source. These velocity changes were minor however, approximate 2-3 percent on the average. The velocity changes were smaller in the deeper regions of the melt pool.

g. Electromagnetic Forces: When a current is passed thru the scanning substrate by means of an arc, a current density (\bar{J}) is developed in the medium. This current also induces a magnetic field (\bar{B}) in the substrate which interacts with the \bar{J} field to form electromagnetic forces. The magnitude of the forces is determined by the cross-product of the \bar{J} and \bar{B} terms ($\bar{J} \times \bar{B}$). To illustrate the effects of the $J \times B$ forces the thermocapillary influence (for case I) was removed and a current of 300 Amps was implemented as the driving mechanism of the flow. As seen from Figs. 3.3.28 through 3.3.31 the $\bar{J} \times \bar{B}$ forces drive the flow radially inward and downward at the free surface. This downward flow impinges upon the pool bottom and recirculates upward along the solid/liquid interface, this recirculating pattern being exactly opposite to that of the thermocapillary recirculation pattern.

The $\bar{J} \times \bar{B}$ forces were also evaluated along with the surface tension driven forces for case I. A current of 100 Amps was used. (See Tables 3.37 through 3.38). (Once again, the o subscript denotes the concentrated heat source center and the $*$ denotes the variation from the constant property case, or in other words, the $\bar{J} \times \bar{B}$ plus surface tension data.) Results show that the radially driven surface velocities were decreased by approximately 10 percent on the average due to the $\bar{J} \times \bar{B}$ influence. This retardation of the flow tends to shrink the pool (radially) and deepen the melt pool bottom. For large enough currents this inward $\bar{J} \times \bar{B}$ flow will predominate over the outward surface tension flow and become the driving mechanism in the melt pool.

3.3.4 Conclusions

From the numerical solutions the following trends can be observed. Application of a laser onto a scanning substrate forms a melt pool which has a

characteristic length-to-width aspect ratio of approximately 1 and a characteristic length-to-depth aspect ratio of approximately 7-12. The melt pool isotherms are approximately circular in the (X-Y) region of the beam center and elongate into elliptic shapes away from the beam. The elliptic form is due to the influence of the substrate scanning velocity on the recirculating flow field. The isotherms tend to compress near the solid/liquid interface due to the impinging flow while the spacing of the isotherms widens near the pool bottom due to the reduced velocities. A dimple forms at the melt pool bottom due to the recirculating nature of the flow. The flow is driven by surface tension effects which is termed thermocapillary flow due to the influence of temperature on surface tension. The thermocapillary velocities are approximately two orders of magnitude greater the substrate scanning velocity which signifies the importance of surface tension. These thermocapillary velocities (on the order of 1 m/s) are a direct consequence of the severe temperature gradients imposed on the substrate by the laser. These temperature gradients are directly proportional to the cooling rates surrounding the melt pool which influences the microstructure of the resolidified substrate. Preliminary free surface calculations show the development of a depressed region in the melt pool center causing mass to bulge upward at the solid/liquid interface before being recirculated downward into the melt pool. Local velocities were seen to increase with decreasing viscosity. The changes were small, however, approximately 2-3 percent on the average. $\vec{J} \times \vec{B}$ forces induced by current from an arc tend to recirculate the flow opposite to that of the surface tension flow, and may predominate if the current is large enough.

These results give important insights into the physical phenomenon involved in laser, arc and electron beam welding/alloying of metals. Further investigation of this subject would provide information on controlling the microstructure of the weld heat-affected-zone (HAZ) by specifying laser parameters as well as yielding further physical insights such as contact angle and oxidation effects.

Suggestions for program improvement include: 1) the incorporation of a variable grid scheme for finer resolution inside the melt pool boundary layers and a coarser resolution in the moving substrate temperature solution domain, 2) the incorporation of an acceleration scheme for quicker residual convergence, 3) the advancement of the free surface routine which would include steep surface curvature and multiple node jumping capabilities and, 4) melt pool coordinate transformation for easier computational analysis in conjunction with a cylindrical coordinate system.

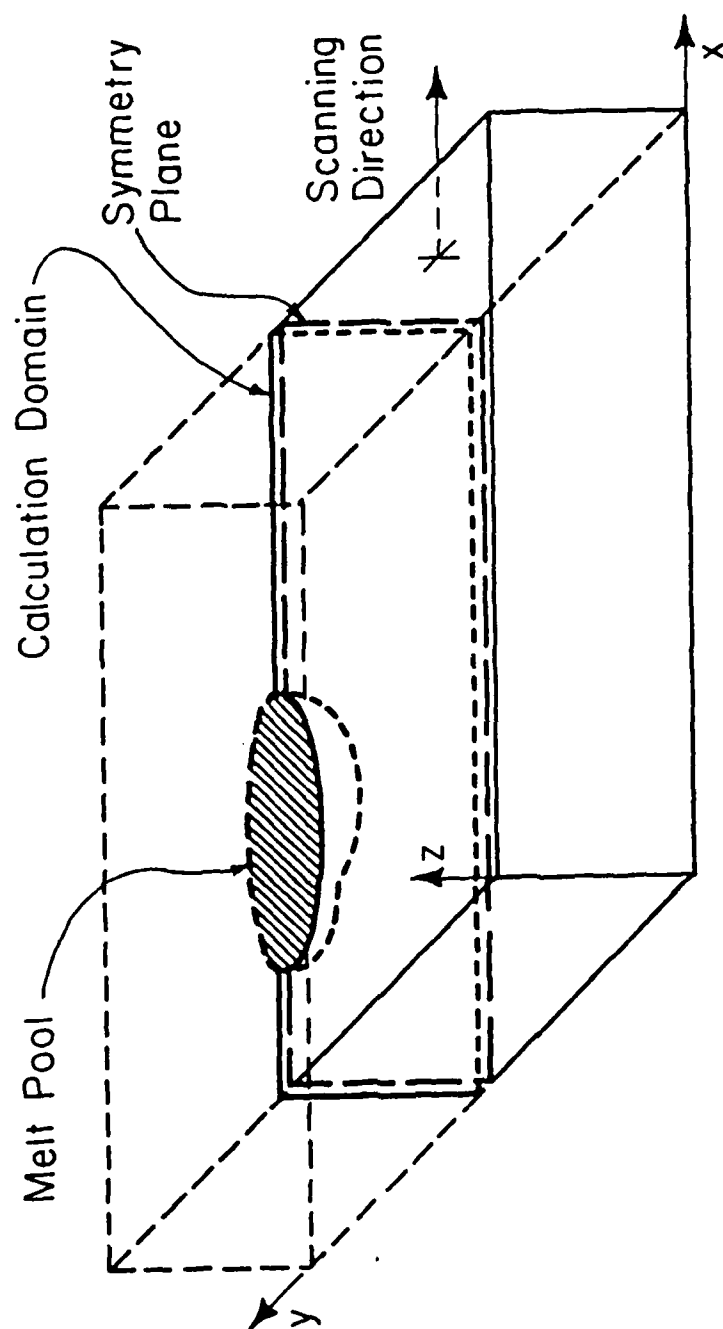


Figure 3.3.1 Three-Dimensional Calculation Domain

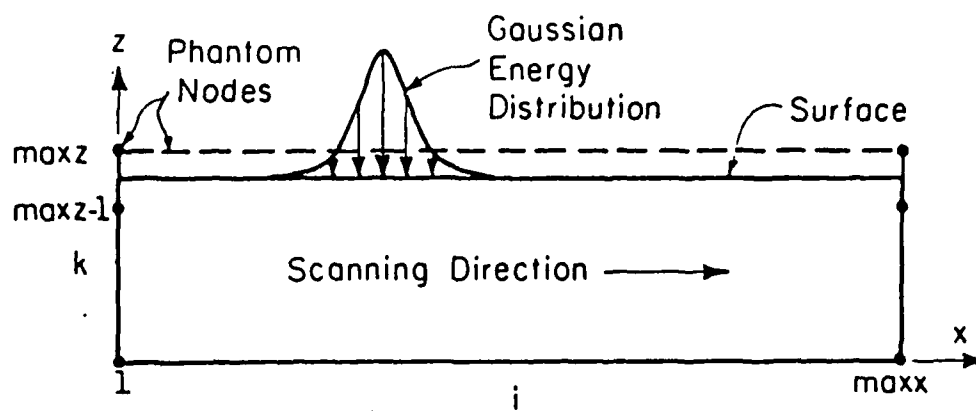


Figure 3.3.2 X-Z Plane Cross-Section of the Calculation Domain
(Y Located at the Symmetry Plane)

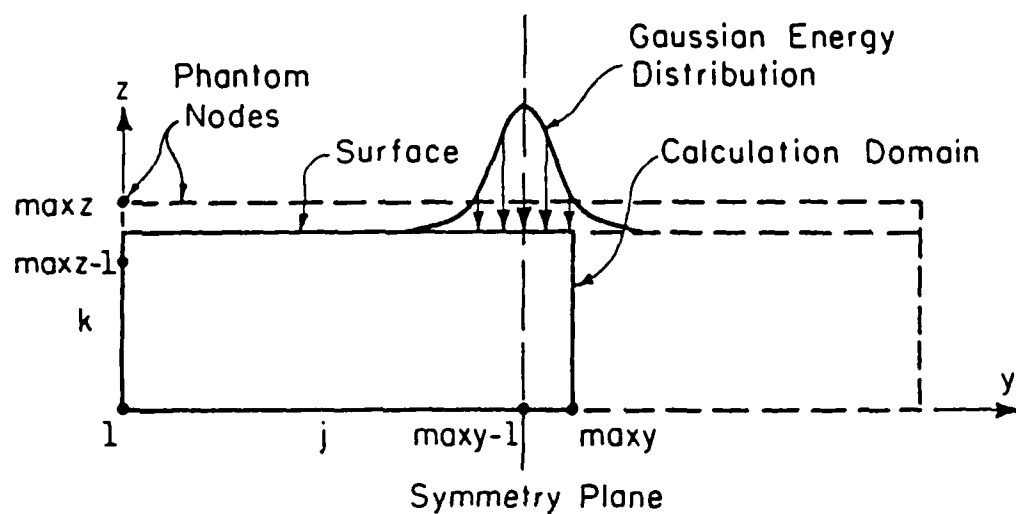
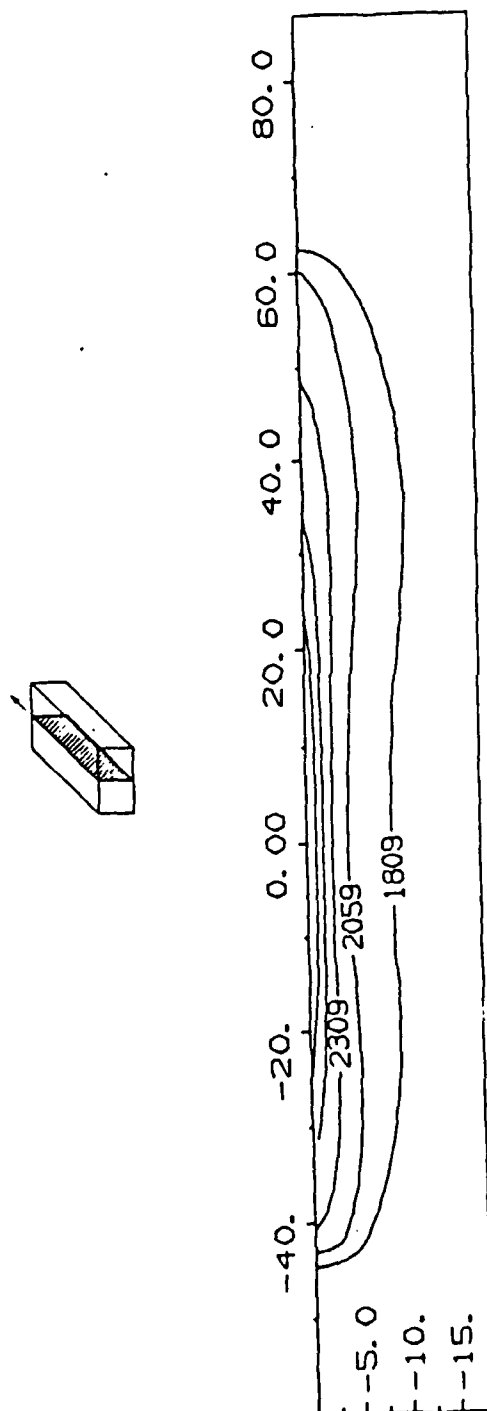
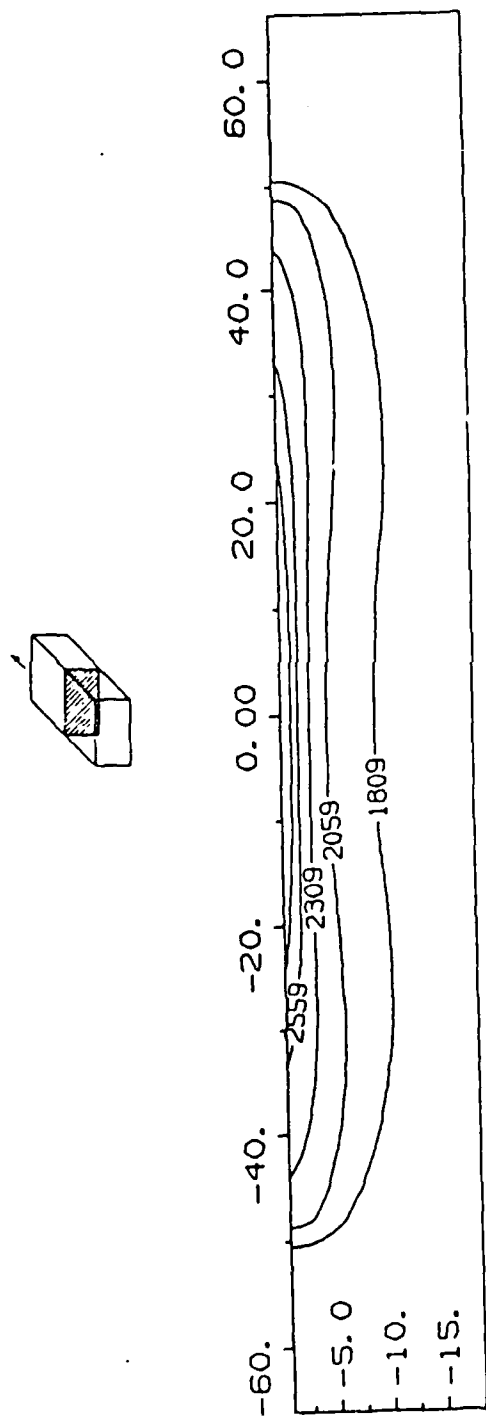


Figure 3.3.3 Y-Z Plane Cross-Section of the Calculation Domain
(X Located at the Beam Center)



Meters *(E-05)

Figure 3.3.4 Melt Pool Isotherms in the X-Z Plane
with Y Located at the Symmetry Plane
(Power = 240 W, $U_s = 0.012$ m/s)



Meters *(E-05)

Figure 3.3.5 Melt Pool Isotherms in the Y-Z Plane
with X Located at the Beam Center
(Power = 240 W, $U_s = 0.012$ m/s)

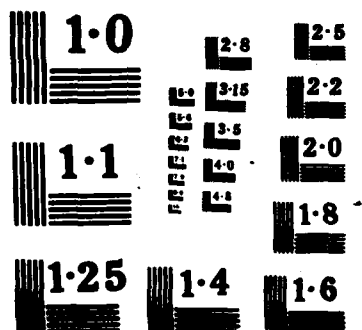
EFFECT OF CONVECTION ON WELD POOL SHAPE AND
MICROSTRUCTURE(U) ILLINOIS UNIV AT URBANA DEPT OF
MECHANICAL AND INDUSTRIAL ENGINEERING
J MAZUMDER ET AL. JUL 86 N00014-84-K-0315 F/G 1

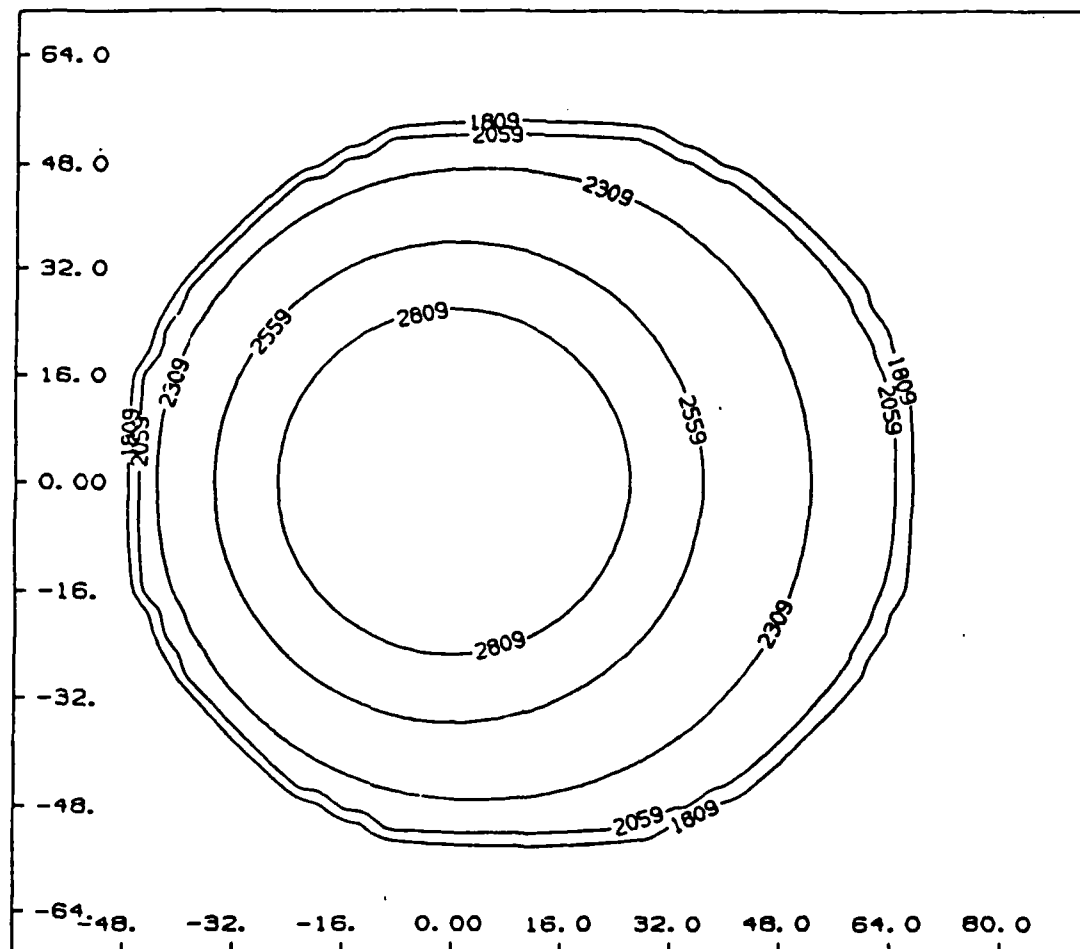
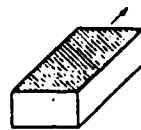
UNCLASSIFIED

F/G 11/6

NE

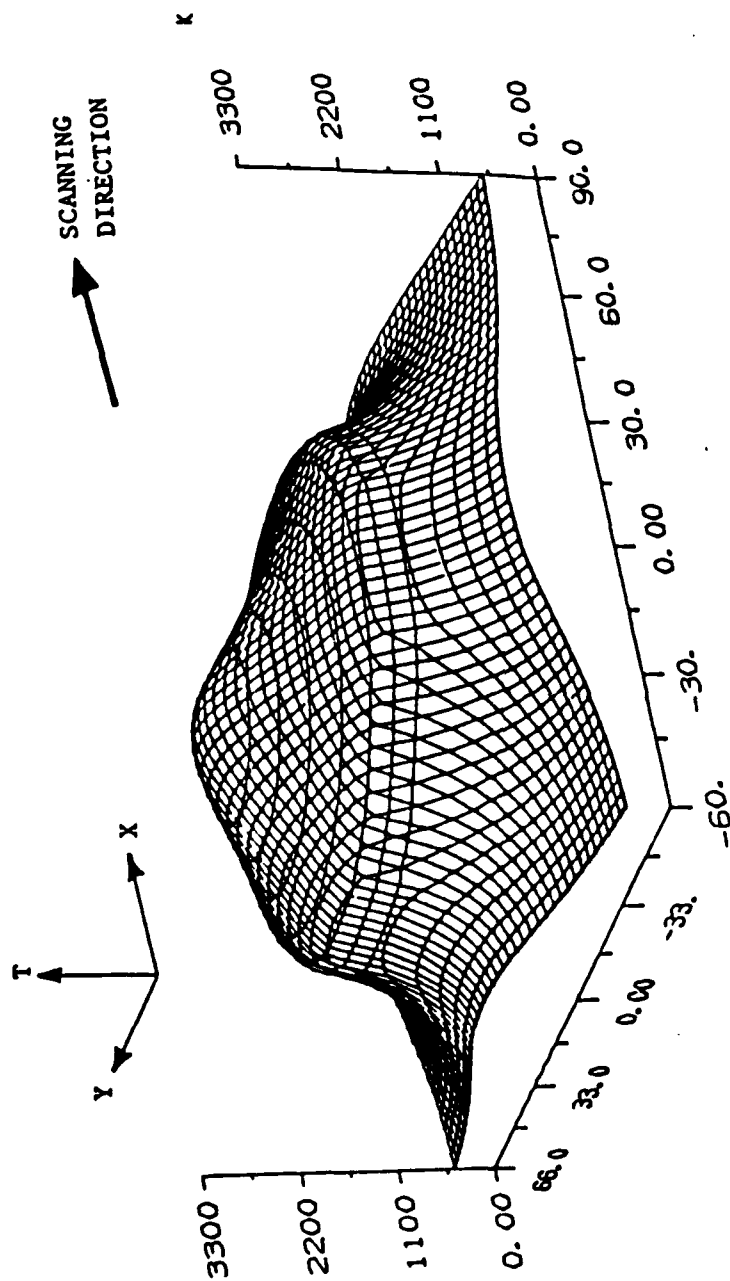
[illegible]





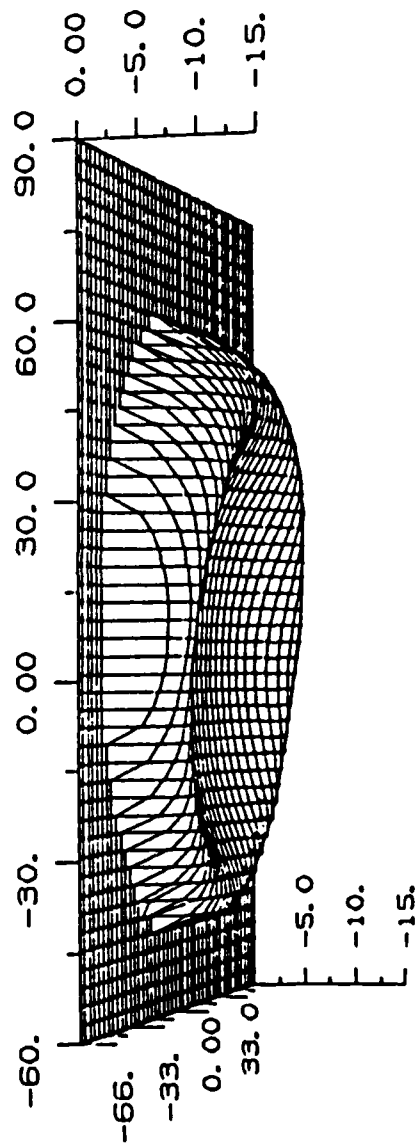
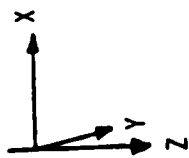
Meters $\times (E-05)$

Figure 3.3.6 Melt Pool Isotherms in the X-Y Plane
with Z Located at the Material Surface
(Power = 240 W, $U_s = 0.012$ m/s)



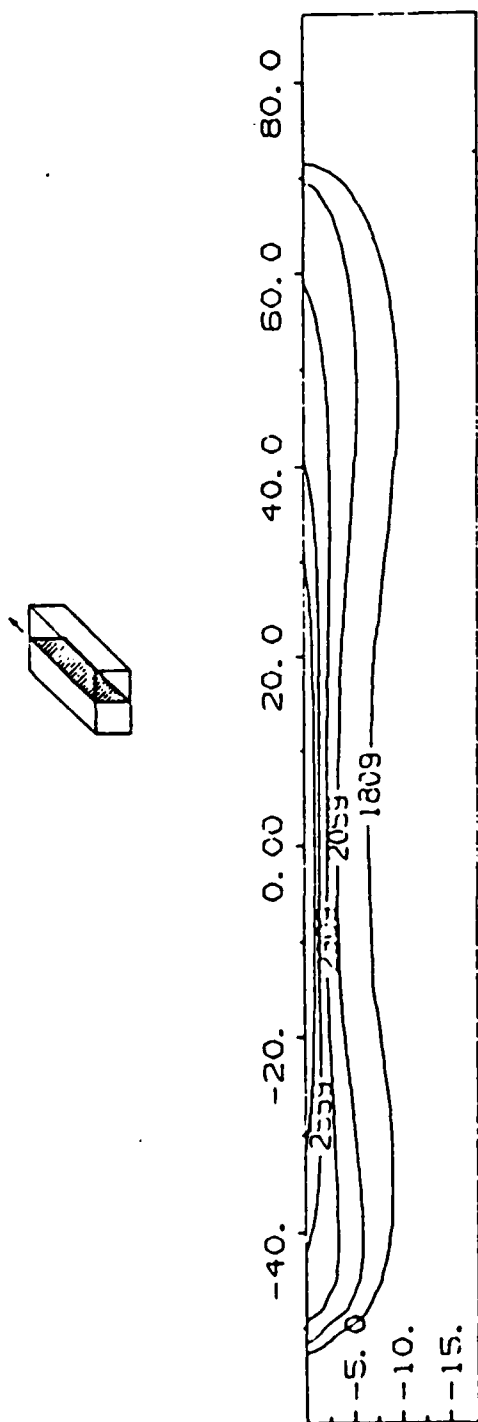
Meters $\times 10^{-5}$

Figure 3.3.7 Surface Temperature Contours
(Power = 240 W, $U_s = 0.012$ m/s)



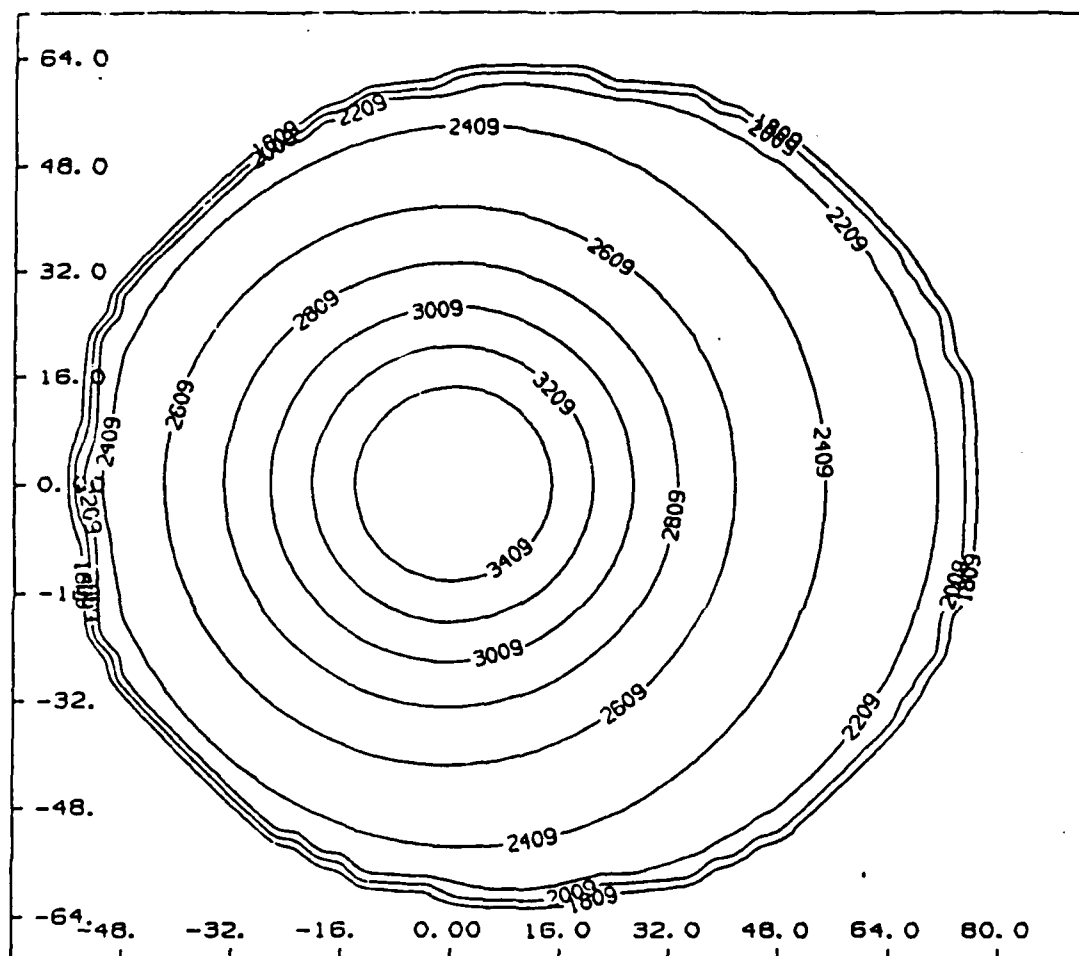
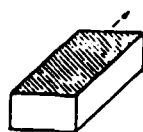
Meters $\times 10^{-5}$

Figure 3.3.8 Melt Pool Solid/Liquid Interface
(Power = 240 W, $U_s = 0.012$ m/s)



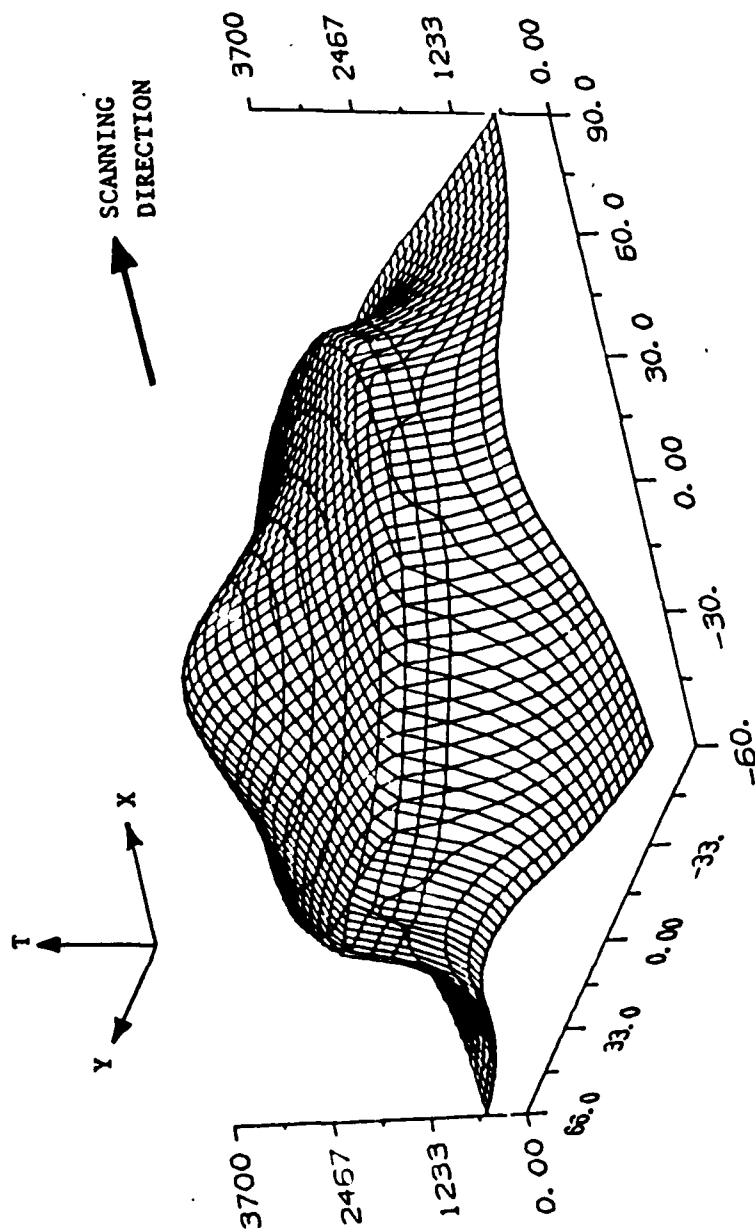
Meters *(E-05)

Figure 3.3.9 Melt Pool Isotherms in the X-Z Plane
with Y Located at the Symmetry Plane
(Power = 400 W, $U_s = 0.02$ m/s)



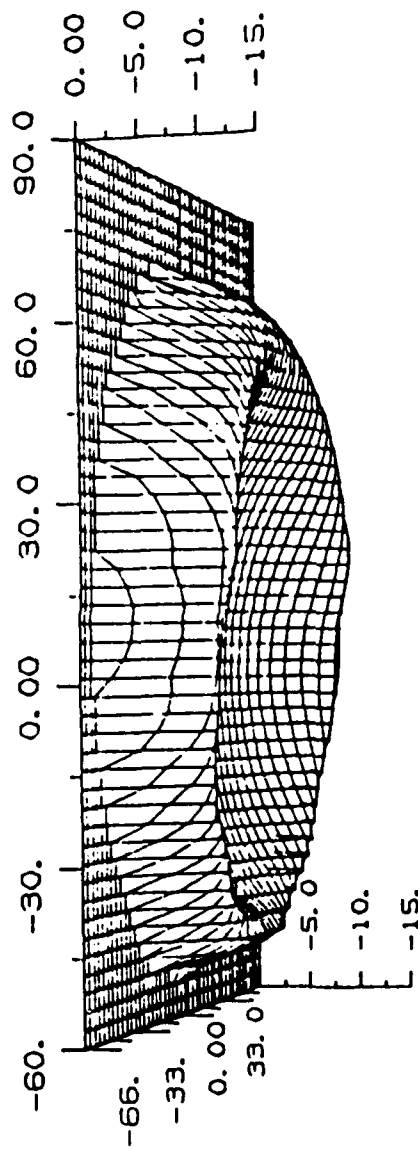
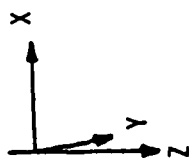
Meters $\times (E-05)$

Figure 3.3.10 Melt Pool Isotherms in the X-Y Plane
with Z Located at the Material Surface
(Power = 400 W, $U_s = 0.02$ m/s)



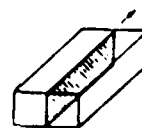
Meters *(E-05)

Figure 3.3.11 Surface Temperature Contours
(Power = 400 W, $U_s = 0.02$ m/s)



Meters $\times 10^{-5}$

Figure 3.3.12 Melt Pool Solid/Liquid Interface
(Power = 400 W, $U_s = 0.02$ m/s)



U-W VELOCITIES

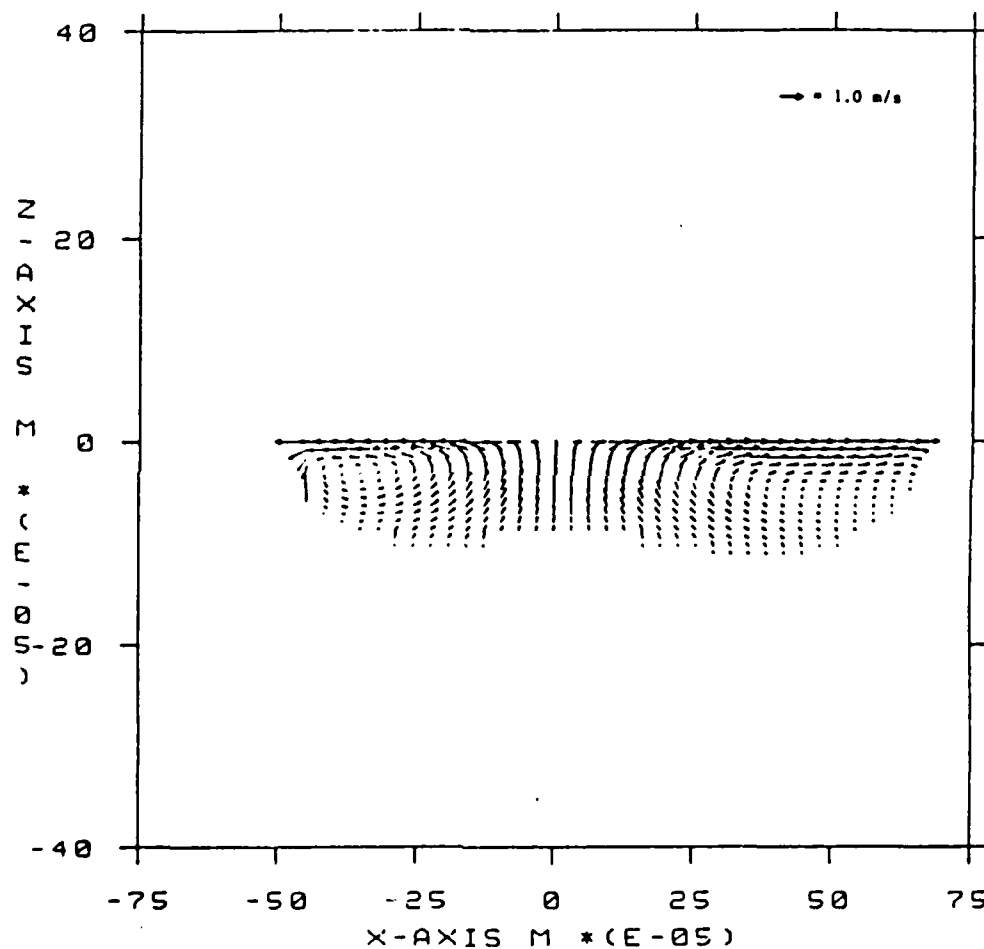


Figure 3.3.13 Melt Pool Velocity Field in the X-Z Plane
with Y Located at the Symmetry Plane
(Power = 240 W, $U_s = 0.012$ m/s)

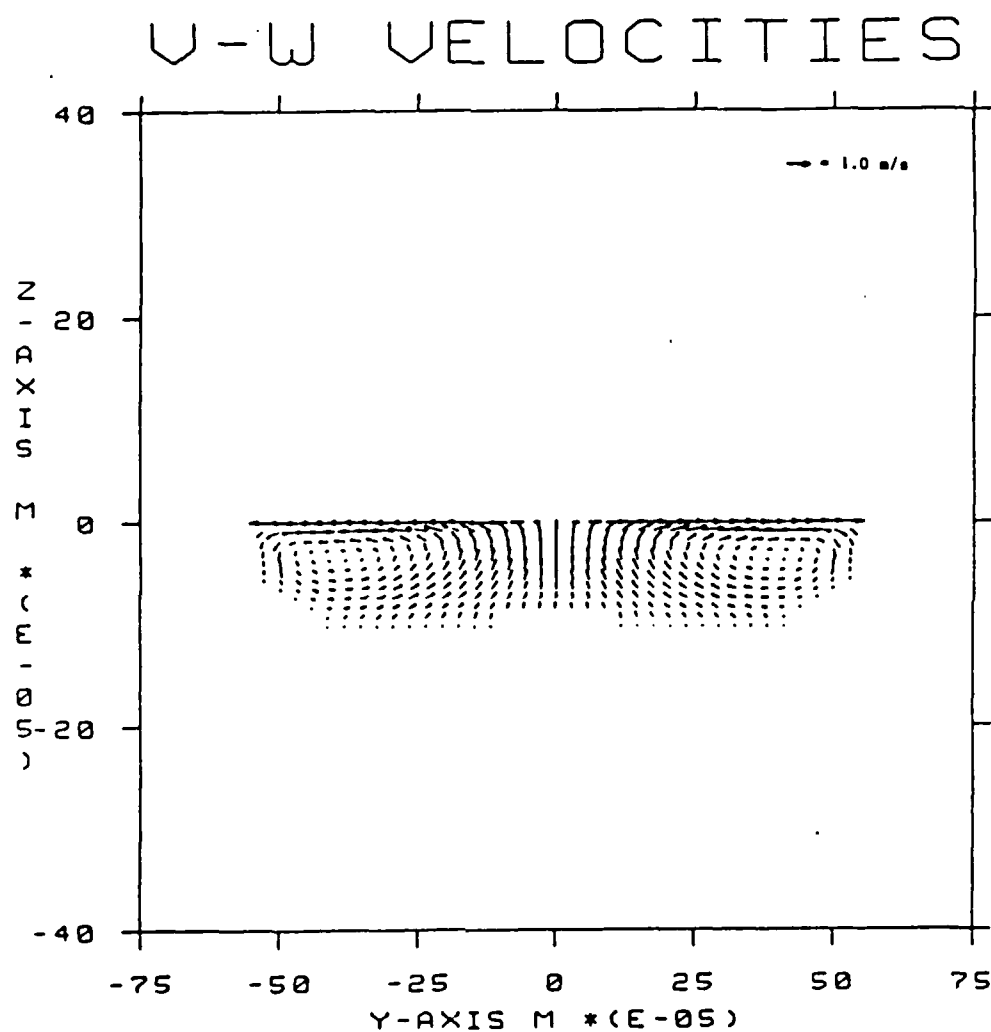
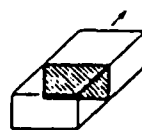
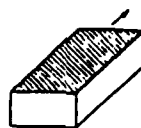


Figure 3.3.14 Melt Pool Velocity Field in the Y-Z Plane
 with X Located at the Beam Center
 (Power = 240 W, $U_s = 0.012$ m/s)



U-V VELOCITIES

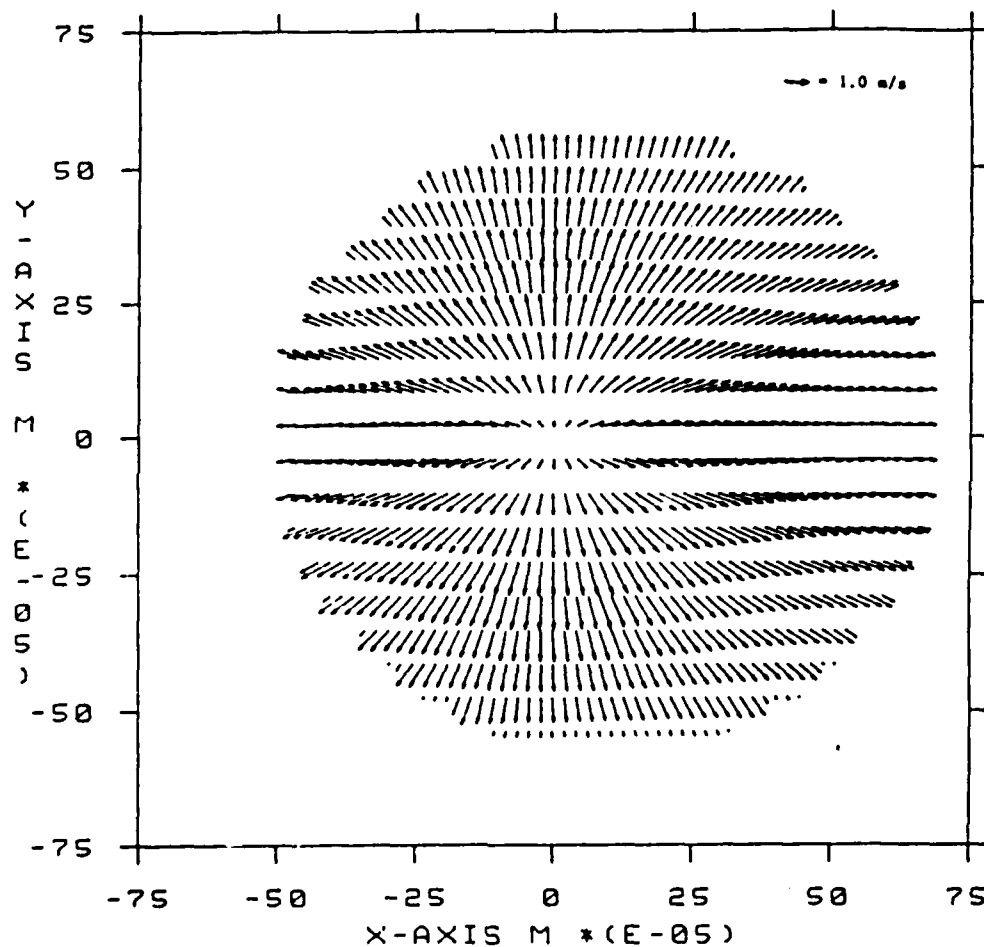


Figure 3.3.15 Melt Pool Velocity Field in the X-Y Plane
with Z Located at the Material Surface
(Power = 240 W, $U_s = 0.012$ m/s)

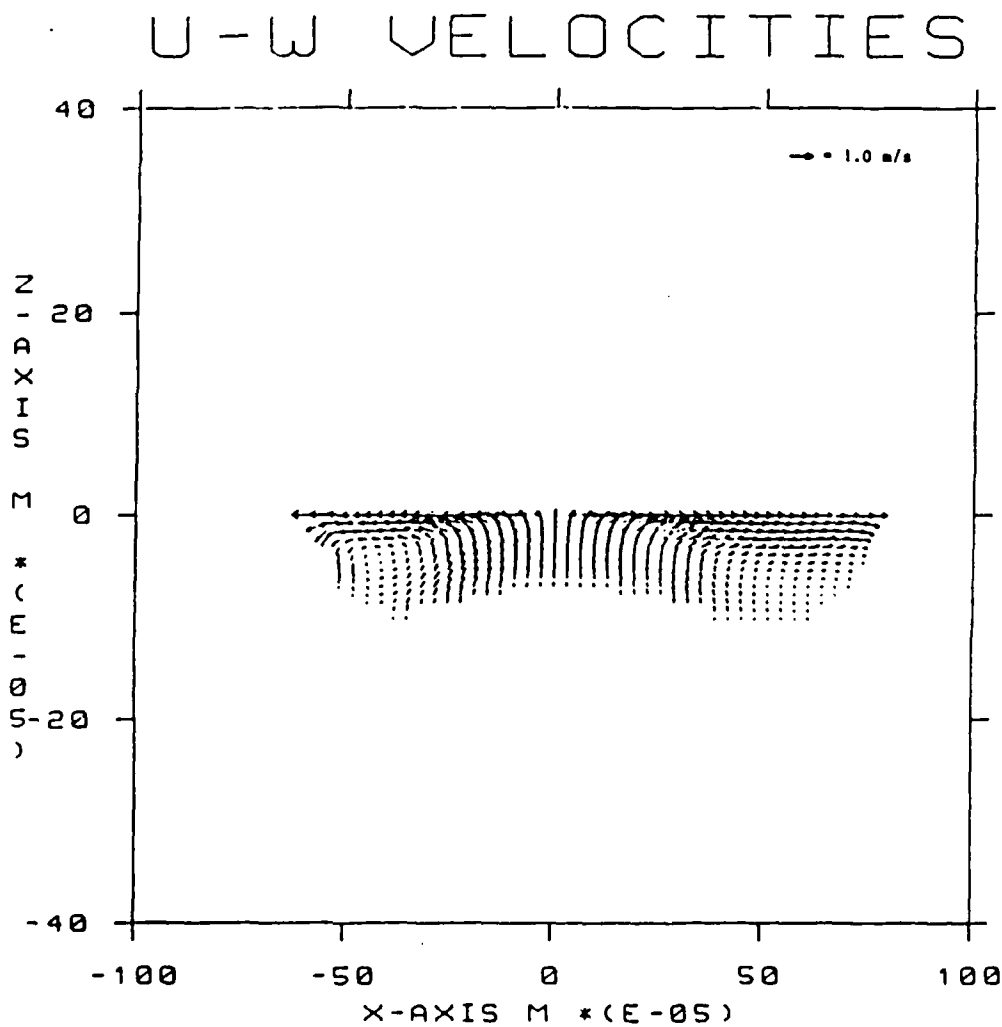
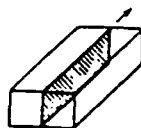


Figure 3.3.16 Melt Pool Velocity Field in the X-Z Plane
with Y Located at the Symmetry Plane
(Power = 400 W, $U_s = 0.02$ m/s)

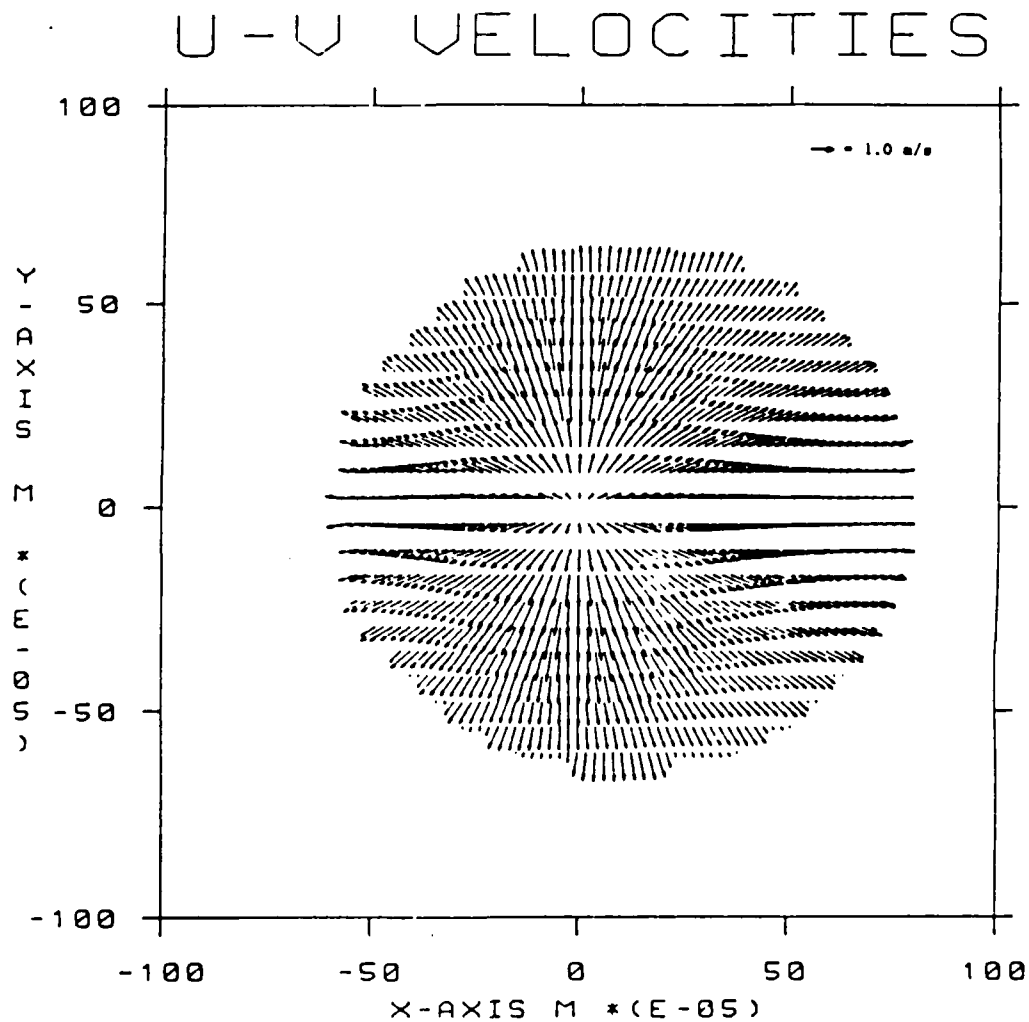
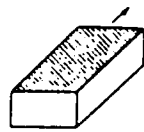
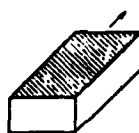


Figure 3.3.17 Melt Pool Velocity Field in the X-Y Plane
with Z Located at the Material Surface
(Power = 400 W, $U_s = 0.02$ m/s)



TEMPERATURE vs DISTANCE

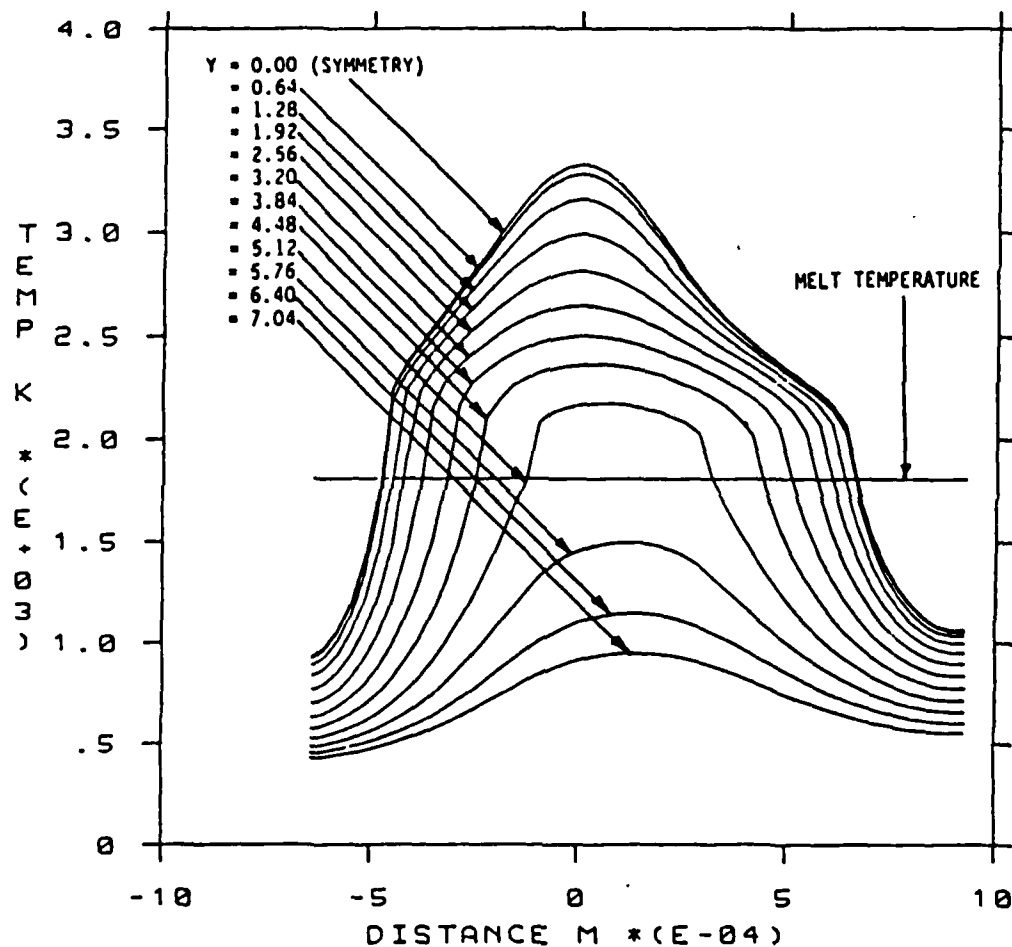
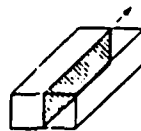


Figure 3.3.18 Surface Temperature versus Distance(X) for Various Locations(Y) Away from the Beam Center (Power = 240 W, $U_s = 0.012$ m/s)



TEMPERATURE vs DISTANCE

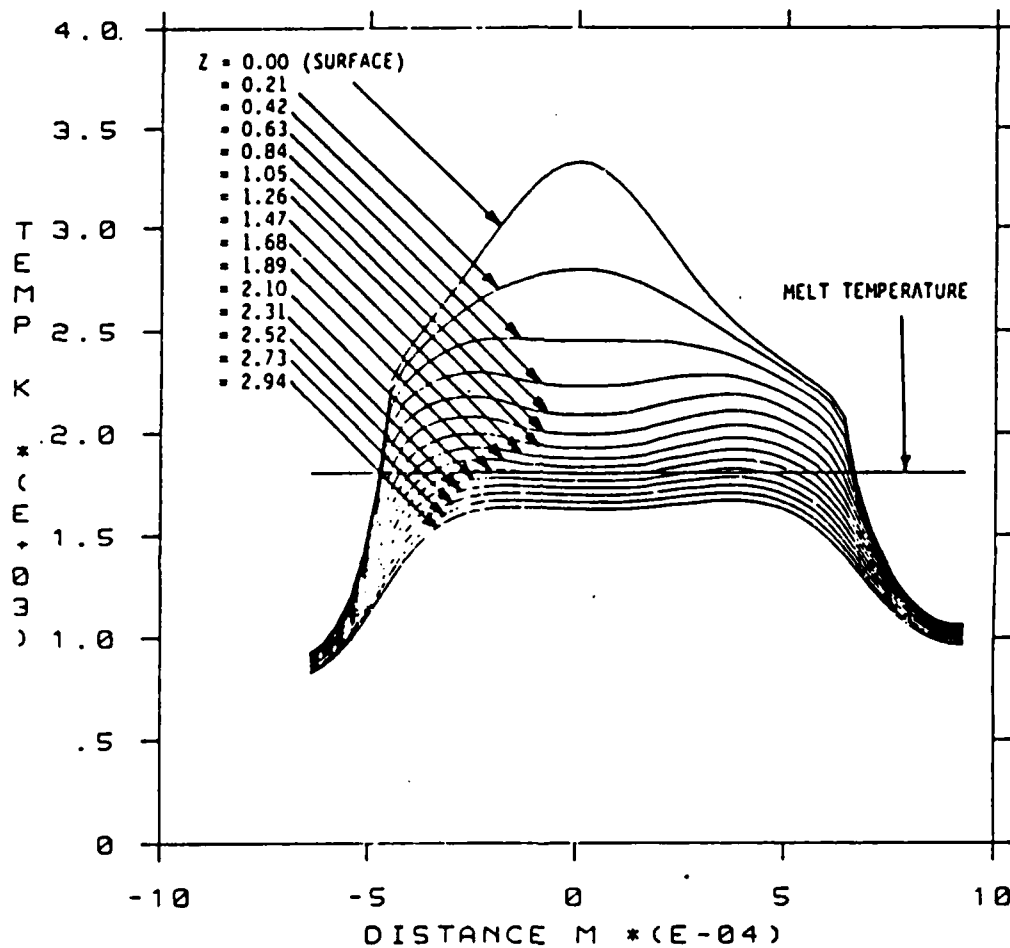
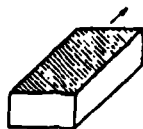


Figure 3.3.19 Symmetry Plane Temperature versus Distance(X) for Various Locations(Z) Beneath the Domain Surface
(Power = 240 W, $U_s = 0.012$ m/s)



TEMPERATURE vs DISTANCE

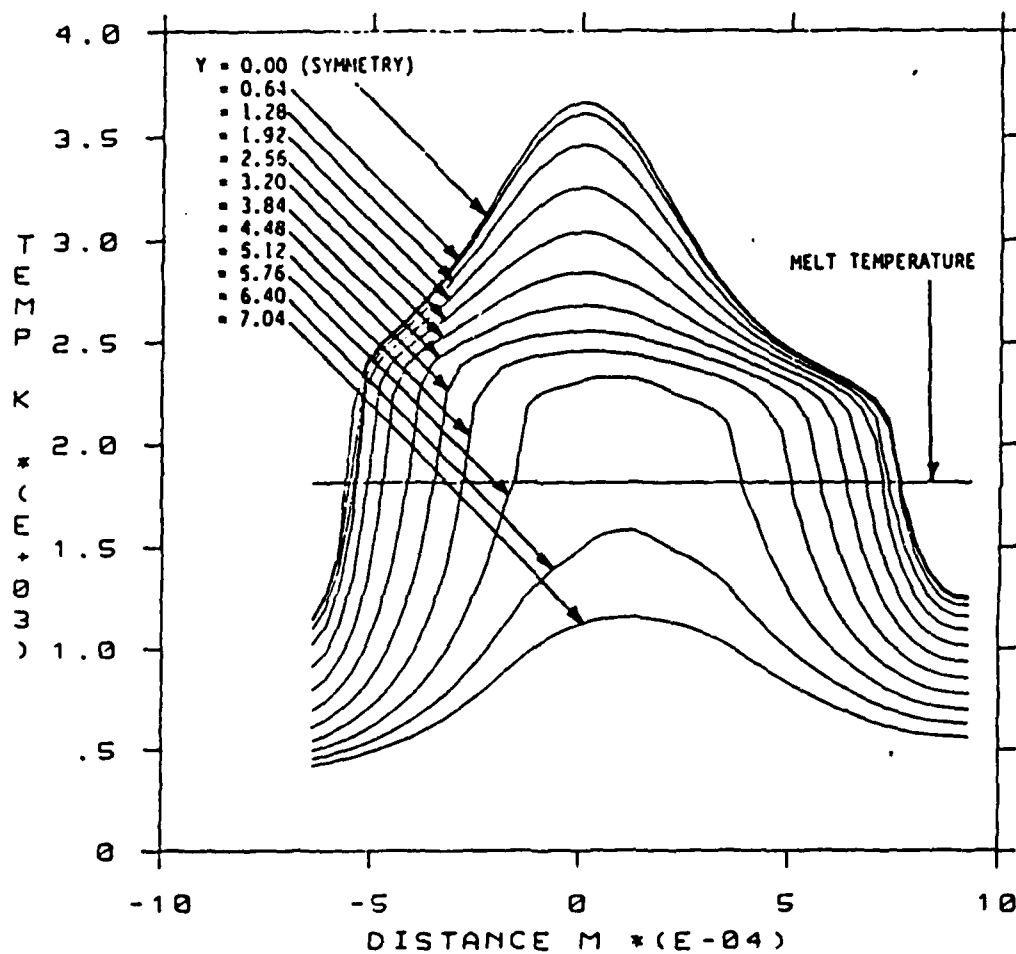


Figure 3.3.20 Surface Temperature versus Distance(X) for Various Locations(Y) Away from the Beam Center (Power = 400 W, $U_s = 0.02$ m/s)

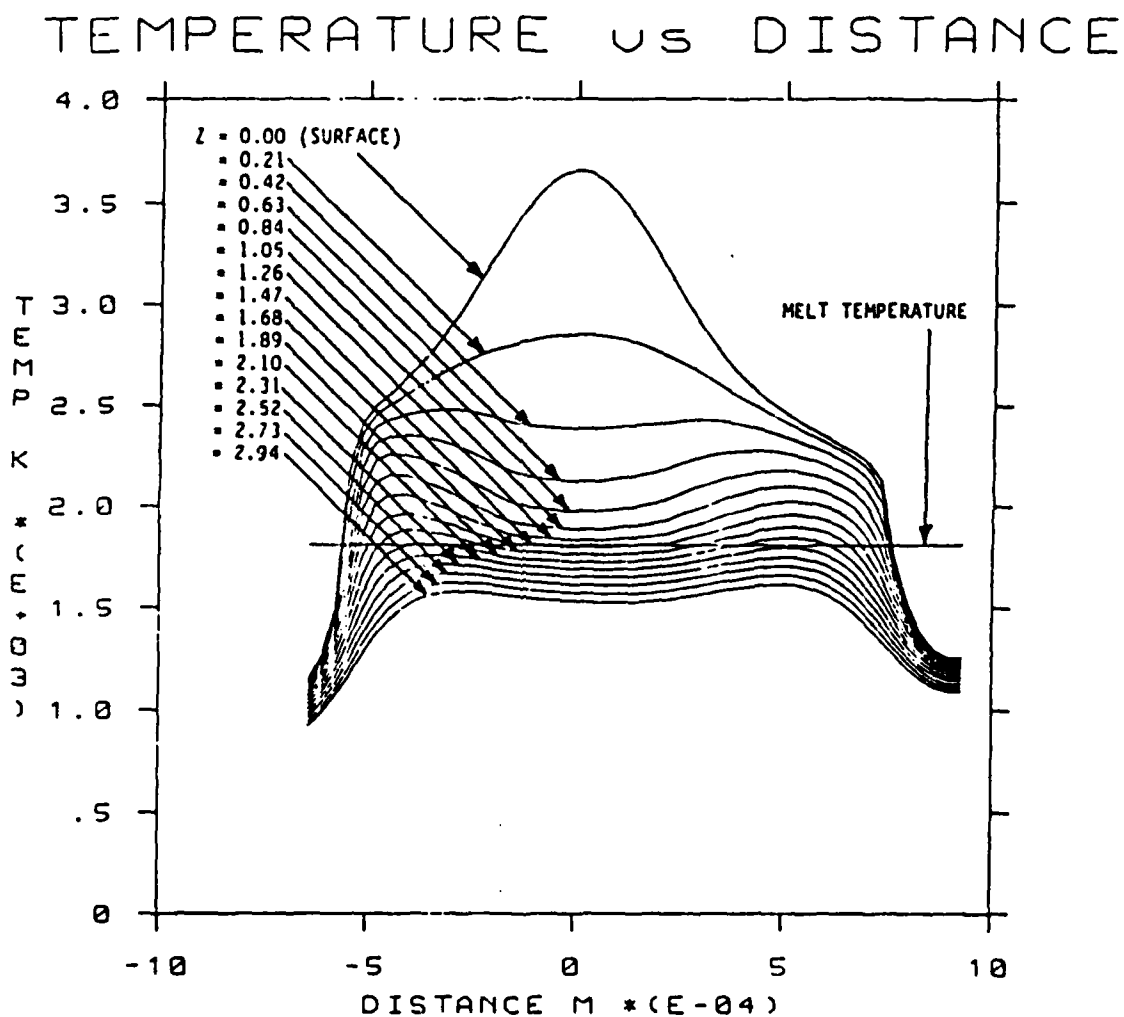
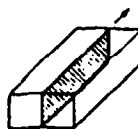
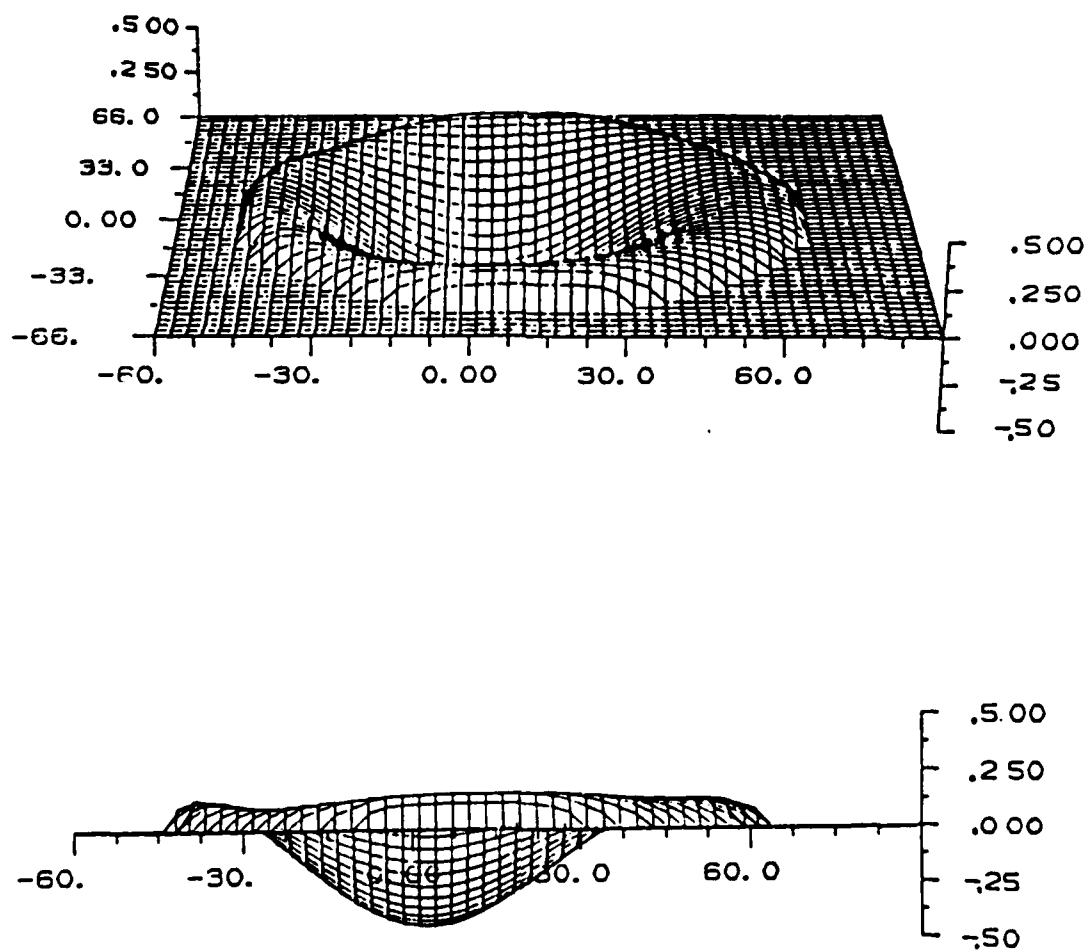


Figure 3.3.21 Symmetry Plane Temperature versus Distance(X) for Various Locations(Z) Beneath the Domain Surface (Power = 400 W, $U_s = 0.02$ m/s)



Meters $\times (E-05)$

Figure 3.3.22 Restricted Free Surface Deformation Based
on Local Pressure Only
(Power = 240 W, $U_s = 0.012$ m/s)

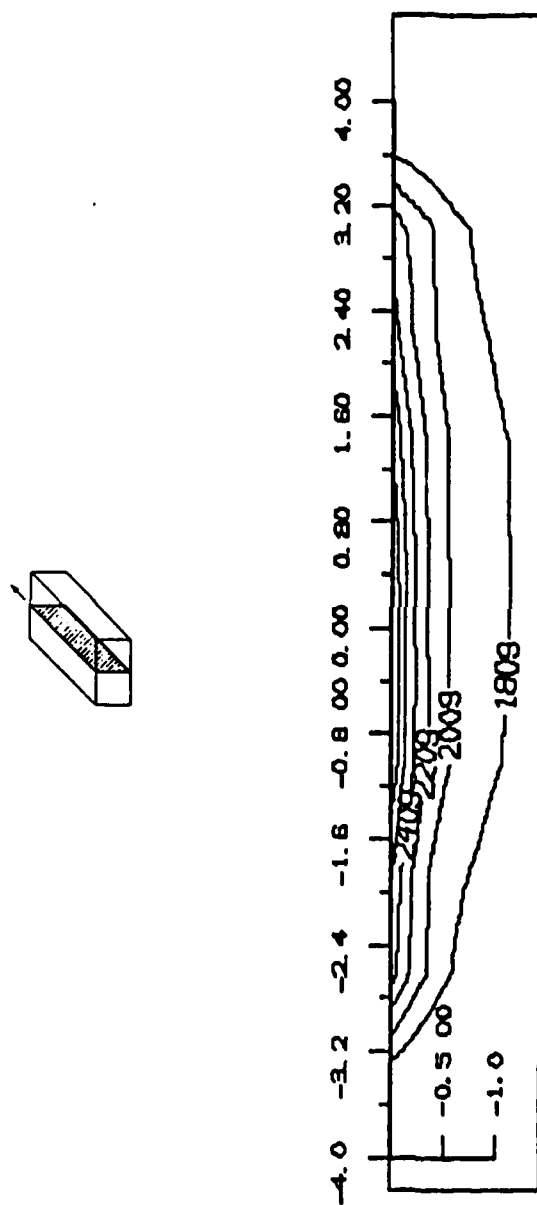


Figure 3.3.23 Melt Pool Isotherms in the X-Z Plane
with Y Located at the Symmetry Plane
(Power = 200 W, $U_s = 0.010$ m/s)

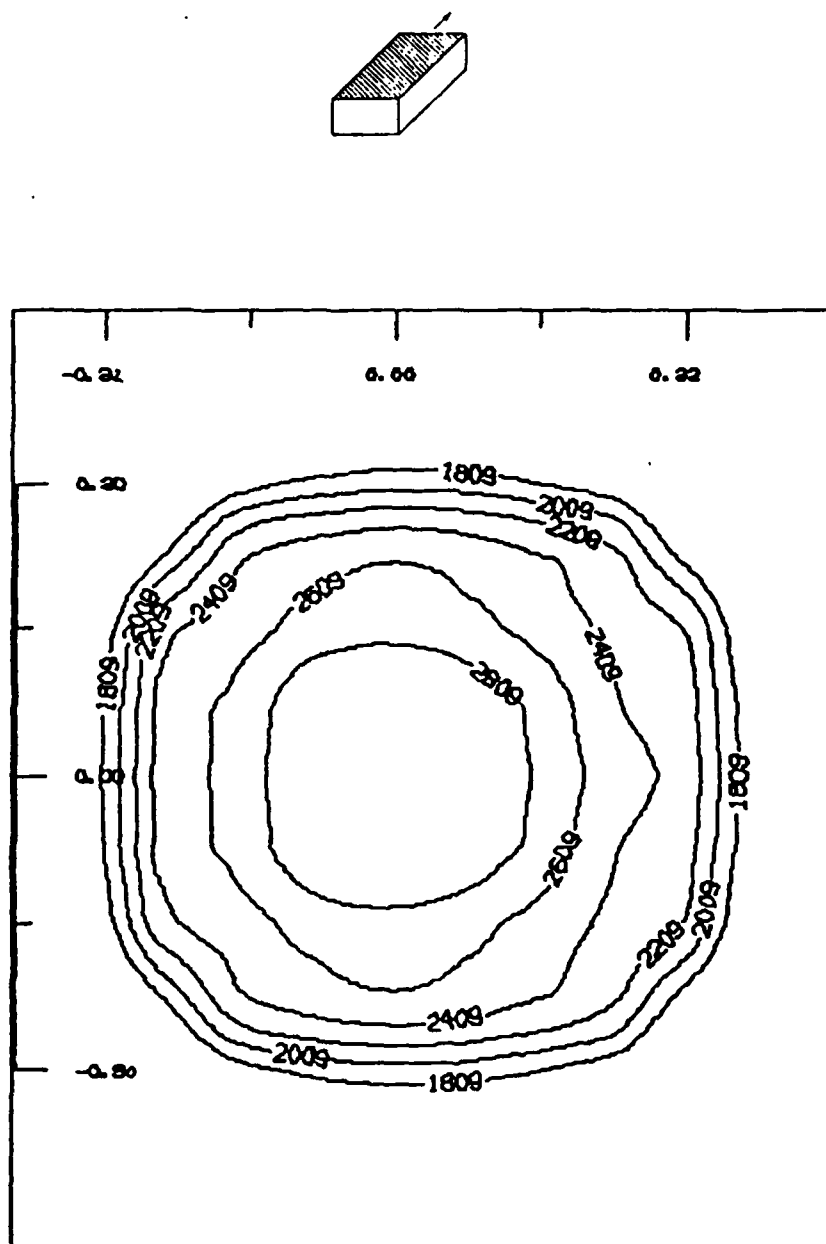


Figure 3.3.24 Melt Pool Isotherms in the X-Y Plane
with Z Located at the Material Surface
(Power = 200 W, $U_s = 0.010$ m/s)

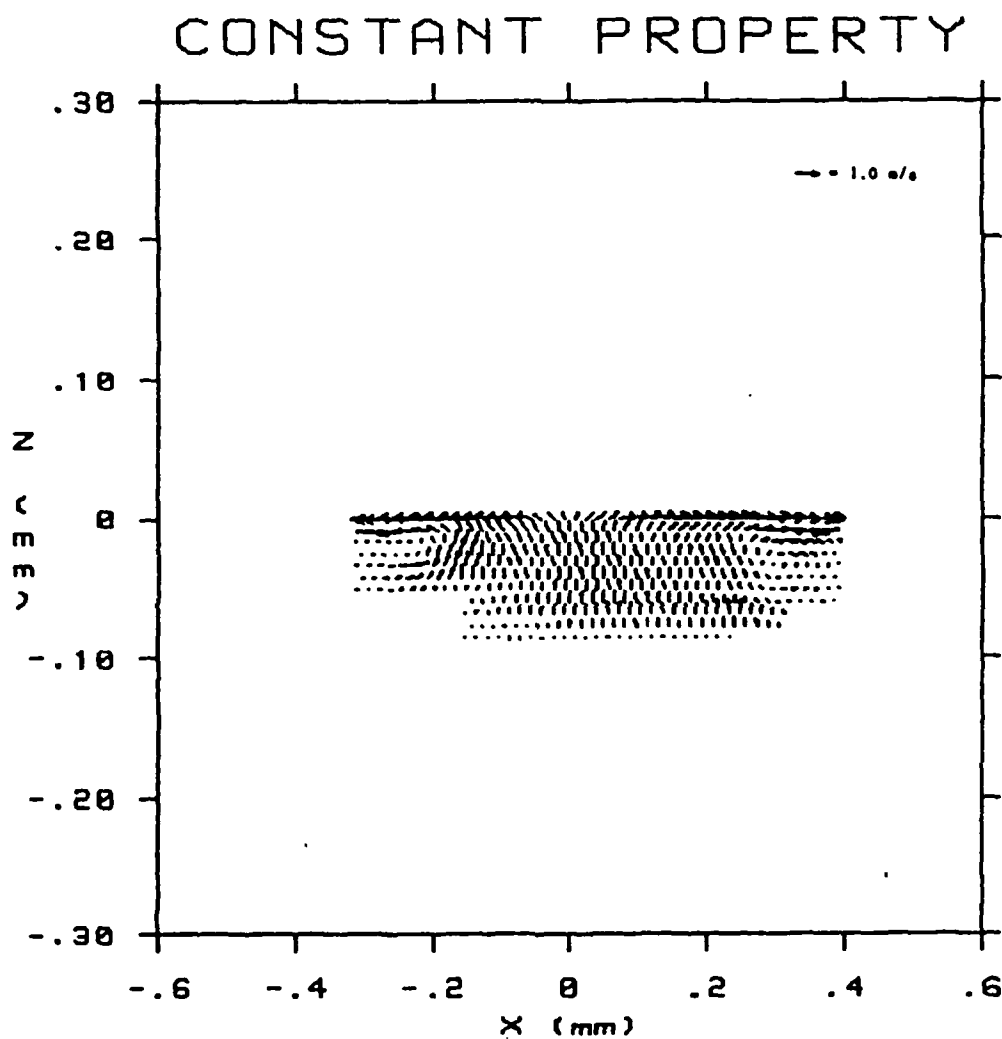
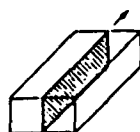


Figure 3.3.25 Melt Pool Velocity Field in the X-Z Plane
with Y Located at the Symmetry Plane
(Power = 200 W, $U_s = 0.010 \text{ m/s}$)

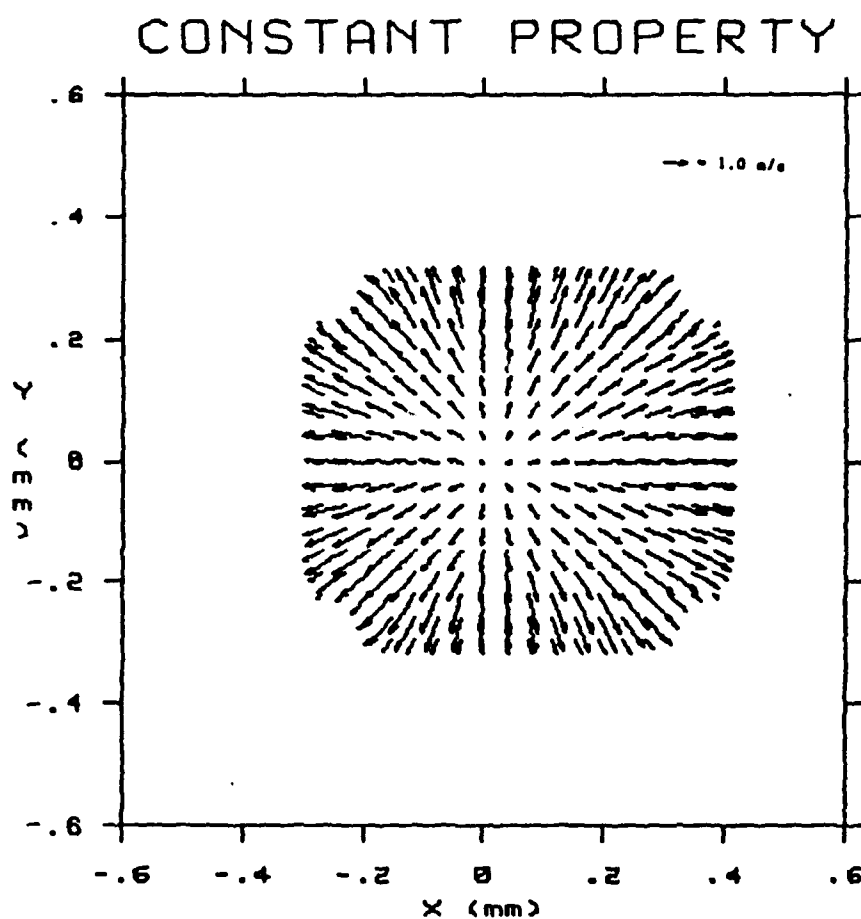
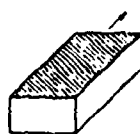


Figure 3.3.26 Melt Pool Velocity Field in the X-Y Plane
with Z Located at the Material Surface
(Power = 200 W, $U_s = 0.010 \text{ m/s}$)

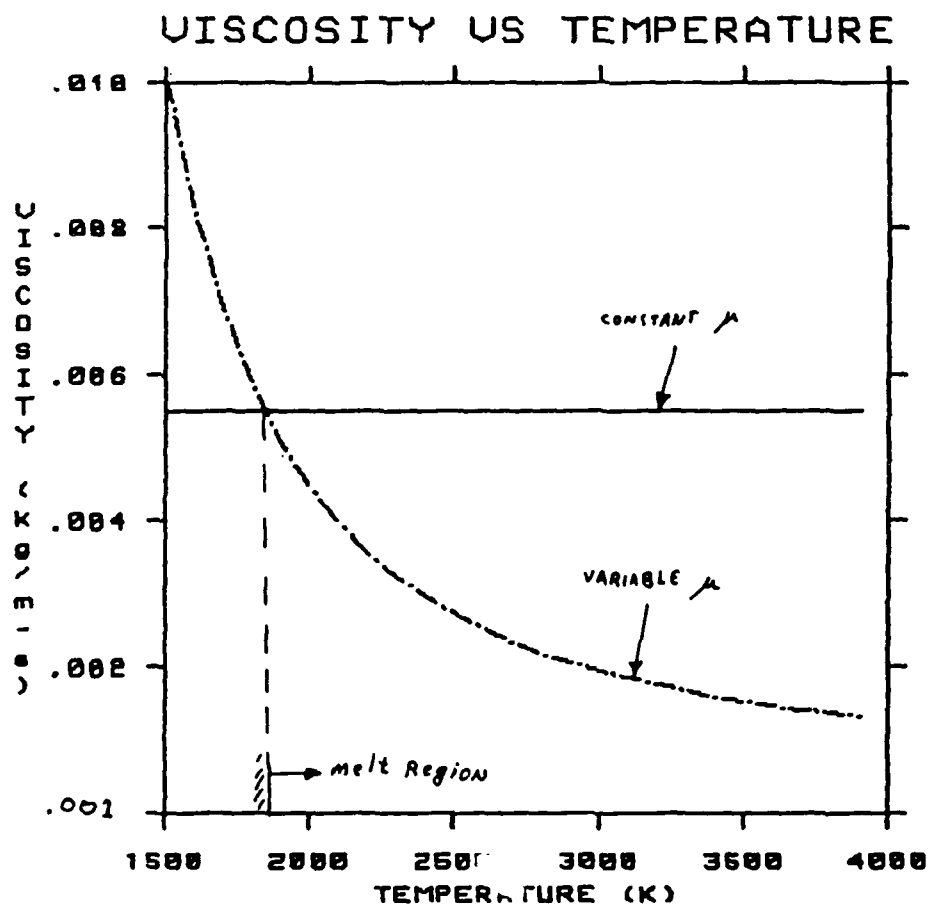


Figure 3.3.27 Variation of Viscosity with Temperature

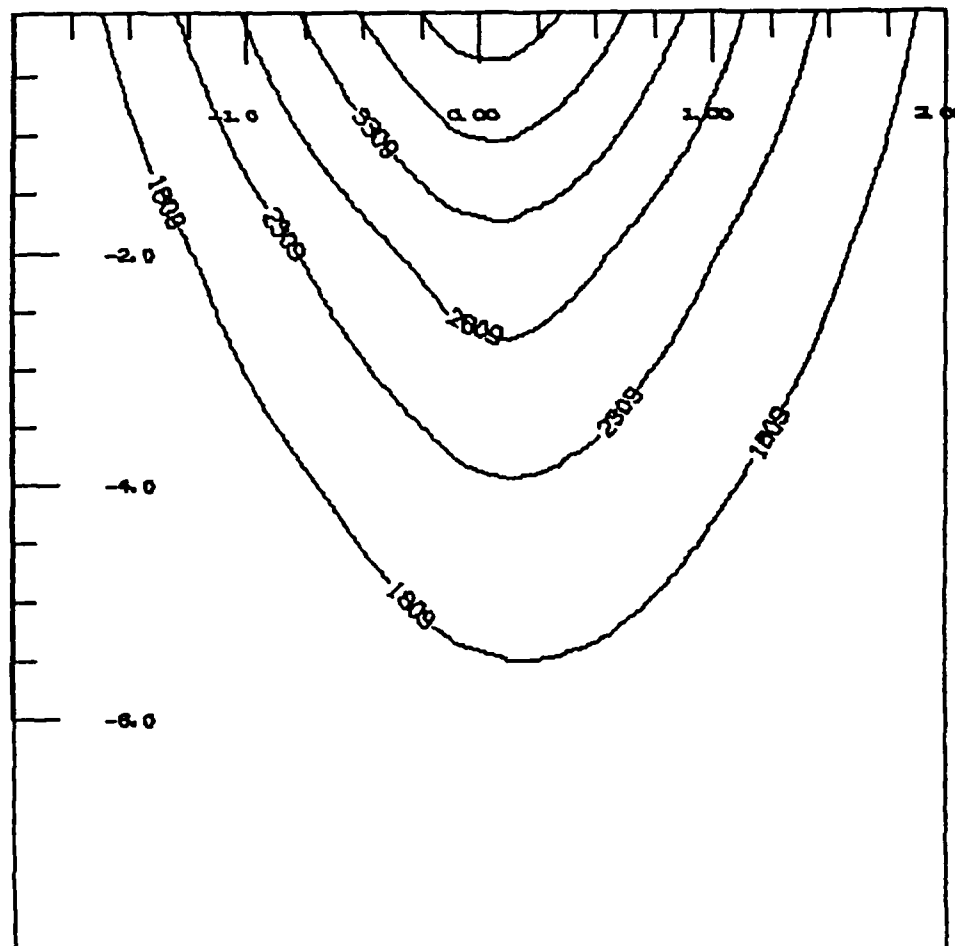
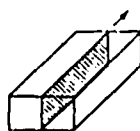


Figure 3.3.28 Melt Pool Isotherms in the X-Z Plane
with Y Located at the Symmetry Plane
(Power = 200 W, $U_s = 0.010$ m/s)
(JxB Forces Only)

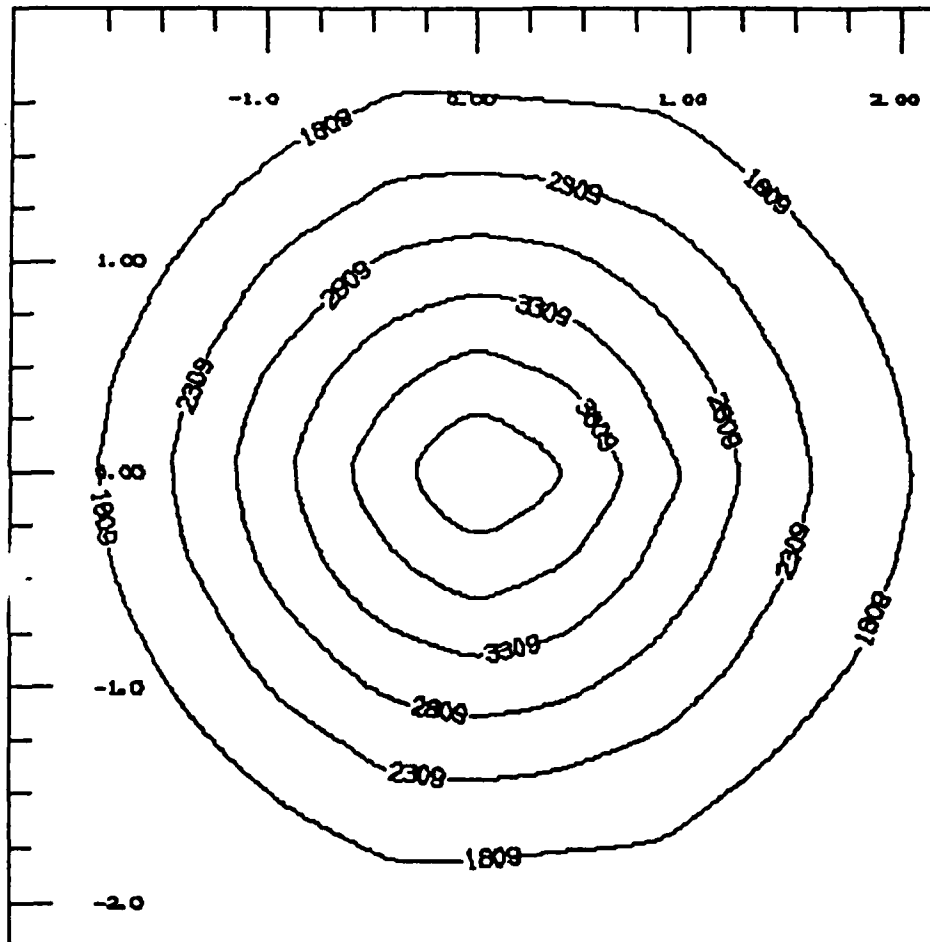
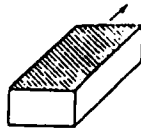
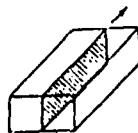


Figure 3.3.29 Melt Pool Isotherms in the X-Y Plane
with Z Located at the Material Surface
(Power = 200 W, $U_s = 0.010$ m/s)
(JxB Forces Only)



$\bar{J} \times \bar{B}$ DRIVEN

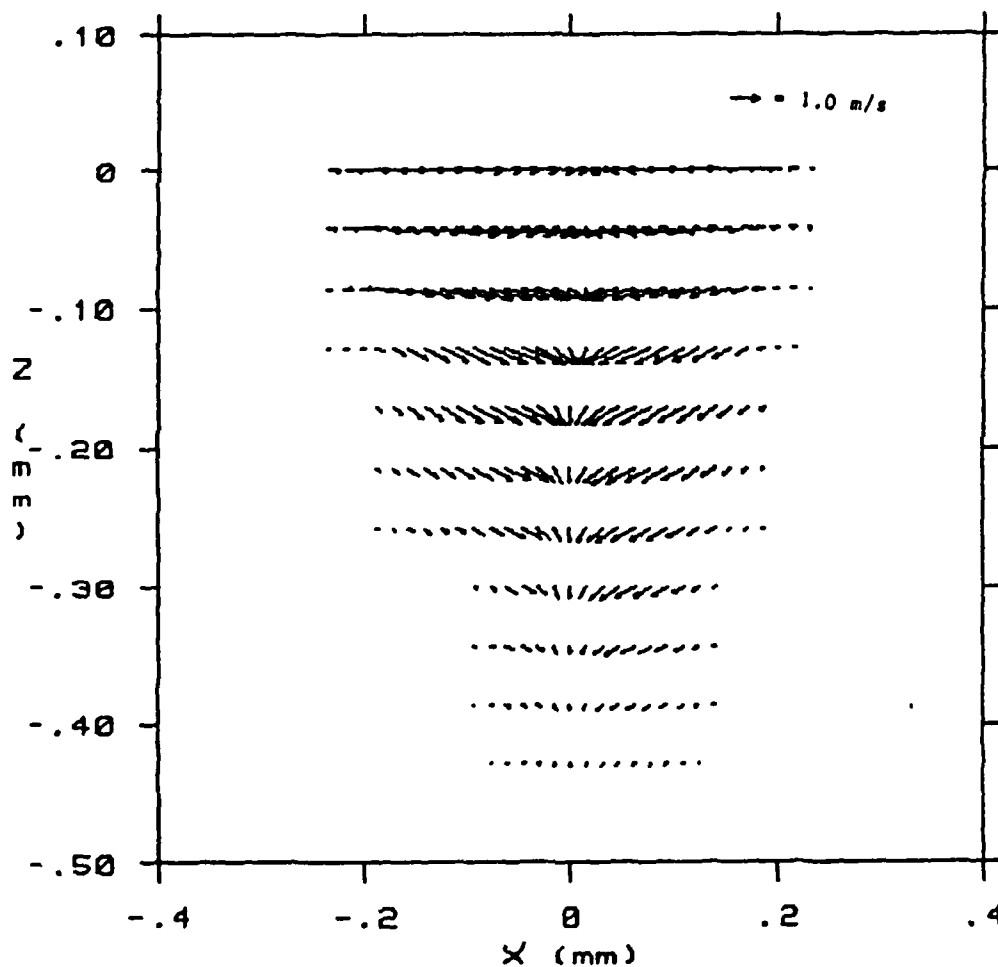


Figure 3.3.30 Melt Pool Velocity Field in the X-Z Plane
with Y Located at the Symmetry Plane
(Power = 200 W, $U_s = 0.010$ m/s)
($\bar{J} \times \bar{B}$ Force Only)

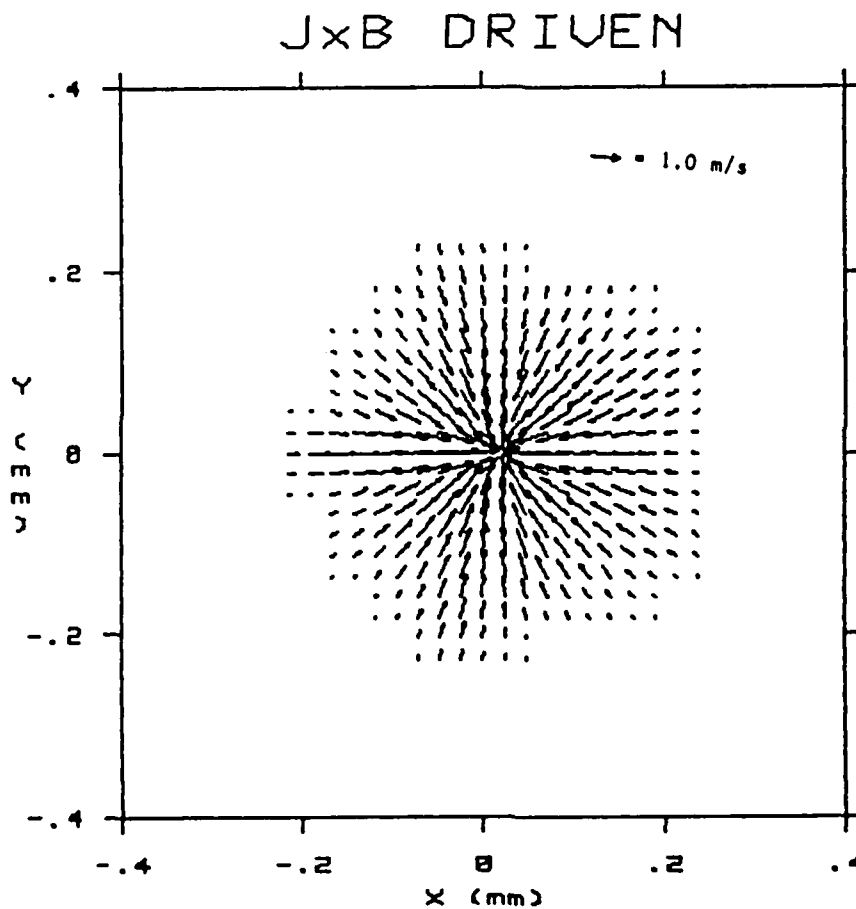
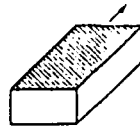


Figure 3.3.31 Melt Pool Velocity Field in the X-Y Plane
with Z Located at the Material Surface
(Power = 200 W, $U_s = 0.010$ m/s)
(JxB Forces Only)

Table 3.3.1 Governing Parameters

PARAMETERS FOR STEEL

$\Delta x = \Delta y$	= 3.20 (10) ⁻⁵	m
Δz	= 1.05 (10) ⁻⁵	m
ρ	= 7800.0	kg/m ³
k	= 30.0	W/mK
C_p	= 800.0	J/kgK
μ	= 0.0275	Ns/m ²
σ_{actual}	= 1.872	N/m
σ_{test}	= 187.2	N/m
T_{melt}	= 1809.0	K
T_{∞}	= 300.0	K
r_{beam}	= 0.275	mm

Table 3.3.2 Test Case Powers and Scanning Speeds

TEST CASES

<u>CASE NUMBER</u>	<u>POWER (W)</u>	<u>SCANNING SPEED (M/S)</u>
I	200	0.010
II	240	0.012
III	280	0.014
IV	320	0.016
V	400	0.020
VI	400	0.024

Table 3.3.3 Boundary Layer Thickness Estimates
for Various Test Cases.

POWER (W)	SCANNING SPEED (m/s)	δ_v		δ_T	
		Re_+	* METER (E-06)	Pe_+	* METER (E-06)
240.0	0.012	924.9	36.8	678.3	43.0
280.0	0.014	1063.7	36.3	780.1	42.4
320.0	0.016	1324.8	34.3	971.5	40.0
400.0	0.020	1511.6	33.7	1108.5	39.4

⁺based on the calculated pool length (X) and the maximum surface (U) velocity.

Table 3.3.4 U-Velocity Variations Due to Variable Viscosity
 Along the Surface of the X-Z Plane with Y Located
 at the Symmetry Plane (Power = 200 W, $U_s = 0.010$ m/s)

(X-X ₀) (mm)	U (m/s)	U* (m/s)	ΔU (m/s)	%
-.320	.000	.000	.000	.000
-.280	-1.283	-1.304	.021	1.624
-.240	-2.566	-2.608	.042	1.625
-.200	-1.947	-1.983	.036	1.867
-.160	-1.327	-1.358	.031	2.335
-.120	-1.175	-1.192	.017	1.467
-.080	-1.023	-1.026	.003	.341
-.040	-.489	-.497	.008	1.595
.000	.044	.032	-.012	-27.622
.040	.371	.377	.006	1.691
.080	.697	.722	.025	3.536
.120	1.048	1.070	.022	2.110
.160	1.399	1.418	.020	1.398
.200	1.486	1.518	.032	2.159
.240	1.573	1.618	.045	2.835
.280	2.255	2.217	-.038	-1.679
.320	2.936	2.816	-.120	-4.097
.360	1.468	1.408	-.060	-4.098
.400	.000	.000	.000	.000

Table 3.3.5 V-Velocity Variations Due to Variable Viscosity
 Along the Surface of th Y-Z Plane with X Located
 at the Beam Center (Power = 200 W, $U_s = 0.010$ m/s)

(Y-Yo) (mm)	V (m/s)	V* (m/s)	ΔV (m/s)	%
-.320	.000	.000	.000	.000
-.280	-1.299	-1.337	.038	2.916
-.240	-2.599	-2.674	.076	2.916
-.200	-1.955	-1.973	.018	.930
-.160	-1.311	-1.271	-.039	-3.008
-.120	-1.102	-1.072	-.030	-2.719
-.080	-.893	-.872	-.020	-2.296
-.040	-.447	-.436	-.011	-2.487
.000	.000	.000	.000	.000
.040	.447	.436	-.011	-2.487
.080	.893	.872	-.020	-2.296
.120	1.102	1.072	-.030	-2.719
.160	1.311	1.271	-.039	-3.008
.200	1.955	1.973	.018	.930
.240	2.599	2.674	.076	2.916
.280	1.299	1.337	.038	2.916
.320	.000	.000	.000	.000

Table 3.3.6 W-Velocity Variations Due to Variable Viscosity
in the X-Z Plane with X and Y Located
at the Beam Center (Power = 200, $U_s = 0.010$ m/s)

(Z-Zo) (mm)	W (m/s)	W* (m/s)	ΔW (m/s)	%
-.000	.000	.000	.000	.000
-.004	.119	.129	.010	8.063
-.008	.238	.257	.019	8.063
-.012	.236	.242	.006	2.734
-.016	.234	.227	-.006	-2.702
-.020	.254	.247	-.006	-2.443
-.024	.273	.267	-.006	-2.221
-.028	.257	.247	-.010	-4.040
-.032	.241	.227	-.015	-6.099
-.036	.253	.241	-.013	-4.973
-.040	.266	.255	-.010	-3.949
-.044	.250	.238	-.012	-4.810
-.048	.235	.221	-.014	-5.784
-.052	.243	.225	-.018	-7.360
-.056	.251	.229	-.022	-8.833
-.060	.238	.215	-.023	-9.712
-.064	.225	.201	-.024	-10.691
-.068	.238	.234	-.004	-1.717
-.072	.251	.267	.016	6.348
-.076	.152	.184	.032	21.130
-.080	.053	.101	.048	91.646
-.084	.026	.050	.024	91.646
-.088	.000	.000	.000	.000

Table 3.3.7 Variation of U-Velocities Due to Electromagnetic Forces (JxD with Surface Tension) in the X-Y Plane with Z Located at the Material Surface
(Power = 200 W, $U_s = 0.010$ m/s, Current = 100 Amps)

(X-Xo) (mm)	U (m/s)	U* (m/s)	ΔU (m/s)	%
-.320	.000	.000	.000	.000
-.280	-1.304	-1.245	-.059	-4.493
-.240	-2.608	-2.491	-.117	-4.494
-.200	-1.983	-1.869	-.114	-5.762
-.160	-1.358	-1.247	-.111	-8.198
-.120	-1.192	-1.098	-.094	-7.910
-.080	-1.026	-.949	-.077	-7.528
-.040	-.497	-.458	-.040	-7.964
.000	.032	.034	.002	6.116
.040	.377	.334	-.043	-11.283
.080	.722	.635	-.087	-12.048
.120	1.070	.989	-.081	-7.555
.160	1.418	1.344	-.075	-5.269
.200	1.518	1.434	-.084	-5.536
.240	1.618	1.525	-.093	-5.770
.280	2.217	2.075	-.141	-6.372
.320	2.816	2.626	-.189	-6.718
.360	1.408	1.313	-.095	-6.718
.400	.000	.000	.000	.000

Table 3.3.8 Variation of V-Velocities Due to Electromagnetic Forces (JxD with Surface Tension) in the X-Y Plane with Z Located at the Material Surface
(Power = 200 W, $U_s = 0.010$ m/s, Current = 100 Amps)

(Y-Y ₀) (mm)	V (m/s)	V* (m/s)	ΔV (m/s)	%
-.320	.000	.000	.000	.000
-.280	-1.299	-1.192	-.107	-8.254
-.240	-2.599	-2.384	-.214	-8.254
-.200	-1.955	-1.784	-.171	-8.759
-.160	-1.311	-1.183	-.128	-9.761
-.120	-1.102	-1.015	-.087	-7.878
-.080	-.893	-.847	-.046	-5.113
-.040	-.447	-.423	-.023	-5.240
.000	.001	.001	.000	.000
.040	.447	.423	-.023	-5.240
.080	.893	.847	-.046	-5.113
.120	1.102	1.015	-.087	-7.878
.160	1.311	1.183	-.128	-9.761
.200	1.955	1.784	-.171	-8.759
.240	2.599	2.384	-.214	-8.254
.280	1.299	1.192	-.107	-8.254
.320	.000	.000	.000	.000

3.4 Experimental Verification

3.4.1 Introduction

In this section, two experiments are described. These experiments are performed to examine the validity of the models. It should be kept in mind that there is no thermophysical properties (not to mention the temperature dependence) data available for high or moderately high melting point materials such as steel and aluminum. In view of this, exact match of experimental and theoretical predictions are unlikely. However, trends of experimental and theoretical predictions should agree to each other. The first experiment is to compare the aspect ratio of the pool shape (width/depth) of the experimental and theoretical predictions. It can be seen from Eq. (3.1.19) that both Reynolds number and Marangoni number are directly proportional to the power absorbed. These parameters therefore serve the purpose of the comparison. The second experiment is to obtain the magnitude of the recirculating flow and the cooling rate. This is done by x-ray shadow graph using a real-time radiography system.

3.4.2 Experimental Procedure

a. Micrograph of Resolidified Region: A schematic diagram of the experimental set up is shown in Fig. 3.4.1. A 10 kW CO₂ continuous laser is used. The materials used are AISI 1016 mild steel. The steel bar is of dimension 150 mm long, 50 mm wide, and 6 mm thick. The surface being irradiated by the laser is ground. The surface is cleaned by using alcohol right before the run to avoid any unnecessary containment.

Samples for the cross-section of laser melt were cut, hand polished, and etched for optical microscopy. The melted region is identified and the aspect ratio of the melted region is estimated.

b. X-ray Shadow Graph: A schematic diagram of the experimental set up is shown in Fig. 3.4.2. An arc is used as the heat source. The materials used are aluminum. Tungsten particles are used as tracers to provide contrast. Microfocus x-ray is used to produce a focused x-ray beam. This x-ray beam is directed through the test section. An image intensifier is located on the back to receive the image. This image is processed and stored on video tape. Because of density difference between aluminum and tungsten, the tungsten particles can be traced as they travel with the motion of the molten aluminum. Density difference due to temperature variation can also be recorded.

3.4.3 Results and Discussion

a. Micrograph of Resolidified Region: The experimental runs for various process parameters - laser power, beam diameter, and scanning speed - are tabulated in Table 3.4.1. A picture of the microstructure of case #6 is shown in Fig. 3.4.3. The melted region can be distinguished from the unmelted region. The aspect ratios based on these micrographs are calculated and tabulated in Table 3.4.1. It can be seen that the aspect ratio increases with respect to laser power which is consistent with the theoretical prediction. The experimental aspect ratio varies from 3.375 to 4.0. The theoretical models predicts 4.0 to 5.0 for the aspect ratio.

b. X-ray Shadow Graph: In Fig. 3.4.4, two successive frames of the x-ray shadow graph are shown. The locations of the center line and tungsten particle are shown by the vertical lines. The left line directly underneath

the arc is the center line. The right line is the location of the tungsten particle. Assuming that the particle travel with the motion of the molten materials, the speed of the recirculating flow can be estimated. It is found to be of the order 1 m/sec which is of the same order of magnitude of the theoretical prediction.

A sequence of four frames at 0, 1, 5, and 9 seconds after the arc is turned off are restored by using a frame grabber. The first frame is used as a reference. Three consecutive frames each four seconds apart are produce from the next three frames and plotted in Fig. 3.4.5 through 3.4.7. Each frame is produced by subtracting the intensity from the reference frame. The difference in intensity, which is caused by different density and hence different temperature, is color enhanced. The change in the color is therefore a measure of the cooling rate. It can be observed that the cooling rate is non-uniform within the molten region. It has a higher cooling rate on the surface than near the bottom. This is consistent with the theoretical prediction.

3.4.4 Conclusion

Two experiments are performed to examine the validity of the theoretical models. The first experiment compares the aspect ratio of the molten pool. It is found that the theoretical and experimental results have the same trend. An increase in laser power increases the aspect ratio. The aspect ratio of the two predictions are within 20 percent. The second experiment is to obtain a measure of the velocity field and cooling rate. It is found that the recirculating flow is of the order 1 m/sec. The cooling rate within the molten region is found to be non-uniform. It is higher on the surface and lower near the bottom.

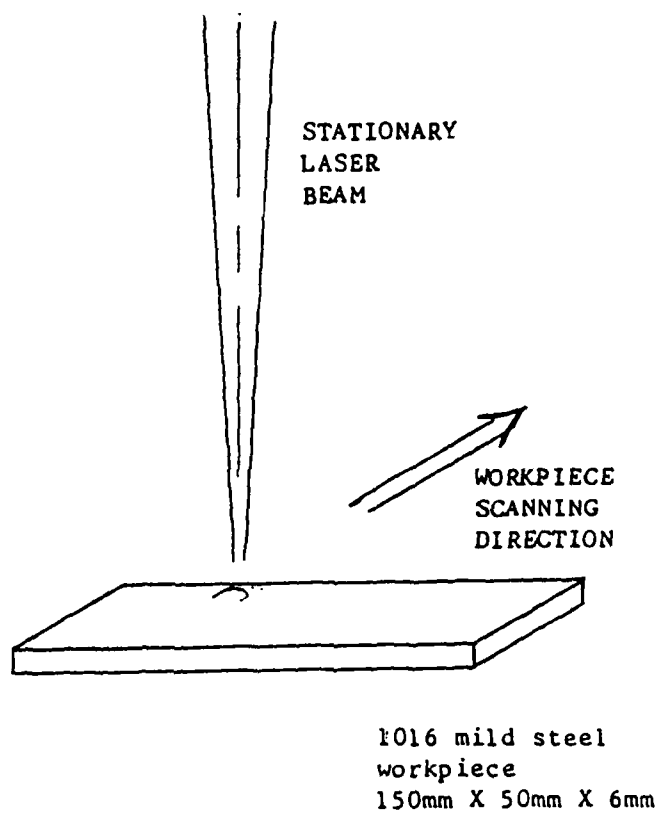


Figure 3.4.1 Schematic Diagram of the Experimental Set Up - Resolidified Region

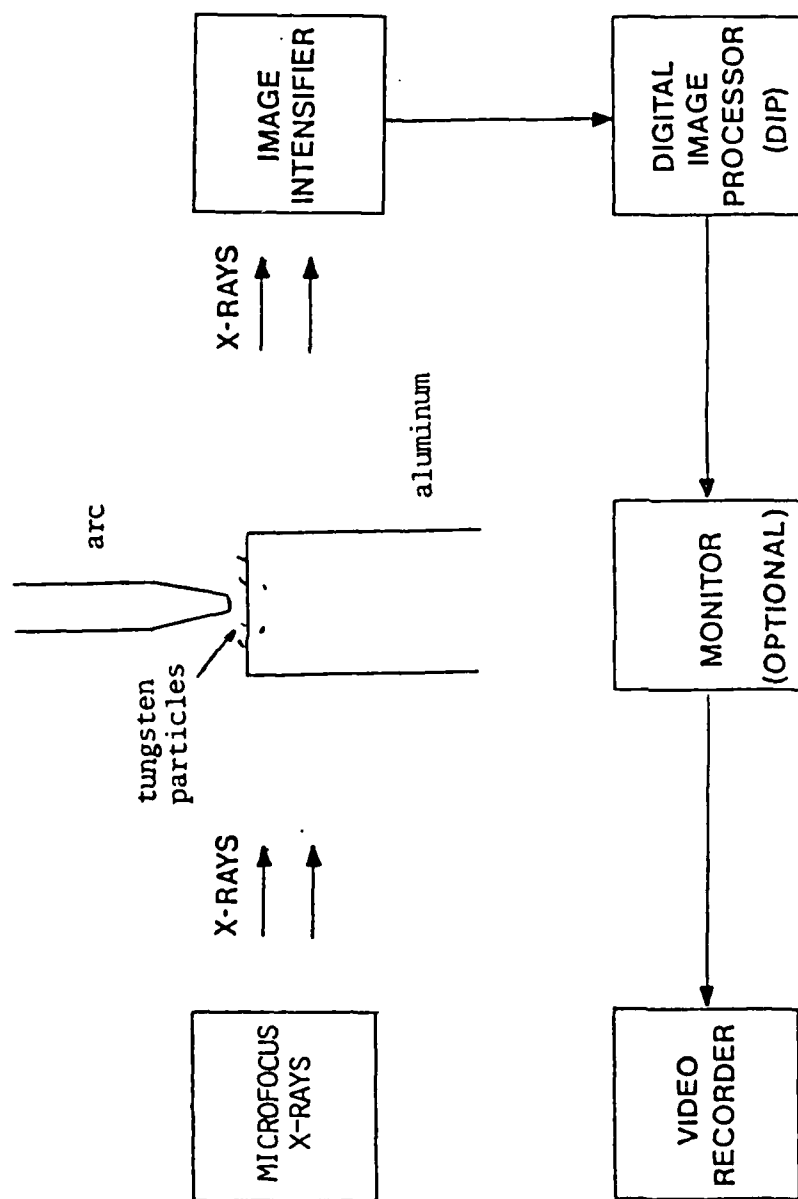


Figure 3.4.2 Schematic Diagram of the Experimental Set Up - X-ray Shadow Graph

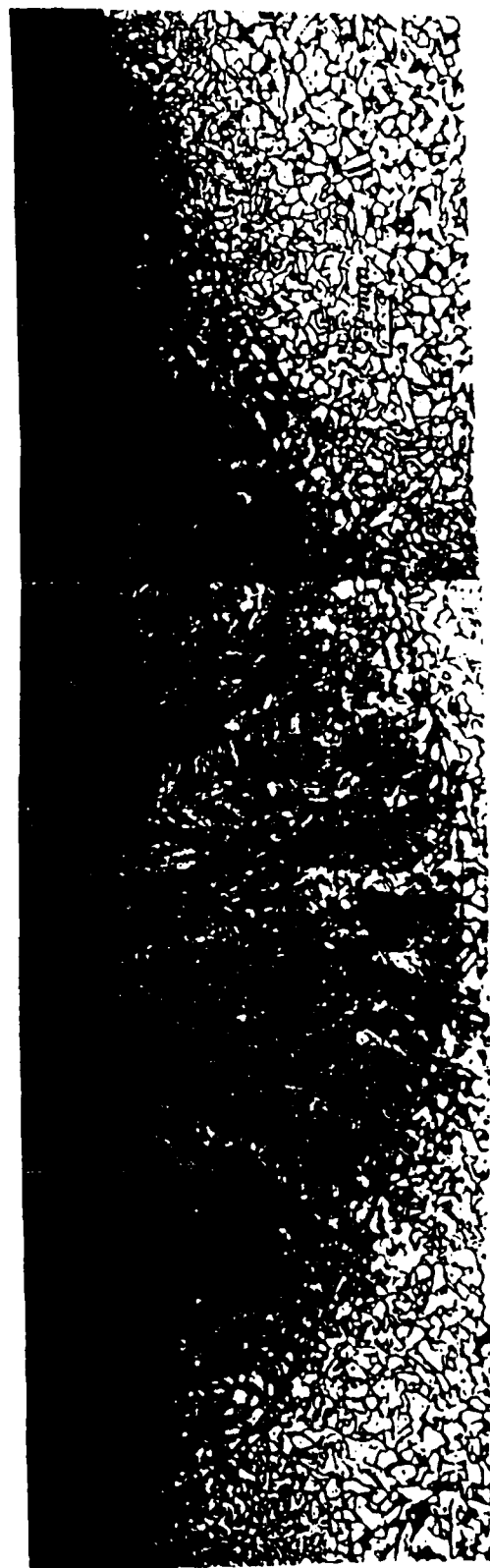


Figure 3.4.3 Micrograph of the Cross-section of the
Laser Melted Pool, Laser Power = 8.0 kW,
Beam Radius = 0.5 mm, Scanning Speed = 50 mm/sec

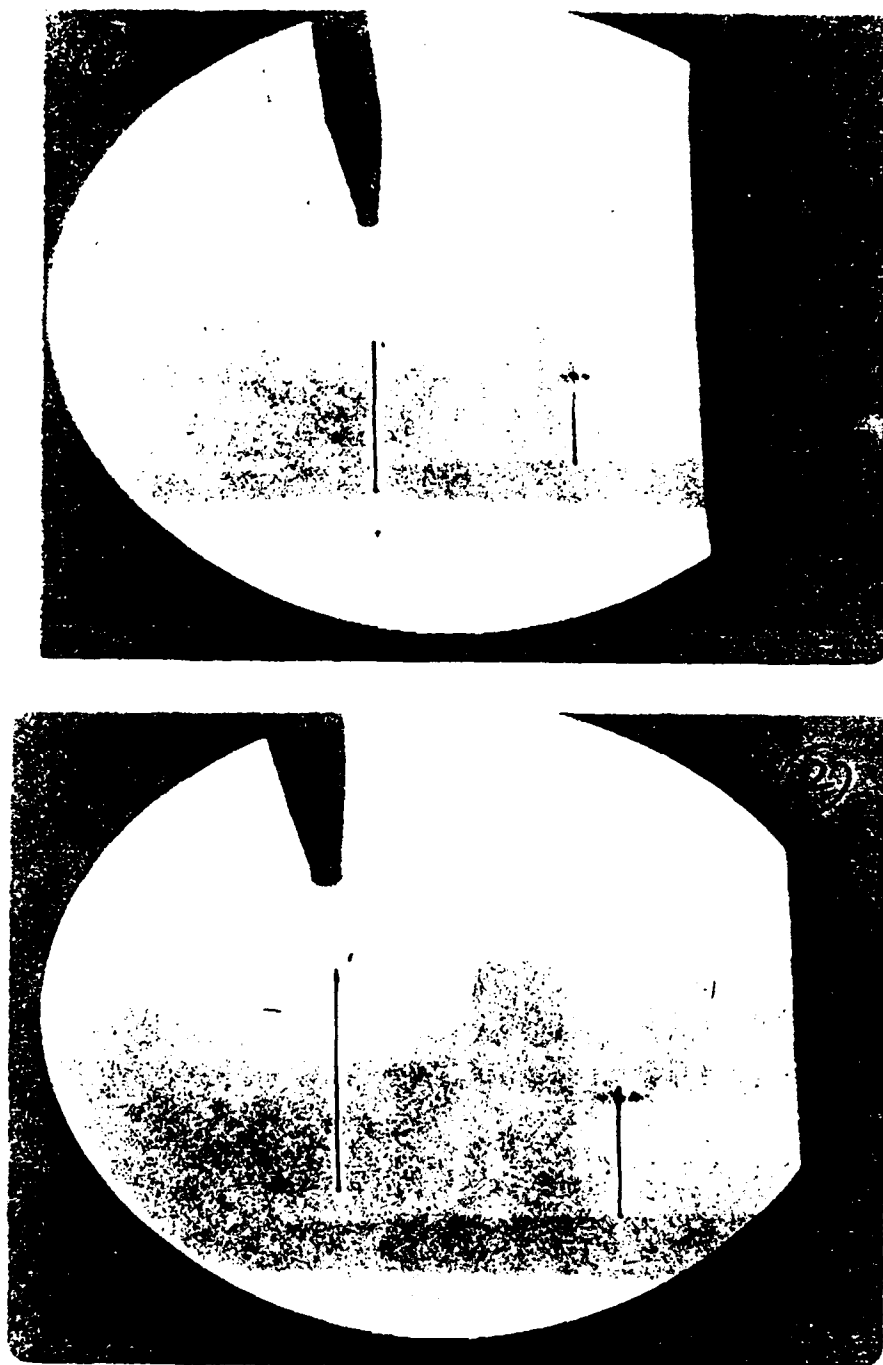


Figure 3.4.4 X-ray Shadow Graph of Two Successive Frames
Showing the Motion of the Tungsten Particle



Figure 3.4.5 Color Enhanced of X-ray Shadow Graph Showing the Temperature Difference at 1 Second after the Arc is Turned Off

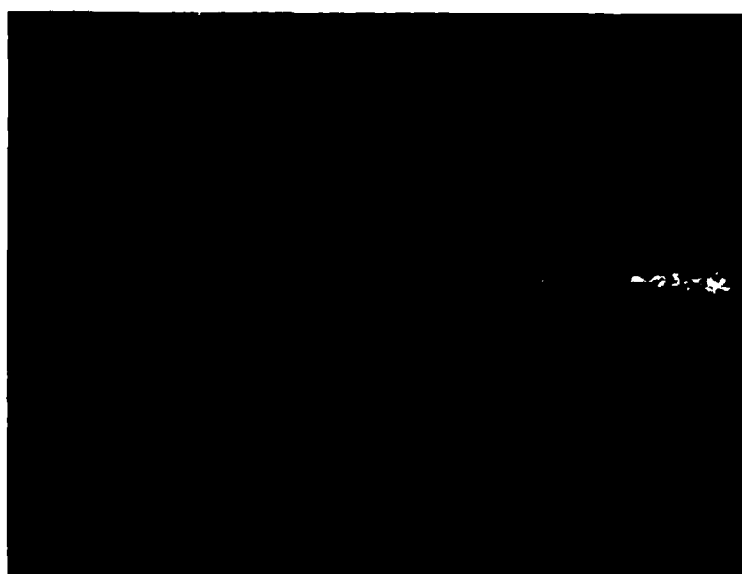


Figure 3.4.6 Color Enhanced of X-ray Shadow Graph Showing the Temperature Difference at 5 Seconds after the Arc is Turned Off



Figure 3.4.7 Color Enhanced of X-ray Shadow Graph Showing the Temperature Difference at 9 Seconds after the Arc is Turned Off

Table 3.4.1 Numerical Values of Process Parameters of the Experimental Runs

Beam Radius 0.5 mm

Case #	Scanning Speed	Laser Power	Aspect Ratio
1	25.0 mm/sec	2 kW	3.375
2	25.0 mm/sec	3 kW	3.51
3	25.0 mm/sec	4 kW	3.62
4	50.0 mm/sec	3 kW	3.66
5	50.0 mm/sec	4 kW	3.79
6	50.0 mm/sec	8 kW	4.0

4. SUMMARY AND CONCLUSIONS

Modeling efforts carried out in the first two years of this ONR program improved the general understanding of the process and revealed the different regimes of the flow as shown in Fig. 1.1. It also drew our attention to the singularities and limiting behavior of the flow which will be addressed in our future work. The important observation and correlations focus the present study can be summarized as follows.

1. Perturbation Model

The physics of the process changes in the presence of thermocapillary convection. It becomes convection dominated. This change the pool geometry dramatically (150 percent increase in the aspect ratio (width/depth) as compared to the conduction case). The cooling rate along the solidifying surface is found to be non-uniform. This in turn give rise to the non-uniform resolidified microstructure. The recirculating flow in the molten region gives a possible explanation of solute redistribution.

2. Stagnation Flow Analysis

This model represents the dominant feature in the central region of the melt pools in various materials processing processes. This model clarifies the scaling laws for thermocapillary convection in a deep melt pool. Single and concise expressions are obtained for the physical quantities such as velocity, temperature, and viscous and thermal boundary layers. Prandtl number dependence is also characterized. Good agreements are obtained in comparison with the basic flow of the perturbation model. The simple and concise expressions can therefore be used to estimate velocity and temperature.

3. Three-dimensional Model

This model provides the full three-dimensional realistic calculations of the process. Results of both thermocapillary and Lorentz flow are presented and discussed. It is found that the thermocapillary flow tends to shear the liquid metal to the pool edge while Lorentz force causes the flow in the opposite direction. Depending on their magnitudes one might dominate over the other. preliminary results of the free surface shape due to fluid motion is also presented and discussed.

4. Experimental Verification

Two experiments were performed to examine the validity of the models. It is found that both theoretical models and experiments predict the same trend in aspect ratio (width/depth). The aspect ratio increases with laser power. It is also found that the recirculating flow within the molten pool is of the order 1 m/sec which coincides with theoretical prediction. The cooling rate without the molten region is found to be non-uniform. It is higher on the surface and lower near the bottom.

REFERENCES

1. D. S. Gnanamuthu, Applications of Lasers in Materials Processing, E. A. Metzbower, ed., ASM, Metals Park, OH, 1979, pp. 177-289.
2. P. M. Moore, and L. S. Weiman, Proc. Soc. of Photo-Opt Instrum. Eng., 1979, Vol. 198, p. 120.
3. L. S. Weinman, J. H. Devault, and P. Moore, Applications of Lasers in Materials Processing, E. A. Metzbower, ed., ASM, Metals Park, OH, 1979 pp. 245-259.
4. C. W. Draper, Proc. Conf. of Lasers in Metallurgy, pp. 67-92, K. Mukherji and J. Mazumder, eds., TMS-AIME, Warrendale, PA, 1981.
5. L. S. Weinman, and J. H. Devault, AIP Conference Proc. No. 50, Symp. on Laser Solid Interactions and Laser Processing, Boston, Mass., 1978, p. 239, S. D. Ferris, H. I. Leamy, and J. M. Poate (ed.), American Inst. of Physics, New York, N.Y. 1979.
6. C. R. Heiple, and J. R. Roper, Welding Journal, 1982, Vol. 61, pp. 973-1025.
7. C. R. Heiple, J. R. Roper, R. T. Stagner, and R. J. Aden, Welding J., 1983, Vol. 62, pp. 72s-77s.
8. P. T. Houldcroft, British Welding J., 1954, Vol. 1, 468.
9. W. I. Pumphrey, British Welding J., 1955, Vol. 2, p. 93.
10. A. L. Shaeffler, Welding J., 1947, Vol. 26, pp. 601s-620s.
11. R. L. Apps, and D. R. Milner, British Welding J., 1963, Vol. 10, p. 348.
12. R. L. Apps, and D. R. Milner, British Welding J., 1955, Vol. 2, p. 475.
13. N. Christensen, V. de L. Davies, and K. Gjermundsen, British Welding J., 1965, Vol. 12, p. 54.
14. B. J. Bradstreet, Welding J., 1968, Vol. 47, pp. 314s-322s.
15. T. Chande, and J. Mazumder, Appl. Phys. Letter, 1982, Vol. 41, p. 42.
16. R. A. Woods, and D. R. Milner, Welding J., 1971, Vol. 50, pp. 163s-173s.
17. G. R. Salter, and D. R. Milner, British Welding J., 1960, Vol. 7, p. 89.
18. G. R. Salter, and D. R. Milner, British Welding J., 1965, Vol. 12, p. 222.
19. D. Howden, and D. R. Milner, British Welding J., 1963, Vol. 10, p. 395.
20. F. A. Crossly, Iron Age, 1960, Vol. 186, p. 102.

21. I. P. Trochum, and V. P. Chemsysh, Welding Production, 1965, Vol. 12, Nov., p. 6.
22. D. N. Petrakis, M. C. Flemings, and D. R. Poirier, Modeling of Casting and Welding Processes, H. Brody and D. Apelian, eds., published by TMS-SIME, Warrendale, Pa., 1981, pp. 285-231.
23. S. M. Copley, D. Beck, O. Esquivel, and M. Bass, Laser-Solid Interaction and Laser Processing--1978, S. D., Ferris, H. J. Leamy, and J. M. Poate, Editors, Conf. Proc. No. 50, American Institute of Physics, New York, NY, 1979, pp. 161-172.
24. O. Esquivel, J. Mazumder, M. Bass, and S. M. Copley, Rapid Solidification Processing, Principles and Technologies, II, R. Mehragian, B. H., Kear, and M. Cohen, Eds., Claitor's Publishing Div. Baton Rouge, LA, 1980, pp. 180-188.
25. S. M. Copley, D. G. Beck, O. Esquivel, and M. Bass, Proc. Conf. of Laser in Metallurgy, Chicago, IL, K. Mukerji, and J. Mazumder, ed., TMS-AIME, Warrendale, PA, 1981, pp. 1-20.
26. T. R. Anthony, and H. F. Cline, J. Appl. Phys., 1977, Vol. 48, pp. 3888-3894.
27. Oreper, G. M., T. W. Eagar, and J. Szekely (1983), Welding Journal, Vol. 63, p. 307s.
28. Wei, P. S., and W. H. Giedt (1985), Welding Journal, Vol. 4, p. 251s.
29. Ostrach, S. (1982), And. Rev. Fluid Mech., Vol. 14, pp. 313-345.
30. Viskanta, R., Solar Heat Storage: Latent Heat Materials, G. A. Lowe, ed., CRC Press Inc., 1982
31. Shamsundar, N., "Comparison of Numerical Methods for Diffusion Problems with Moving Boundaries, Moving Boundary Problem, Wolson, D. G., Solomon, A. D., and Boggs, P. T., eds., Academic Press, New York, Vol. 165, 1978.
32. Lynch, D. K., and K. O'Niel, "Continuously Deforming Finite Elements for the Solution of Parabolic Problems, With and Without Phase Change," Int. J. Numerical Methods Eng., Vol. 17, p.81, 1981.
33. C. W. Hirt, B. D. Nichols, and N. C. Romero, "A Numerical Solution Algorithm for Transient Fluid Flows," Los Alamos Scientific Laboratory, Report No. UC-34 and UC-79d, April 1975.
34. Cannahan, B., H. A. Luther, and J. O. Wilkes, Applied Numerical Methods, John Wiley and Sons, Inc.
35. White, F. M., Viscous Fluid Flow, McGraw-Hill, 1974.

36. Chan, C. L., J. Mazumder, and M. M. Chen, (1984), Metal. Trans. A, Vol. 15A, p. 2175.
37. C. Chan, J. Mazumder, and M. M. Chen, Applications of Lasers in Materials Processing, p. 150, E. A. Metzbower, ed., ASM, 1983.
37. Chan, C. L., J. Mazumder, and M. M. Chen (1984), Lasers in Metallurgy II, Proc., Symp. at the 113th AIME Annual Meeting, Los Angeles, Ca., Feb. 26, to March 1, 1984 by AIME, Warrendale, PA.
38. Fu, B., and Ostrach, S., Numerical Solutions of Floating Zone Crystal Growth, Department of Mechanical and Aerospace Engineering, Case Western Reserve University, Cleveland, Ohio.
39. Cowley, S. J., and Davis, S. H., Viscous Thermocapillary Convection at High Marangoni Number, J. Fluid Mechanic (1983), Vol. 135, pp. 175-188.
40. T. Chande, and J. Mazumder, Metal. Trans. B, 1983, Vol. 14B, pp. 181-190.
41. Brandes, E. A., Smithells Metals Reference Book, 6th ed., Butterworth.
42. Chan, C., "Thermocapillary Convection During Laser Surface Heating," Ph.D. Thesis, University of Illinois, Urbana, Illinois, 1986.
43. Chorin, A. J., "A Numerical Method for Solving Incompressible Viscous Flow Problems", J. of Computational Physics, 1967, Vol. 2, pp. 12-26.
44. Mech, A. R., Private Communications.
45. Dussan, V. E. B., "On the Spreading of Liquid on Solid Surfaces: Static and Dynamic Contact Lines", Ann. Rev. Fluid Mech., Vol. 11, pp. 371-.
46. Zehr, R. L., "A Three-dimensional Finite-Difference Computation of Thermocapillary Convection in Weld Pools and Laser Heated Melt Pools," M.S. Thesis, University of Illinois, Urbana, Illinois, 1986.
47. Chan, C., Chen, M. M., and Mazumder, J., "Thermocapillary Convection in the Central Region of a Deep Melt Pool due to Intense, Non-uniform Surface Heating," presented at the 1985 ASME/AIChE National Heat Transfer Conference in Denver, Colorado, Aug. 4-7, 1985.
48. Chen, C., Chen, M. M., and Mazumder, J., "High and Low Prandtl Number Limits for Stagnation Thermocapillary Convection in the Central Region of a Deep Melt Pool Due to Non-Uniform Surface Heating," presented at 1985 ASME Winter Annual Meeting, Miami, Florida, Nov. 17-21, 1985.
49. Chan, C., Mazumder, J., and Chen, M. M., "An Axis-symmetry Model for Convection in a Laser Melted Pool," presented in 113th Meeting of AIEE Conference, Feb. 21-Mar. 1, 1984.

50. Chan, C., Mazumder, J., and Chen, M. M., "Perturbation Model for Three-dimensional Thermocapillary Convection in Laser Melt Pool," accepted for presentation in 1986 ASME Winter Annual Meeting, Anaheim, California.
51. Chan, C., Zehr, R., Mazumder, J., and Chen, M. M., "Three-dimensional Model for Convection in Laser Weld Pool," presented at the Engineering Foundation Conference on Modeling and Control of Casting and Welding Processes, Santa Barbara, California, Jan 12-17, 1986.

END
DTIC

9-86